Supporting information

for *Environmental Science: Water Research & Technology*

Reactions of pyrrole, imidazole, and pyrazole with ozone: kinetics and mechanisms

Agnes Tekle-Röttering,[1*] Sungeun Lim,[2,3*] Erika Reisz,[4] Holger V. Lutze,[5,6,7] Mohammad Sajjad Abdighahroudi,[5] Sarah Willach,[5] Winfried Schmidt,[1,6] Peter R. Tentscher,[8] Daniel Rentsch,[9] Christa S. McArdell,[2] Torsten C. Schmidt,[5,6,7†] Urs von Gunten[2,3†]

[1]Westphalian University of Applied Sciences, Department of Environmental Engineering, Neidenburgerstraße 10, 45897 Gelsenkirchen, Germany

[2]Eawag, Swiss Federal Institute of Aquatic Science and Technology, Überlandstrasse 133, 8600 Dübendorf, Switzerland

[3]School of Architecture, Civil and Environmental Engineering (ENAC), École Polytechnique Fédérale de Lausanne (EPFL), 1015 Lausanne, Switzerland

[4]University "Politehnica" of Timişoara, Faculty of Industrial Chemistry and Environmental Engineering, Bulevardul Vasile Pârvan Nr. 6, 300233 Timişoara, Romania

[5]University of Duisburg-Essen, Faculty of Chemistry, Instrumental Analytical Chemistry,

Universitätsstraße 5, 45141 Essen, Germany

[6]Centre for Water and Environmental Research (ZWU), University of Duisburg-Essen, Universitätsstraße 2, 45141 Essen, Germany

[7]IWW Water Centre, Moritzstraße 26, 45476 Mülheim an der Ruhr, Germany

[8]Department of Chemistry and Bioscience, Aalborg University, 9220 Aalborg East, Denmark

[9]EMPA, Swiss Federal Laboratories for Materials Science and Technology, 8600 Dübendorf, Switzerland

---

[*] Co-primary authors equally contributed to this work

[†] Co-corresponding authors (contact: vongunten@eawag.ch, +41 58 765 5270)

Table of contents

Table S1. List of chemicals used.

All reagent solutions (aqueous) were prepared in ultrapurified water obtained from Barnstead™ Nanopure™ (Thermo Scientific) or Direct8/16system (Merck Millipore).

Chemicals and purity	**Suppliers**	**Product No.**
1,5-Dihydro-pyrrol-2-one ≥98%	Chem-Impex	CH6371383198
1-Benzylimidazole 99%	Sigma Aldrich	116416
1-Benzylpyrazole 98%	abcr	AB312011
1H-Pyrazol-4-ol 97%	abcr	AB416886
1H-Pyrazole-3,4,5-d_3	Toronto Research Chemicals	P842197
6-benzyladenine 98.5%	Dr. Ehrenstorfer	DRE-C10569600
Acetic acid (glacial) 100%	Merck	1370002500
Acetone-d_6 99.9%	Cambridge Isotope Laboratories	DLM-9-25
Acetonitrile Optima™ LC/MS Grade	Fisher Chemical	A955-212
Acetylacetone ≥99%	Sigma Aldrich	8000230250
Ammonium acetate ≥98%	Merck	1011160500
Ammonium bicarbonate ≥99.5%	Sigma Aldrich	09830-500G
Ammonium formate ≥99.0%	Sigma-Aldrich	17843
Dimethylsulfoxide 99.9%	J.T. Baker	
di-Sodium hydrogen phosphate dihydrate ≥99.5%	Merck	106580
DMSO-d_6 99.9%	Cambridge Isotope Laboratories	DLM-10-100
EPA 8270/Appendix IX Nitrosamines Mix	Sigma Aldrich	502138
Formaldehyde 37%	Merck	
Formic acid 98-100%	Merck	100264
Imidazole anhydrous ≥99%	Sigma Aldrich	792527
Imidazole-d_4 98%	Cambridge Isotope Laboratories	DLM-3033-1
Maleimide 99%	Sigma Aldrich	129585-2G
Methanol Optima™ LC/MS Grade	Fisher Chemical	A456-212
N-Benzylformamide 99%	abcr	AB131671
Phosphoric acid ≥85%	Sigma Aldrich	30417
Potassium indigotrisulfonate	Sigma Aldrich	234087
Pyrazole 98%	Sigma Aldrich	P56607-5G
Pyrrole-d_5 98%	Cambridge Isotope Laboratories	DLM-3192-1
Sodium cyanate 96%	Sigma Aldrich	185086
Sodium dihydrogen phosphate monohydrate 99-102%	Merck	106346
tert-Butanol ≥ 99.7%	Sigma Aldrich	19460

Text S1. Reaction kinetics

This section describes the methods used for determining the reaction kinetics of the reactions of azoles with ozone and presents the data plots from competition kinetics and pseudo-first-order kinetic experiments (Figure S1).

Competition kinetics for determination of k_{O3} of pyrrole and imidazole. The apparent second-order rate constants for the reactions of pyrrole, imidazole, and pyrazole with ozone (k_{app}) at pH 0.5 to 12 were determined by a competition kinetics method with 3-buten-2-ol as a competitor. Reaction vessels containing an azole (typically 0.1 – 0.6 mM for pyrrole and 1 – 5 mM for imidazole), 3-buten-2-ol (1 mM) at various ratios and dimethylsulfoxide (DMSO, 0.1 M) as a $^{\bullet}$OH scavenger were prepared and a fixed dosage of an ozone stock solution (~40 µM) was added under rapid mixing. DMSO was used to quench $^{\bullet}$OH instead of *t*-butanol, because the reaction of *t*-butanol with $^{\bullet}$OH produces formaldehyde, the same product as expected for the reaction of 3-buten-2-ol with ozone. The second-order rate constants are 8.2 $M^{-1}\,s^{-1}$ for the reaction of DMSO with ozone[1] and 6.6×10^{9} $M^{-1}\,s^{-1}$ for the reaction of DMSO with $^{\bullet}$OH.[2] After the reaction, formaldehyde, a product of the reaction of 3-buten-2-ol with ozone, was quantified by the Hantzsch method.[3] The second-order rate constant of an azole was deduced based on the following equation with 7.9×10^{4} $M^{-1}\,s^{-1}$ as $k_{\mathrm{O3,3\text{-}buten\text{-}2\text{-}ol}}$.[4]

$$\frac{[\text{formaldehyde}]_0}{[\text{formaldehyde}]} = 1 + \frac{k_{\mathrm{O_3,azole}}[\text{azole}]}{k_{\mathrm{O_3,3\text{-}buten\text{-}2\text{-}ol}}[\text{3-buten-2-ol}]}$$

Direct measurement of pyrazole decrease for determination of k_{O3} of pyrazole. The apparent second-order rate constant for the reaction of pyrazole with ozone at pH 7 was determined by a direct method following pyrazole decrease over time under conditions with ozone in excess. Using the ozone excess condition was necessary, because otherwise ozone-reactive transformation products from the pyrazole-ozone reaction (see the section 3.3 of the main text) would lead to an overestimation of the second-order ozone rate constant. A solution containing 5 µM of pyrazole and 0.3 mM of *t*-butanol as a $^{\bullet}$OH scavenger was prepared at pH 7 (10 mM phosphate buffer). An aliquot of the primary ozone stock solution (typically 1.3 – 1.5 mM) was added to the pyrazole solution to yield 100 µM ozone. Samples were taken by a laboratory dispenser at pre-determined reaction times (starting from 15 s) at which the residual ozone concentrations in the samples were quenched by approximately 200 µM cinnamic acid. The pyrazole concentrations were determined by HPLC-UV.

Direct measurement of ozone decrease by a quench-flow apparatus for determination of k_{O3} of maleimide and 4-hydroxypyrazole. A solution containing 1.9 mM of maleimide or 4-hydroxypyrazole and 0.5 M of *t*-

butanol was prepared at pH 7 (10 mM phosphate buffer). An ozone stock solution (0.275 mM) was prepared by diluting the primary ozone stock solution (typically 1.3 – 1.5 mM) with 1 mM hydrochlorous acid solution and kept in ice packs. The reaction was initiated by mixing the substrate and the ozone solutions at a ratio of 10:1 (1.7 mM substrate and 0.025 mM ozone as the concentrations after mixing) and an indigotrisulfonate solution (0.038 mM) was added at pre-determined reaction times to quench the remaining ozone. The experiments were conducted by a quench-flow apparatus (BioLogic, SFM-400/Q) which allows quenching the reactions within a ms range. The ozone concentrations were determined by the decolorization of the indigo solution measured spectrophotometrically at 600 nm (ε_{600nm} = 20,000 M^{-1} cm^{-1}).[5] For 4-hydroxypyrazole, ozone was completely consumed within the shortest reaction time (22 ms). Assuming 98 % of ozone is consumed at 22 ms, the second-order rate constant for the reaction of 4-hydroxypyrazole with ozone was estimated to be higher than 9×10^4 M^{-1} s^{-1}.

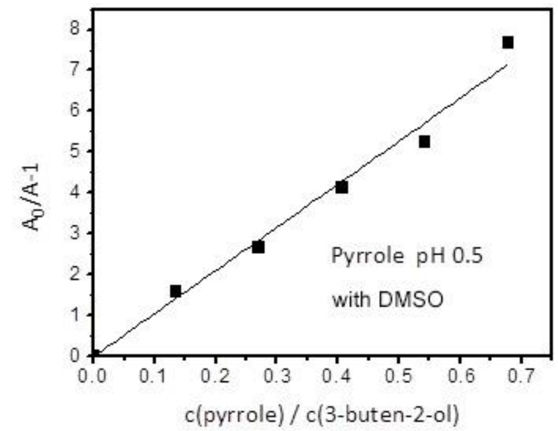
A0/A-1
0
1
2
3
4
5
6
7
8
0.0
0.1
0.2
0.3
0.4
0.5
0.6
0.7
c(pyrrole) / c(3-buten-2-ol)
Pyrrole pH 0.5
with DMSO

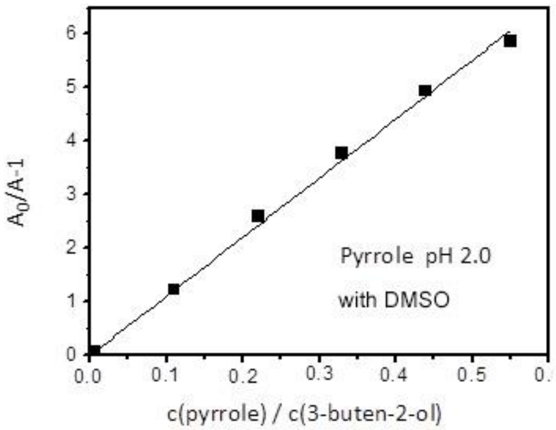
A0/A-1
0
1
2
3
4
5
6
0.0
0.1
0.2
0.3
0.4
0.5
c(pyrrole) / c(3-buten-2-ol)
Pyrrole pH 2.0
with DMSO

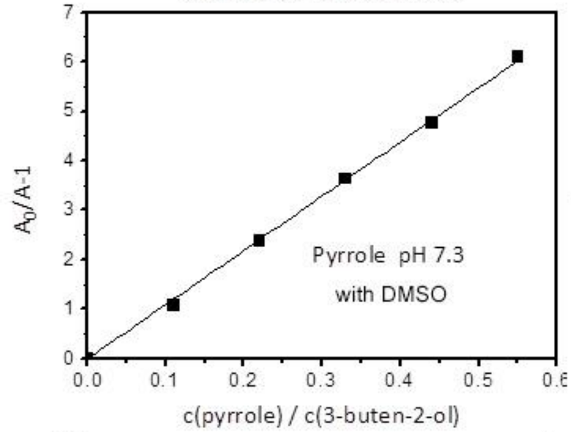
A0/A-1
0
1
2
3
4
5
6
7
0.0
0.1
0.2
0.3
0.4
0.5
c(pyrrole) / c(3-buten-2-ol)
Pyrrole pH 7.3
with DMSO

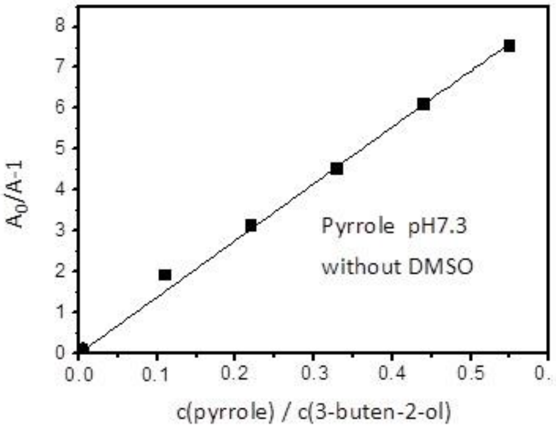
A0/A-1
0
1
2
3
4
5
6
7
8
0.0
0.1
0.2
0.3
0.4
0.5
c(pyrrole) / c(3-buten-2-ol)
Pyrrole pH7.3
without DMSO

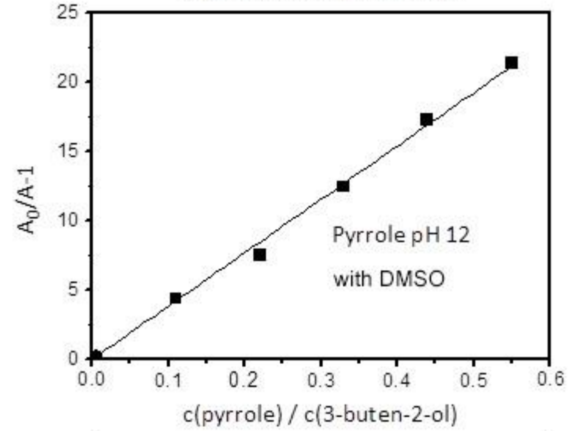
A0/A-1
0
5
10
15
20
25
0.0
0.1
0.2
0.3
0.4
0.5
0.6
c(pyrrole) / c(3-buten-2-ol)
Pyrrole pH 12
with DMSO

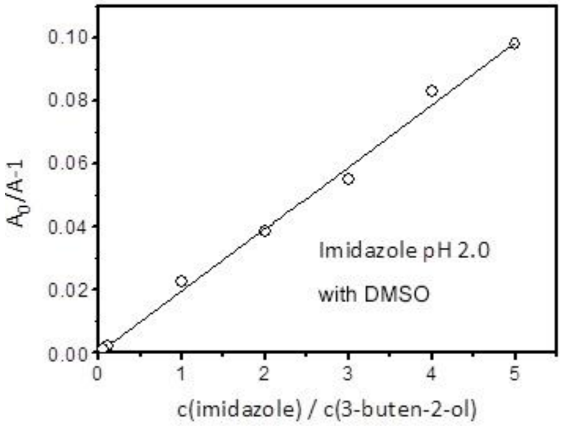
A0/A-1
0.00
0.02
0.04
0.06
0.08
0.10
0
1
2
3
4
5
c(imidazole) / c(3-buten-2-ol)
Imidazole pH 2.0
with DMSO

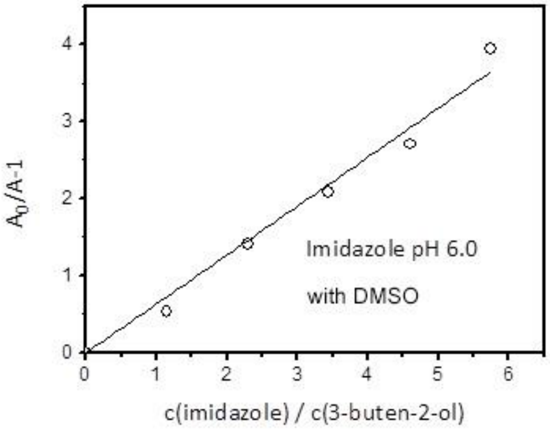
A0/A-1
0
1
2
3
4
0
1
2
3
4
5
6
c(imidazole) / c(3-buten-2-ol)
Imidazole pH 6.0
with DMSO

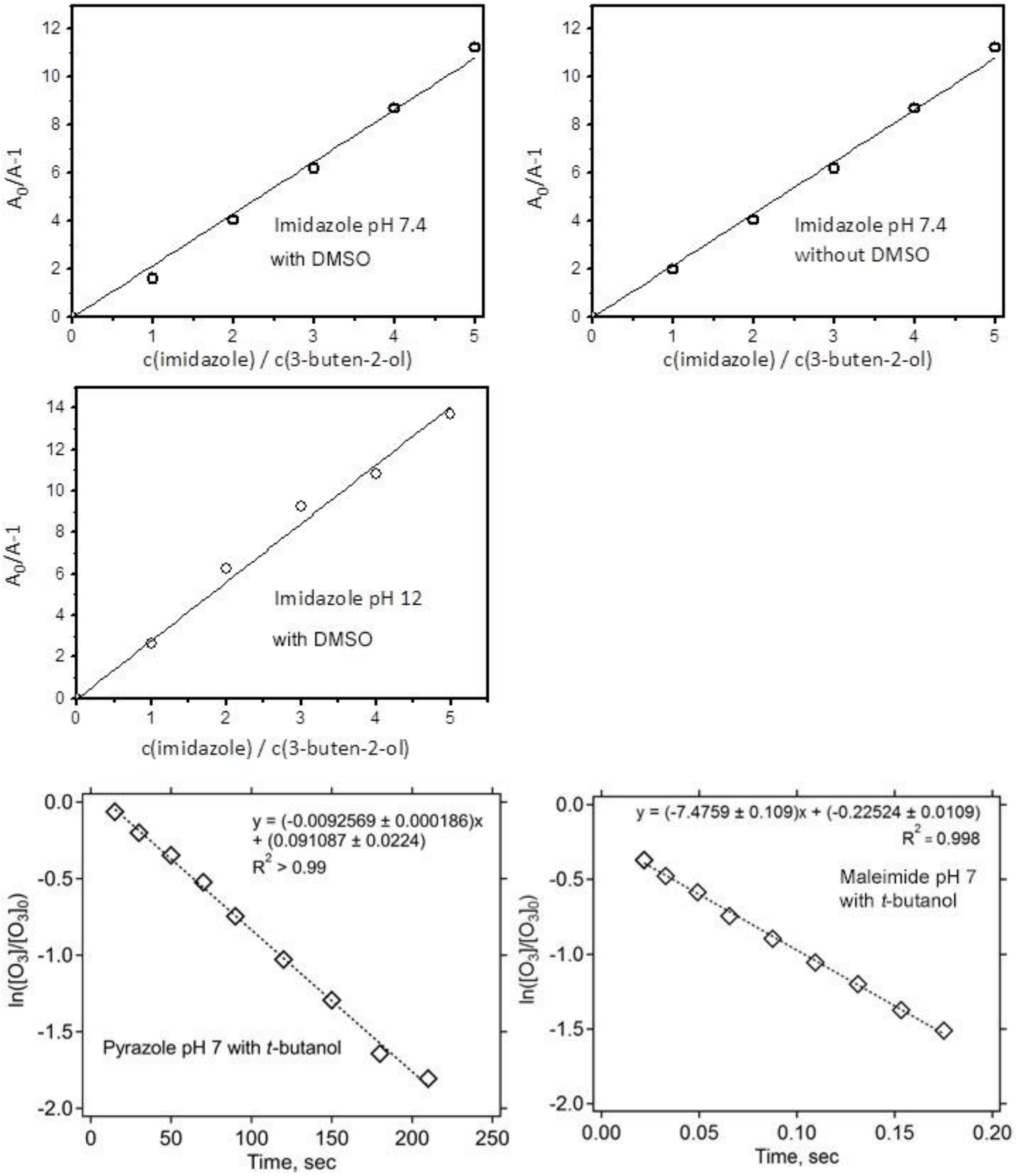

Figure S1. Competition kinetics plots for the reactions of ozone with pyrrole, imidazole, and pyrazole under varying pH conditions corresponding to the results presented in Table S2. A pseudo-first-order kinetic plot for the reaction of maleimide with ozone at pH 7 is also shown. Data points shown in each plot are from single measurements.

Table S2. Compilation of the apparent second-order rate constants (k_{app}) for the reactions of pyrrole, imidazole, pyrazole, and maleimide with ozone for the pH range 0.5 – 12.

Compound	**pH**	**$^{\bullet}$OH scavenger**	**k_{app}, $M^{-1}\,s^{-1}$**
Pyrrole	0.5	DMSO	$(8.3 \pm 0.6) \times 10^5$
	2.0	DMSO	$(8.7 \pm 0.6) \times 10^5$
	7.3	DMSO	$(8.6 \pm 0.7) \times 10^5$
	7.3	None	$(1.1 \pm 0.2) \times 10^6$
	12.0	DMSO	$(3.1 \pm 0.4) \times 10^6$
Imidazole	2.0	DMSO	$(1.5 \pm 0.1) \times 10^3$
	6.0	DMSO	$(5.0 \pm 0.5) \times 10^4$
	7.4	DMSO	$(1.7 \pm 0.2) \times 10^5$
	7.4	None	$(1.5 \pm 0.1) \times 10^5$
	12.0	DMSO	$(2.2 \pm 0.2) \times 10^5$
Pyrazole	7.0	*t*-butanol	$(5.6 \pm 0.9) \times 10^1$
Maleimide	7.1	*t*-butanol	$(4.2 \pm 0.2) \times 10^3$

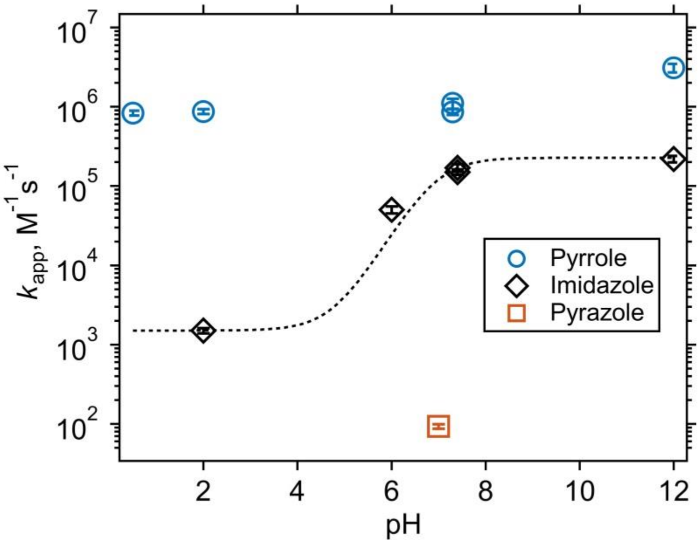

Figure S2. Logarithmic apparent second-order rate constants (k_{app}) for the reactions of pyrrole, imidazole, and pyrazole with ozone as a function of the pH in the range 0 to 12. The k_{app} values of imidazole were fitted to the expression: $k_{app} = k_{NH+}(1-\alpha) + k_N\alpha$ and $\alpha = 1/(1 + 10^{pKa-pH})$, where k_{NH+} and k_N are the species-specific second-order rate constants for the protonated and the neutral imidazole, respectively, α is the fraction of the neutral imidazole, and a pK_a value of imidazole is 7.0.[6] The following species-specific second-order rate constants were obtained: $(2.3 \pm 0.1) \times 10^5$ $M^{-1}\,s^{-1}$ for neutral imidazole (k_N) and $(1.5 \pm 0.1) \times 10^3$ $M^{-1}\,s^{-1}$ for protonated imidazole (k_{NH+}). The species-specific second-order rate constant for the reaction of pyrrole with ozone was obtained to be $(1.4 \pm 1.1) \times 10^6$ $M^{-1}\,s^{-1}$ by averaging k_{app} for the pH range 0.5 – 12.

Text S2. Kinetic simulations

The evolution of pyrrole and its transformation products as a function of the molar ratio of $[O_3]/[\text{Pyrrole}]_0$ was simulated by a kinetic simulation with the Kintecus software[7] based on a model described in Table S3. The simulated concentrations are shown as lines in Figure 2 in the main text. The imidazole-ozone reaction was also simulated based on a model described in Table S4 and the results are shown as lines in Figure 5 in the main text. Only the consumption of ozone by pyrrole, imidazole, and their transformation products were considered.

Table S3. Kinetic model for the pyrrole-ozone reactions performed by Kintecus.[7] The initial concentrations of pyrrole and ozone were set as [pyrrole] = 115 µM and $[O_3]$ = 0 – 250 µM (in 2 µM increments). Simulated reaction time was set as 4 h.

No.	**Reaction**	$\boldsymbol{k}_{\textbf{app,pH7}}$**,** $\mathbf{M^{-1}\,s^{-1}}$	**Reference**
1	Pyrrole + O_3 ==> 0.34*maleimide	8.6×10^5	Table 1 of main text
2	Maleimide + O_3 ==> Products	4.2×10^3	Table 1 of main text

Table S4. Kinetic model for the imidazole-ozone reaction performed by Kintecus.[7] The initial concentrations of imidazole and ozone were set as [pyrrole] = 94.5 µM and $[O_3]$ = 0 – 250 µM (in 2 µM increments). Simulated reaction time was set as 4 h.

No.	**Reaction**	$\boldsymbol{k}_{\textbf{app,pH7}}$**,** $\mathbf{M^{-1}\,s^{-1}}$	**Reference**
1	Imidazole + O_3 ==> Cyanate + Formamide + Formate	1.7×10^5	Table 1 of main text
2	Cyanate + O_3 ==> Products	1.0×10^{-2}	Hoigné et al. (1985)[8]
3	Formamide + O_3 ==> Products	1.0×10^{-2}	assumed as a slow reaction, considering the similar evolution as for cyanate (see Figure 5 in the main text)
4	Formate + O_3 ==> Products	46	Reisz et al. (2014)[9]

Text S3. Ozonation experiments

The required initial concentrations of azoles and ozone doses varied depending on the applied analytical methods for product identification. For example, NMR analyses require at least a few milligrams of isolated solids, whereas LC-HRMS/MS is capable of detecting submicromolar concentrations. Accordingly, various ozonation conditions were applied in this study and are described below.

(a) *Ozonation experiment for quantifying pyrrole, imidazole, pyrazole, 1-benzylimidazole, 1-benzylpyrazole, maleimide, urea, N-benzylformamide, cyanate, formate, and total N-nitrosamines by LC-HRMS/MS, IC-CD, and total N-nitrosamine analyses*. Ozonation experiments were conducted under the condition as described in the main text: [azole] ~100 µM, [*t*-butanol] = 50 mM, [ozone] = 0 – 200 µM, and 10 mM phosphate buffer (pH 7). Ozone stock solutions were prepared by an ozone generator (BMT MESSTECHNIK GMBH, BMT 803 BT). The oxygen gas flow rate was set as 0.15 NL min^{-1} (N stands for normal conditions being 0 °C and 1 atm) and the power of ozone generator was 100%. Based on the instrument manual (Rev. 05/2014), this condition yielded approximately 2.4 g h^{-1} of ozone production rate. Additionally for quantifying maleimide, 100 µM of pyrrole and 50 mM of *t*-butanol were prepared at pH 2 (10 mM phosphate buffer) to investigate the pH effect on maleimide formation.

(b) *Ozonation experiment for quantifying formamide by HPLC-UV.* Because of the high dilution factor (100-fold) required for quantification of formamide by HPLC-UV (see Text S4 for detailed method), a millimolar range of formamide should be formed during the azole-ozone reactions for the detection. Millimolar concentrations of azole and ozone were required accordingly. To this end, the primary ozone stock solution (1.59 ± 0.05 mM) was prepared as described above and 9 mL of the ozone stock solution were transferred to a 10 mL reaction vessels containing 1 – 2 mL of the mixture of azole, 1 M *t*-butanol, and 10 mM phosphate buffer solution at pH 7 under rapid stirring. The concentrations of azole in the mixtures were 0.8 mM – 2 mM of pyrrole, 1 mM – 4 mM of imidazole, and 0.3 mM – 1.5 mM of pyrazole, to produce varying molar $[O_3]/[azole]_0$ ratios of 0.8 – 2.0 for pyrrole, 0.4 – 1.5 for imidazole, and 1.0 – 5.6 for pyrazole.

(c) *Ozonation experiment for quantifying glyoxal by derivatization followed by HPLC-UV and for quantifying formate by IC-CD.* 1 mM of azoles were prepared in ultrapurified water without buffering agents in a volume of 20 – 25 mL in presence (0.1 – 0.5 M) or absence of *t*-butanol. Additionally, 1 mM of azoles in presence (0.1 – 0.5 M) or absence of *t*-butanol were prepared at pH 2 (by adding sulfuric acid) or pH 11 (by adding sodium hydroxide) to investigate the pH effect on glyoxal and formate formation. Ozone stock solutions were prepared by another ozone generator (Erwin Sander Elektroapparatebau GmbH, Laboratory Ozonizer 300.5), yielding the maximum concentration of the stock solution of 1 mM. An aliquot of the ozone stock solution was added to the azole solution to initiate ozonation with ozone doses ranging from 40 µM to 200 µM. The pH of the azole solution without buffering agents was in the range of pH 6.5 – 7.4 prior to ozonation, which decreased to pH 4.3 – 6.1 after ozonation. The pH of the acidified (pH 2) and basified (pH 11) solutions remained the same after ozonation. The complete consumption of ozone was verified regularly with indigotrisulfonate.

(d) *Ozonation experiments for identifying TP1, TP2, and maleimide by NMR*. Solutions containing 1 mM of pyrrole and 1 M of *t*-butanol were prepared in ultrapurified water without buffering agents with a total volume of 1 L. Buffering agents could not be used because they would remain in too large quantities after work-ups for NMR (Text S4), which makes it difficult to isolate ozonation products. A decrease in pH was observed from pH 5.8 before ozonation to pH 4.5 after ozonation. Ozonation was initiated by directly sparging an ozone-containing oxygen gas flow produced by an ozone generator (BMT MESSTECHNIK GMBH, BMT 803 BT) to the pyrrole solution, which was kept at room temperature under constant stirring. The oxygen gas flow rate was set as 0.02 NL min^{-1} and the power of ozone generator was 30 %. Under this condition, the ozone production rate would be roughly 0.1 g h^{-1}. During ozonation, 100 µL of samples were withdrawn at pre-defined reaction times, to analyze the remaining pyrrole concentrations in the solution by HPLC-UV. As a result, a 30 min ozonation time was selected for NMR analyses, for which more than 80% pyrrole was abated. A control experiment by sparging oxygen gas with the same flow rate but without generating ozone was performed in parallel to confirm the effect of the gas flow on evaporation or abatement of pyrrole. The HPLC-UV result of the control experiment confirmed that the pyrrole concentrations remained unchanged over 90 min under the oxygen gas flow.

Text S4. Analytical methods for azoles and their transformation products

This section describes the analytical methods used for quantifying abatement of azoles upon ozonation and for identifying/quantifying transformation products formed during the azole-ozone reactions.

NMR analyses for TP1, TP2, and maleimide. Prior to NMR analyses, *t*-butanol and water in ozonated solutions were removed by (1) rotary evaporation (Hei-VAP, Heidolph) at 40 °C to dryness, or (2) rotary evaporation at 25 °C to 20 % removal in weight, followed by lyophilization (LYOVAC GT 2-E, STERIS) to dryness. The work-up procedure (2) was employed to minimize the increase of temperature in the solution, which appeared to promote polymerization of ozonated products. The isolated solids were dissolved in acetone-d_6 or DMSO-d_6. ^{1}H and ^{13}C NMR data were measured at 400.2 MHz and 100.6 MHz using a 5 mm CryoProbe™ Prodigy probe equipped with z-gradient on a Bruker Avance III 400 NMR spectrometer (Bruker Biospin AG, Fällanden, Switzerland). The 1D ^{1}H, ^{13}C and ^{1}H 1D-NOESY NMR experiments and the 2D correlated ^{1}H-^{13}C HSQC, ^{1}H-^{13}C HMBC, ^{1}H-^{1}H DQF-COSY, and ^{1}H-^{1}H NOESY experiments were performed at 298 K using the Bruker standard pulse programs and parameter sets applying 90° pulse lengths of 11.4 μs (^{1}H) and 10.0 μs (^{13}C). Chemical shifts (δ) in ppm are calibrated to residual solvent peaks (DMSO-d_6: δ = 2.49 and 38.5 ppm; acetone-d_6: δ = 2.05 and 29.8 ppm). Details of product identification by the NMR analyses are provided in Text S7.

LC-HRMS/MS for pyrrole, imidazole, pyrazole, 1-benzylimidazole, 1-benzylpyrazole, maleimide, urea, and N-benzylformamide. Non-ozonated (ozone dose = 0 µM, azole concentration 100 µM) and ozonated samples were diluted 10-fold (for imidazole, pyrazole, 1-benzylimidazole, urea, and *N*-benzylformamide) or 20-fold (for pyrrole and 1-benzylpyrazole) in ultrapurified water or in acetonitrile depending on the applied LC column. For quantifying maleimide, ozonated samples were analyzed without dilution, because of the relatively poor sensitivity of detecting maleimide by LC-HRMS/MS (see the limits of quantification of maleimide and other compounds summarized in Table S6). Pyrrole-d5 (5 µM as final concentration), imidiazole-d5 (10 µM), pyrazole (1 µM), or 6-benzyladenine (1 µM) prepared in acetonitrile or in ultrapurified water were used as internal standards for all analytes except urea (Text S16). Pyrrole, pyrazole, 1-benzylimidazole, 1-benzylpyrazole, and *N*-benzylformamide in the samples diluted in ultrapurified water were separated on a C18 reversed-phase (RP) column (Atlantis® T3, 3 µm particle size, 3.0 × 150 mm, Waters) at 30 °C with a flow of 300 µL/min and ultrapurified water and methanol as eluents. 0.1% formic acid was added to both eluents. The gradient started with 98% of ultrapurified water during the first 1.5 min, which linearly decreased to 2% between 1.5 min and 17.5 min, maintained at 2% until 25 min, returned to the initial condition of 98% ultrapurified water at 25.1 min, and maintained at 98% until 29.5 min for column re-equilibration. Imidazole and urea in the samples diluted in acetonitrile were separated on a hydrophilic interaction liquid chromatography (HILIC) column (XBridge™ BEH HILIC XP, 2.5 µm particle size, 3.0 × 150 mm, Waters) at 30 °C with a flow of 400 µL min^{-1} and ultrapurified water and an acetonitrile:methanol:ultrapurified water mixture (95:3:2) as eluents. 1mM ammonium formate and 0.1% formic acid was added to both eluents. The gradient started with 100% of the acetonitrile mixture during the first 2 min, which linearly decreased to 5% between 2 min and 12 min, maintained at 5% until 17 min, returned to the initial condition of 100% acetonitrile mixture at 17.1 min, and maintained at 100% until 37 min for column re-equilibration. After separation on the RP or HILIC column, compounds were detected by a Thermo Scientific Q-Exactive high-resolution mass spectrometer (R = 70,000) with electrospray ionization (ESI) in positive full scan mode with a spray voltage of 4000 V, a capillary temperature of 350 °C, a sheath gas flow rate of 40 (arbitrary units), and an auxiliary gas flow rate of 10 (arbitrary units). Detected and theoretical exact masses deviated typically within 5 ppm (Table S5), except urea which showed high mass deviation of ~50 ppm for both ozonated samples and standards (Text S16).

Table S5. Theoretical and detected exact masses as $[M+H]^+$ of the compounds (parent compounds (azoles) and identified or suspected transformation products) measured by LC-HRMS/MS.

Compound	**Type**	**Molecular formula**	**Theoretical mass**	**Detected mass**
Pyrrole	Parent	C_4H_5N	68.0495	68.0495
Maleimide	TP	$C_4H_3NO_2$	98.0237	98.0236
N-(3-oxo-1-propen-1-yl)formamide (TP1)	TP	$C_4H_5NO_2$	100.0393	100.0391
5-Hydroxy-1,5-dihydro-2H-pyrrol-2-one (TP2)	TP	$C_4H_5NO_2$	100.0393	100.0391
1,5-dihydro-pyrrole-one	TP	C_4H_5NO	84.0444	84.0443
Imidazole	Parent	$C_3H_4N_2$	69.0447	69.0448
Urea	TP	CH_4N_2O	61.0396	61.0368
1-Benzylimidazole	Parent	$C_{10}H_{10}N_2$	159.0917	159.0915
N-Benzylformamide	TP	C_8H_9NO	136.0757	136.0755
Pyrazole	Parent	$C_3H_4N_2$	69.0447	69.0448
Formylhydrazine	TP	CH_4N_2O	61.0396	ND
4,5-dihydroxypyrazole	TP	$C_3H_4N_2O_2$	101.0346	ND
1-Benzylpyrazole	Parent	$C_{10}H_{10}N_2$	159.0917	159.0919
Candidate 191	TP	$C_{10}H_{10}N_2O_2$	191.0815	191.0813
Candidate 151	TP	$C_8H_{10}N_2O$	151.0866	151.0864

Table S6. Limits of quantification (LOQ) of azoles and identified or suspected transformation products.

Compound	**Method**	**LC column**	**LOQ, µM**[a]	**Calibration range**	**R^2 of calibration curve**	**Retention time, min**
Pyrrole	LC-HRMS/MS	RP	1.1	0.5 µM – 5 µM	> 0.99	9.2
Imidazole	LC-HRMS/MS	HILIC	0.8	1 µM – 10 µM	> 0.99	6.8
Pyrazole	LC-HRMS/MS	RP	2.5	1 µM – 10 µM	> 0.99	6.4
1-Benzylimidazole	LC-HRMS/MS	RP	3.0	1 µM – 10 µM	> 0.99	8.6
1-Benzylpyrazole	LC-HRMS/MS	RP	2.7	0.5 µM – 5 µM	0.97	15.8
Maleimide	LC-HRMS/MS	RP	12.9	10 µM – 100 µM	> 0.99	4.9
N-(3-oxo-1-propen-1-yl)formamide (TP1)	LC-HRMS/MS	RP	ND	ND	ND	6.3[b]
5-Hydroxy-1,5-dihydro-2H-pyrrol-2-one (TP2)	LC-HRMS/MS	RP	ND	ND	ND	4.2[b]
1,5-Dihydro-pyrrole-one	LC-HRMS/MS	RP	ND	ND	ND	Unconfirmed[c]
Urea[d]	LC-HRMS/MS	HILIC	2.1	1 µM – 10 µM	> 0.99	4.0
N-benzylformamide	LC-HRMS/MS	RP	2.9	1 µM – 10 µM	> 0.99	12.6
Candidate 191	LC-HRMS/MS	RP	ND	ND	ND	12.0
Candidate 151	LC-HRMS/MS	RP	ND	ND	ND	11.7
Cyanate	IC-CD	AS19	0.5	1 µM – 20 µM	> 0.99	10.0
Formate	IC-CD	AS19	1.0	1 µM – 20 µM	> 0.99	6.2
Formamide	HPLC-UV	HILIC	1.6	1 µM – 10 µM	> 0.99	2.9
Total *N*-nitrosamines	UV-Photolysis and Chemiluminescence[10]	NA	0.7[e]	0.4 µM – 4 µM	0.94	NA
Glyoxal	Deriv-HPLC-UV[f]	RP	0.8	1 µM – 20 µM	-	9.3

[a]LOQs were estimated based on the slope of the calibration curve (s) and the standard deviation of the y-intercept of the calibration curve (σ) with the following equation, LOQ = 10 × σ/s,[11] for all compounds except total *N*-nitrosamines. [b]Inconclusive but suggested based on structural characteristics and distinct MS2 fragmentation patterns (see main text). [c]Because of too many peaks (Figure S23b). [d]Urea quantification was performed without internal standard. [e]LOQ of total *N*-nitrosamine analysis was determined based on a signal-to-noise ratio of 10.[12] [f]*o*-phenylendiamine derivatization followed by HPLC-UV analysis.[13]

IC-CD for cyanate and formate and IC-MS for cyanate. Ozonated samples in the pH 7 buffered system (parent concentration 100 µM) were diluted 4-fold in ultrapure water to reduce column overloading from phosphate buffer. Cyanate and formate in the diluted samples were then separated on a capillary anion-exchange IC column (IonPac AS19-4µM, 0.4 × 250 mm, Dionex) with a gradient of KOH as eluent with a flow rate of 0.01 mL min^{-1}. The eluent concentration was initially at 10 mM for 10 min, increased to 28.5 mM between 10 min and 15 min, increased to 120 mM between 15 min and 15.1 min, was maintained at 120 mM until 23 min, went back to the initial concentration of 10 mM between 23 min and 23.1 min, and held at 10 mM until 32 min. The anions were detected by suppressed conductivity (ACES 300 Capillary Electrolytic Suppressor, Dionex). Examples of chromatograms of an ozonated sample and standards are shown in Figure S3. For cyanate, additional confirmation was carried out once by using a mass spectrometer (TSQ-Vantage, Thermo Scientific) by following a fragmentation reaction: $m/z = 42.0 \rightarrow 26.0$ (36 V collision energy). The MS measurements were performed in negative mode, HESI at 150°C. The peak corresponding to cyanate was observed at a retention time of 11.0 min. Formate in the ozonated samples without buffering agents or under pH 2 and 11 conditions (parent concentration 1 mM) was analyzed by IC-CD (883 Basic IC plus, Metrohm) equipped with a Metrosep Organic Acids column (Metrohm). The eluent was 0.5 mM sulphuric acid with a flow rate of 0.5 mL min^{-1}. The suppressor was regenerated with a 30 mM lithium chloride solution.

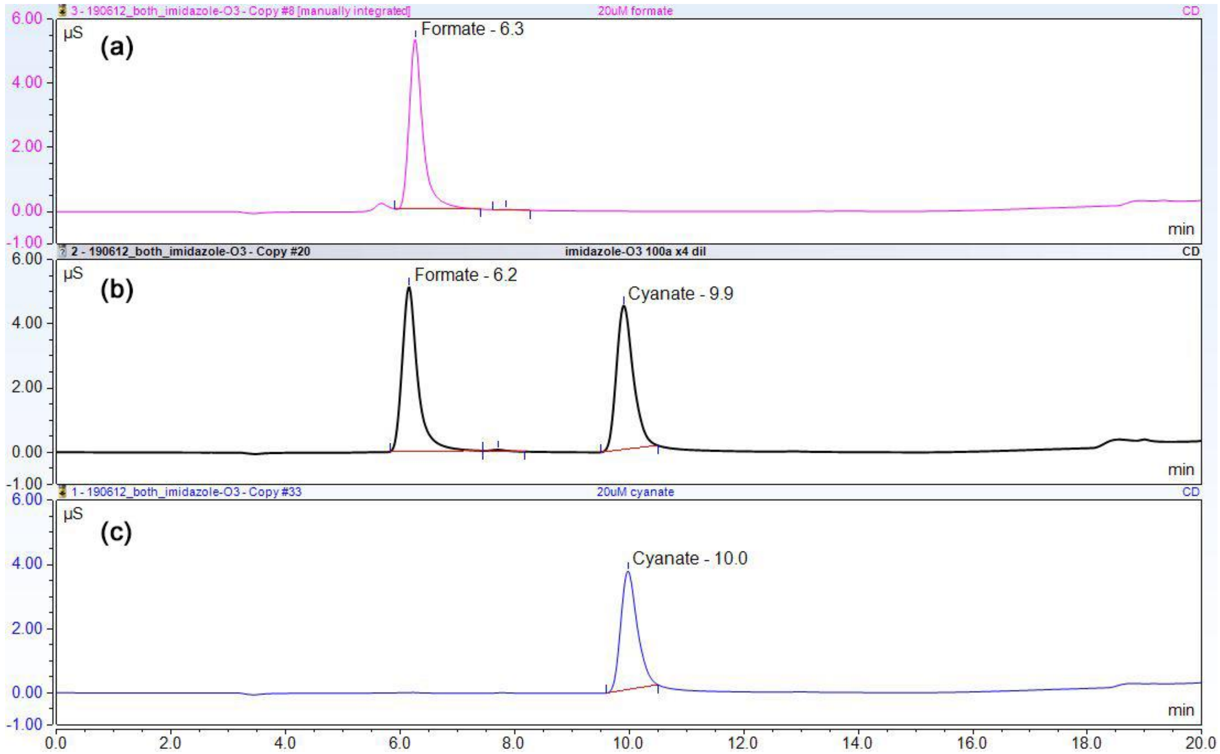

Figure S3. Stacked IC-CD chromatograms of (a) a 20 µM formate standard, (b) an ozonated imidazole solution at $[O_3]/[\text{imidazole}]_0$ ~ 1 diluted 4-fold in ultrapurified water, and (c) 20 µM cyanate standard.

HPLC-UV for pyrrole, imidazole, and pyrazole. Pyrrole and imidazole which were ozonated by sparging ozone directly into the azole solution for NMR and GC-MS analyses were analyzed by HPLC-UV to quantify the abatement. 100 µL of samples were withdrawn during ozonation at pre-determined time points and diluted 10-fold with ultrapurified water. Pyrazole of which ozone reactivity was determined by following the pyrazole decrease over time, was also analyzed by HPLC-UV without dilution. The samples were separated on a Cosmosil C18 column (5C18-MS-II, 3.0 × 100 mm, NACALAI TESQUE, INC.) with a gradient (0.5 mL min^{-1}) of acetonitrile as eluent A and ultrapurified water (for pyrrole) or 10 mM phosphate buffer at pH 7.5 (for imidazole) as eluent B. The gradient started at 5% acetonitrile (eluent A) during 1.5 min, which linearly increased to 95% between 1.5 min and 17.5 min, maintained at 95% to 22.5 min, decreased back to the initial condition of 5% acetonitrile until 23 min, and maintained at the initial conditions until 28 min. The samples for analyzing pyrazole were separated on the same column with an isocratic method (0.5 mL min^{-1}) with 5% acetonitrile and 95% 10 mM phosphate buffer (pH 7). All azoles were analyzed by UV detection at 210 nm.

HPLC-UV for formamide. The ozonated samples containing formamide (parent concentrations 0.3 mM – 4 mM) were diluted 100-fold in acetonitrile and were separated on the HILIC column (XBridge™ BEH HILIC XP, 2.5 µm particle size, 3.0 × 150 mm, Waters) at 30 °C with a flow of 400 µL min^{-1} via isocratic eluents of 3% ultrapurified water and 97% acetonitrile. The high dilution factor (100-fold) was required to achieve the ideal sample composition of 99% acetonitrile and 1% aqueous solution for the HILIC column. Because of the low molecular weight (m/z 45) below the MS scan range (m/z ≥ 50), formamide could not be detected by MS. Instead, it was analyzed by UV detection at 210 nm. Known concentrations of formamide standards (5 µM and 10 µM) were added to the ozonated samples containing formamide to additionally confirm the peak retention time and the quantified results. The peak retention times remained the same (2.94 min) before and after the addition of standard solutions (Figure S4). The averages of the relative difference between the measured increase in formamide concentration of the spiked sample and the concentration of the spiked formamide standard were (9 ± 7)% for 5 µM addition and (11 ± 1)% for 10 µM addition.

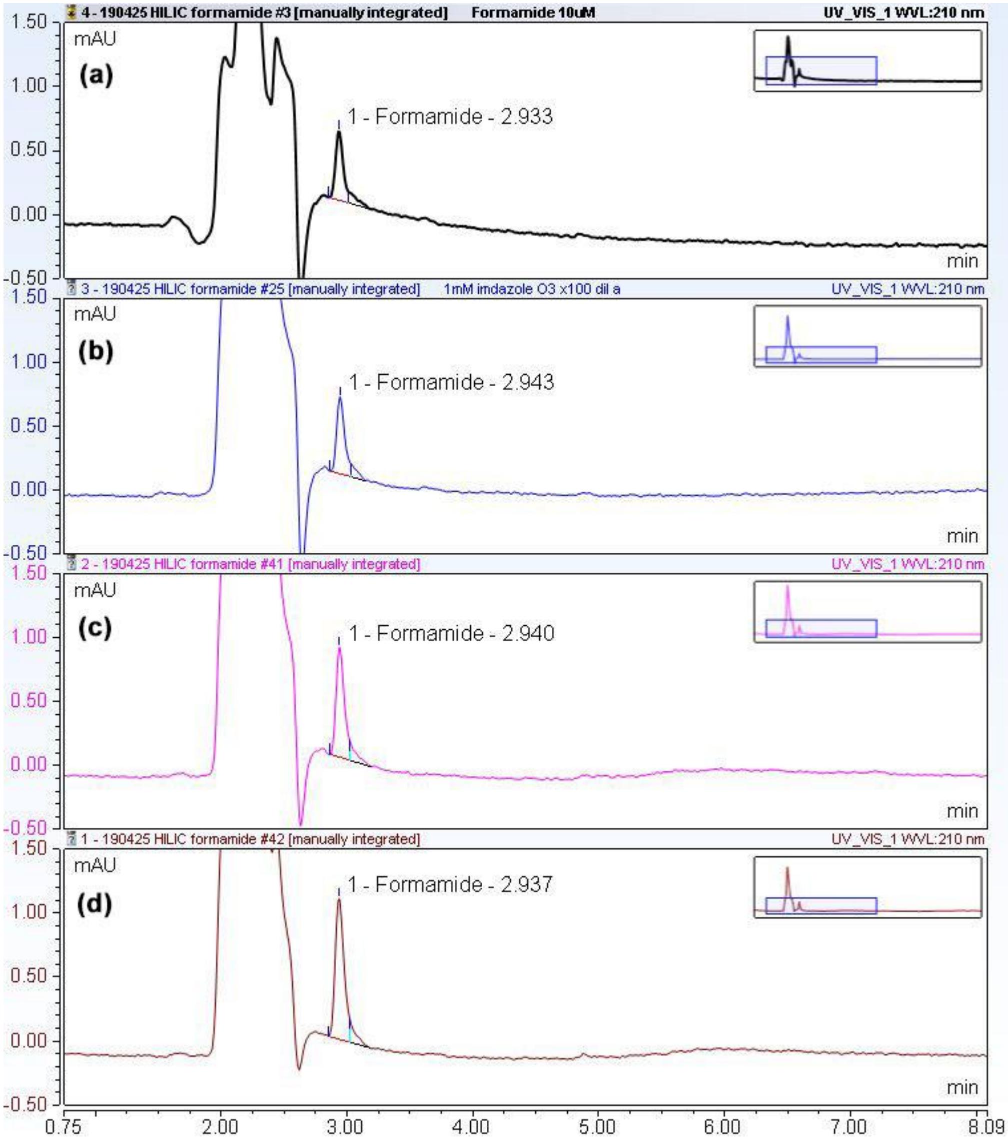

Figure S4. Stacked HPLC-UV chromatograms for (a) a 10 µM formamide standard, (b) an ozonated imidazole solution at $[O_3]/[\text{imidazole}]_0$ ~ 1, (c) the ozonated imidazole solution after the addition of a 5 µM formamide standard, and (d) the ozonated imidazole solution after the addition of a 10 µM formamide standard. The dead volume time of the column was 2.65 min and the retention time of formamide was at 2.94 min.

GC-MS for formamide. The formation of formamide from the imidazole-ozone reaction was additionally confirmed by GC-MS. Because of very low sensitivity of formamide by the GC-MS method (LOQ = 3.3 mM) and lack of extraction methods for formamide, the method was applied only once and thereafter no longer applied for further quantifications. To yield high production of formamide suitable for the GC-MS method, an ozonation experiment was carried out by using high initial concentrations of imidazole (1 mM) and *t*-butanol (1 M) prepared in 1 L of ultrapurified water by directly sparging ozone-containing gas to the imidazole solution with an oxygen gas flow of 0.02 NL min^{-1} and ozone generator power of 30 % (BMT MESSTECHNIK GMBH, BMT 803 BT). After 90 min of ozonation, when a complete abatement of imidazole was confirmed by HPLC-UV, the resulting solution was further processed by an evaporator (Büchi Syncore® Analyst) with preset operating parameters (heating temperature of 40 °C, cooling temperature of 15 °C, target pressure of 45 mbar over 3 hours, and 230 RPM) to remove *t*-butanol and subsequently by a lyophilizer (STERIS, LYOVAC GT 2-E) to remove the remaining water in the ozonated solution. The resulting particles were dissolved in 0.7 mL dimethylformamide and analyzed by GC-MS equipped with a Restek-Stabilwax column (60m, 0.32mm I.D., 1 µm d_f, Restek) by injecting 1 µL in the splitless mode with an inlet temperature of 220 °C. The column oven was initially at 100 °C for 1 min, ramped to 180 °C between 1 min and 9 min, held at 180 °C between 9 min and 24 min, ramped to 220 °C between 24 min and 25 min, and held at 220 °C until 30 min. After separation, formamide was detected by a Thermo Scientific DSQ II mass spectrometer with positive SIM mode. A quantification ion for formamide was m/z = 45. No internal standards were applied. The GC-MS chromatograms of the formamide standard solutions and the ozonated imidazole solution further treated by evaporation and lyophilization are shown in Figure S5. The concentration of formamide present in the ozonated sample was determined to be 2.4 mM based on the calibration of peak areas ($R^2 = 0.98$). This corresponds to 0.0017 mmol of formamide (by multiplying the volume of added dimethylformamide, 0.7 mL), which is 0.17 % of the initial amount of imidazole of 1 mmol (1 mM imidazole prepared in 1 L of ultrapurified water). The determined yield may underestimate the actual amount of formamide formed during the ozonation, because formamide could be degraded or evaporated during evaporation and lyophilization.

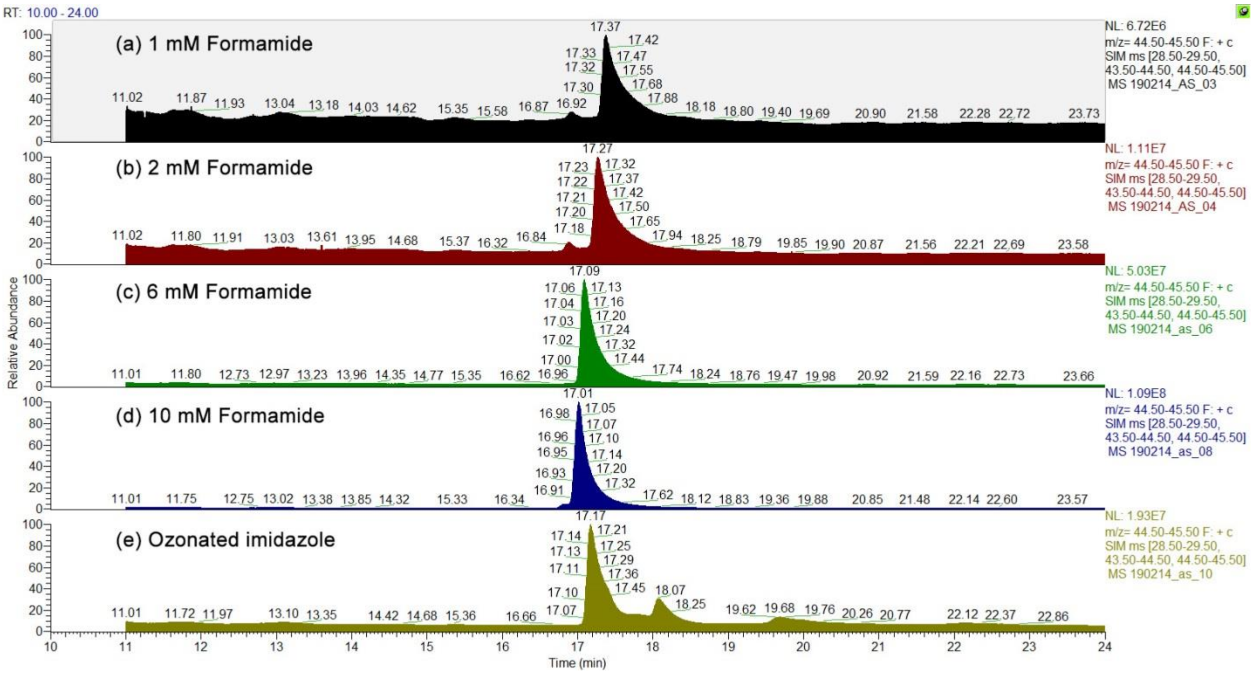

Figure S5. Stacked GC-MS chromatograms of (a) – (d) formamide standard solutions and (e) an ozonated imidazole solution treated by evaporation and lyophilization. The intensities of the highest peaks of (a) – (e) are 6.72 × 10^6, 1.11 × 10^7, 5.03 × 10^7, 1.09 × 10^8, and 1.93 × 10^7.

UV-photolysis−chemiluminescence for total N-nitrosamines. Ozonated pyrazole and 1-benzylpyrazole samples (parent concentration 100 µM) were analyzed by a UV-photolysis−chemiluminescence system[10] to determine total *N*-nitrosamines (TONO). The total *N*-nitrosamine standards were prepared from a mix comprising *N*-nitrosodimethylamine (NDMA), *N*-nitrosodiethylamine (NDEA), *N*-nitrosodipropylamine (NDPA), *N*-nitrosodibutylamine (NDBA), *N*-nitrosodiphenylamine (NDPhA), *N*-nitrosopiperidine (NPIP), *N*-nitrosopyrolidine (NPYR), and *N*-nitrosomorpholine (NMOR). A signal of the lowest concentration of the standard (0.4 µM) is shown in Figure S6.

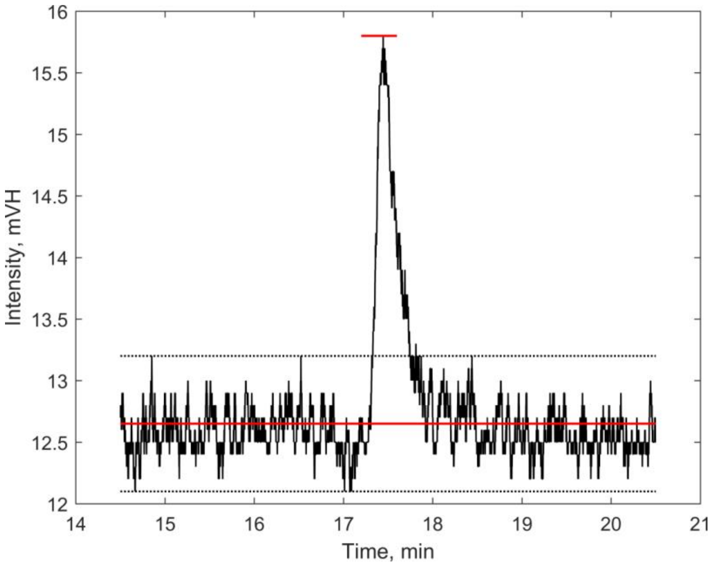

Figure S6. Example of a chemiluminescence signal of a 0.4 µM total *N*-nitrosamines standard in ultrapurified water. The signal-to-noise was 5.7. LOQ calculated based on the signal-to-noise was 0.7 µM by the equation of LOQ = [concentration of standard]/[signal-to-noise] × 10.

OPD derivatization followed by HPLC-DAD for glyoxal. Glyoxal in the ozonated samples (parent concentration 1 mM) was analyzed by a derivatization method using *o*-phenylendiamine (OPD).[13] Derivatization was performed by adding sodium hydroxide to 10 mL of the ozonated sample to make the solution alkaline and then by mixing it with 1 mL of the OPD solution prepared by dissolving 0.5 g of OPD in 100 mL of ultrapurified water. The mixture was heated at 60 °C for 3 h. After cooling, the derivatized product, quinoxaline, was determined by HPLC-DAD (LC 20, Shimadzu). The instrument was equipped with a C18 column (Prontosil, NC-04, 250 mm x 4.0 mm I.D., 5.0 µm, Bischoff). 50 µL of the derivatized solution was separated by a water/acetonitrile gradient system (35% ACN/ 5 min, 45% ACN/ 10 min, 100% ACN) with a flow rate of 0.5 mL min^{-1} for the ozonated imidazole and pyrazole samples. For the ozonated pyrrole samples, a water/methanol gradient system was used (20% MeOH/ 2 min, 80% MeOH/ 5 min). Quinoxaline was quantified by UV detection at 380 nm.

Text S5. Analytical methods for reactive oxygen species

This section describes the analytical methods used for quantifying reactive oxygen species (singlet oxygen, hydroxyl radical, and hydrogen peroxide) formed during the azole-ozone reactions.

Singlet oxygen. The formation of $^1O_2$ formed during the azole-ozone reactions was quantified by detecting the phosphorescence emitted by $^1O_2$ at 1270 nm by a near-infrared photomultiplier tube (NIR-PMT, H10330B-45, Hamamatsu). The setup is described in detail in a previous study.[14] The $^1O_2$ signals were calibrated by the reaction of triethylamine with ozone ([triethylamine] = 2 mM and [ozone] = 5 – 50 µM, as initial concentrations), which forms $^1O_2$ with a 70% yield.[14] The calibration reaction needs similar reaction kinetics to the azole-ozone reactions, because the shape of $^1O_2$ signals strongly depends on the kinetics of $^1O_2$ formation and could affect the peak integration and quantification.[14] Therefore, the calibration was performed at pH 10 (achieved by 20 mM carbonate buffer) where the triethylamine reacts with ozone with a second-order rate constant > 10^5 M^{-1} s^{-1}, similar to the apparent second-order rate constants of the azole-ozone reactions at pH 7. The calibration reaction by hydrogen peroxide and hypochlorous acid, applied in previous studies,[14,15] could not be used, because of its lower reactivity (maximum k ~ 3×10^3 M^{-1} s^{-1} at around pH 10).[16] The calibration curve is shown in Figure S7. The azole-ozone reactions were carried out under azole-excess conditions where [azole] = 2 mM or 3 mM and [ozone] = 90 – 100 µM as initial concentrations. 1 M *t*-butanol was added and the pH was maintained at pH 7 – 8 by 20 mM phosphate buffer. The results are summarized in Table S7 and examples of $^1O_2$ signals are shown in Figure S8.

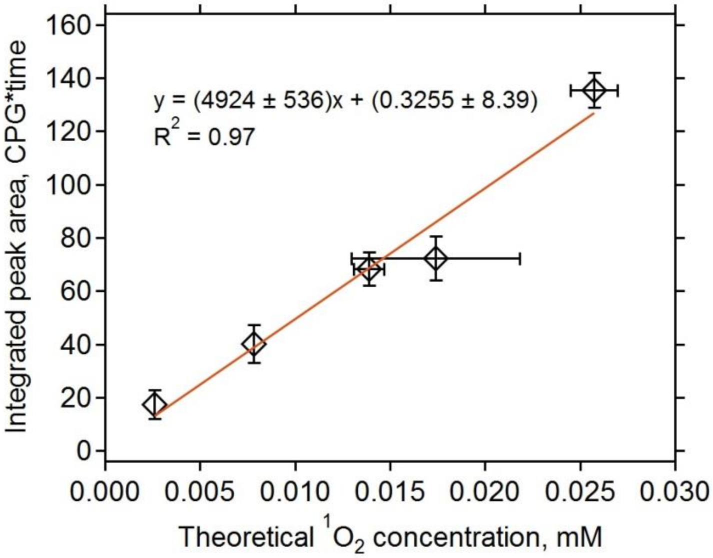

Figure S7. Integrated $^1O_2$ signals as a function of the theoretical concentrations of $^1O_2$ formed during the reaction of triethylamine with ozone, producing a 70% yield of $^1O_2$ at pH 10. Data points are average values of five individual measurements. Conditions: [triethylamine]$_0$ = 2 mM, [ozone]$_0$ = 5 µM – 50 µM, and pH 10 (20 mM carbonate buffer).

Table S7. Measuring conditions and $^{1}O_2$ yields of the azole-ozone reactions. All reactions were performed in presence of 1 M *t*-butanol. Each condition was repeated at least five times and the average values ± standard deviations are shown in bold at the last row for each condition.

	$^{1}O_2$ Measuring conditions			**Results**		
Compound	**Concentration, mM[a]**	**O_3, mM[a]**	**pH**	**Peak area**	**$^{1}O_2$, mM**	**$^{1}O_2/O_3$**
Pyrrole	3	0.101	7.3	63.27	0.0128	13%
		0.094		42.96	0.0087	9%
		0.098		65.51	0.0132	14%
		0.101		49.58	0.0100	10%
		0.096		50.34	0.0102	11%
		0.098			**0.0110 ± 0.0020**	**(11 ± 2)%**
Imidazole	2	0.096	7.6	0.70	0.00008	0.08%
		0.089		1.08	0.00015	0.17%
		0.086		0.70	0.00008	0.09%
		0.087		0.77	0.00009	0.10%
		0.089[b]		0.88	0.00011	0.13%
		0.089[b]		0.86	0.00011	0.12%
		0.089			**0.00010 ± 0.00003**	**(0.12 ± 0.03)%**
Pyrazole	3	0.096	7.5	8.56	0.00167	1.7%
		0.096		8.64	0.00169	1.8%
		0.088		8.49	0.00166	1.9%
		0.091		8.98	0.00176	1.9%
		0.093[b]		8.19	0.00160	1.7%
		0.093			**0.00167 ± 0.00006**	**(1.8 ± 0.1)%**

[a]concentration of the compound, [b]the original measured concentration was missing and therefore replaced by the average value of the other ozone concentrations measured for the same condition.

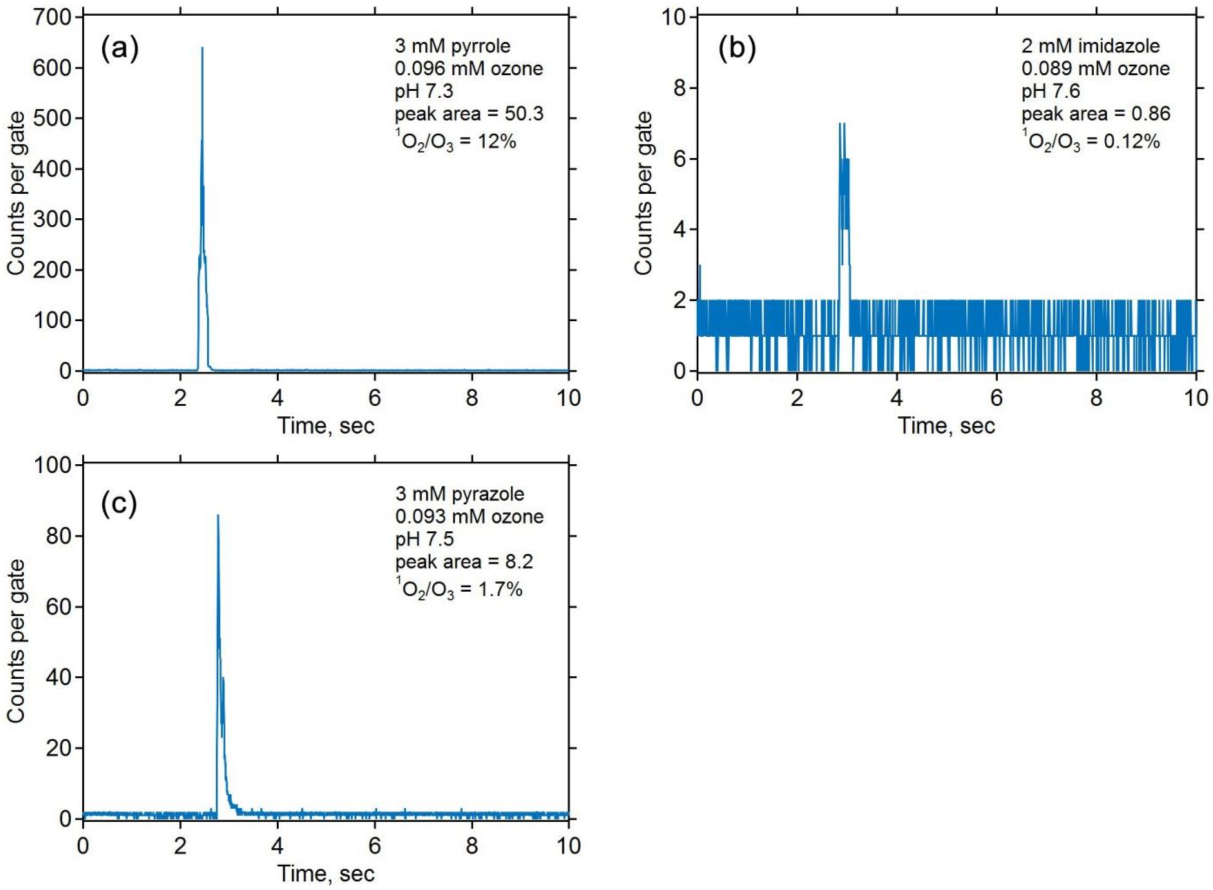

Figure S8. Examples of $^1O_2$ signals for the reactions of (a) pyrrole, (b) imidazole, and (c) pyrazole with ozone.

Hydroxyl radical. The concentrations of $^\bullet$OH formed during the reactions of pyrrole, imidazole, and pyrazole with ozone were quantified by using the $^\bullet$OH scavenger *t*-butanol. An azole solution containing 1 mM azole and 0.5 M *t*-butanol was prepared at pH 7 (5 mM phosphate buffer). Additionally, an azole solution containing 1 mM azole and 0.1 M *t*-butanol was prepared at pH 2 (by adding sulfuric acid) or at pH 11 (by adding sodium hydroxide) to investigate the pH effect on $^\bullet$OH formation. Varying doses of ozone (30 µM – 300 µM) were applied to the solution. After the reaction, formaldehyde, a product of the reaction of *t*-butanol with $^\bullet$OH, was quantified by the Hantzsch method[3] which derivatizes formaldehyde with acetylacetone and ammonium acetate and measures the absorbance of the derivatized product (diacetyldihydrolutine) at the wavelength of 412 nm (ε = 7700 M^{-1} cm^{-1}). The $^\bullet$OH concentrations were estimated by doubling the formaldehyde concentrations based on the previously reported formaldehyde yield of ~50%.[17] The determined $^\bullet$OH concentrations as a function of the ozone doses for the azole-ozone reactions are shown in Figure S9.

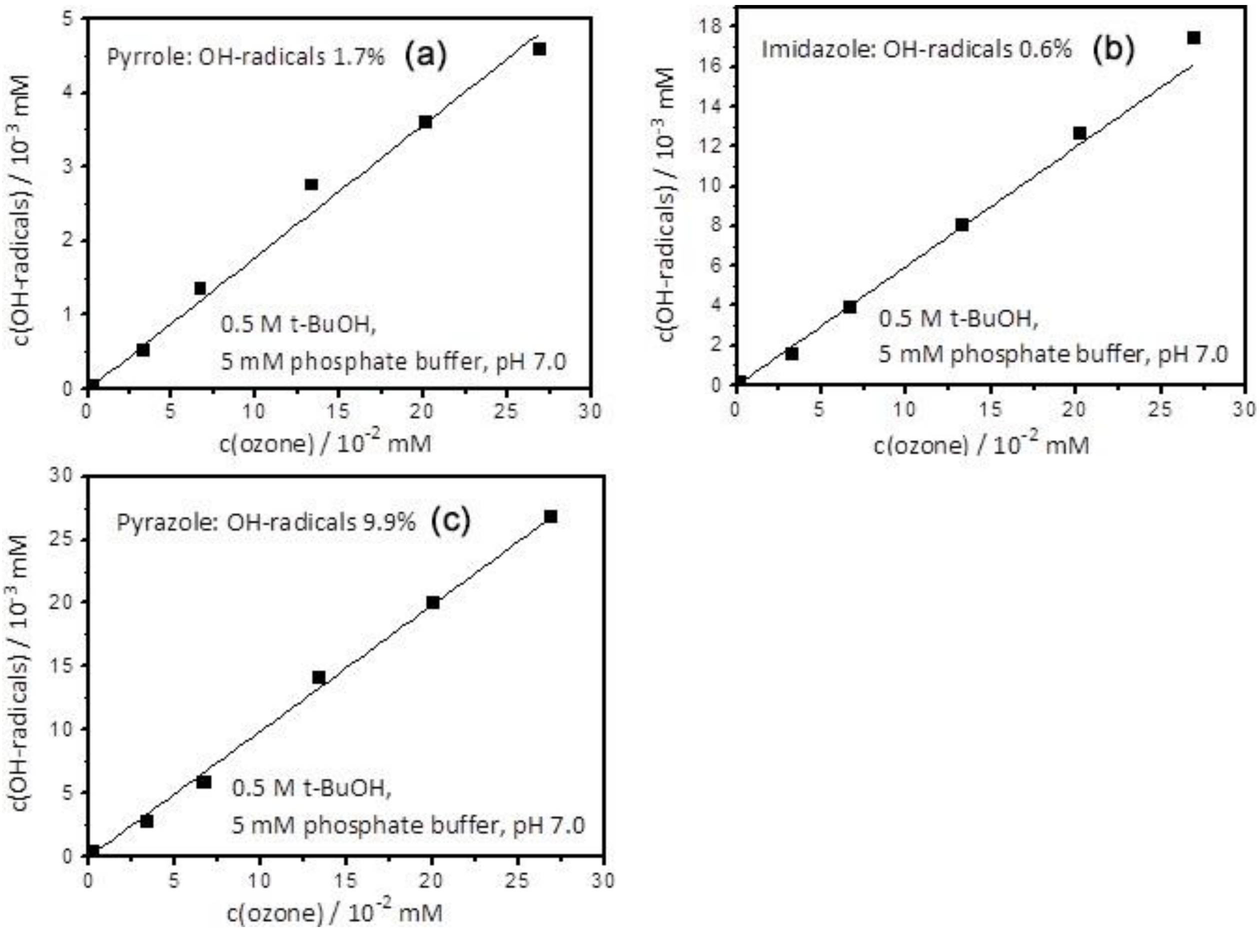

Figure S9. $^{\bullet}$OH formation during the reactions of (a) pyrrole, (b) imidazole, and (c) pyrazole with ozone (initial azole concentration = 1 mM). Symbols indicate the determined $^{\bullet}$OH concentrations and lines are the linear regression of the data for ozone doses ranging from 30 µM to 300 µM. Numbers in percentage are $^{\bullet}$OH yields obtained by the slopes of the linear regression.

Hydrogen peroxide. An azole solution containing 1 mM azole and 0.5 M *t*-butanol was prepared at pH 7 (5 mM phosphate buffer). Additionally, an azole solution containing 1 mM azole in absence of a $^{\bullet}$OH scavenger was prepared at pH 2 (by adding sulfuric acid) or at pH 11 (by adding sodium hydroxide) to investigate the pH effect on H_2O_2formation. Varying doses of ozone (30 µM – 300 µM) were applied to the solution. After the reaction, H_2O_2 was quantified spectrophotometrically with Allen's reagent (molybdate-activated iodide).[18,19] H_2O_2 oxidizes molybdate activated iodide ions to iodine, which can be detected as I_3^- according to the following equations:

$$H_2O_2 + 2I^- \rightarrow I_2 + 2OH^-$$

$$I_2 + I^- \rightleftarrows I_3^-$$

The quantitative determination of H_2O_2 was achieved by adding the following solutions to UV-cells (1 cm path length): 1 mL of Allen´s reagent A (1 g NaOH + 33 g KI + 0.1 g $(NH_4)_6Mo_7O_{24} \cdot H_2O$ filled up to 500 mL ultrapurified water), 1 mL of Allen´s reagent B (10 g potassium hydrogen phthalate (KHP) dissolved in 500 mL ultrapurified water), and 1 mL of sample. After rapid mixing, the H_2O_2 concentrations were derived by spectrophotometrically measuring the absorbance at 350 nm (ε_{350nm} = 25,500 M^{-1} cm^{-1}). The H_2O_2 measurements were carried out in presence and absence of *t*-butanol, both of which show similar results (Figure S10). It has to be noted that oxidation of iodide may also be induced by other peroxides. Organic peroxides can be formed *via* recombination of oxyl radicals. These oxyl radicals can either be formed by $HO_2^•$ cleavage of an ozone adduct after insertion, or from tetroxide decay. These reactions have rarely been reported, indicating that they may be of minor importance. Yet, such interferences can also not be fully excluded by other methods for H_2O_2 determination such as peroxidase catalyzed oxidation of *N*,*N*-diethyl-*p*-phenylenediamine (DPD).[20]

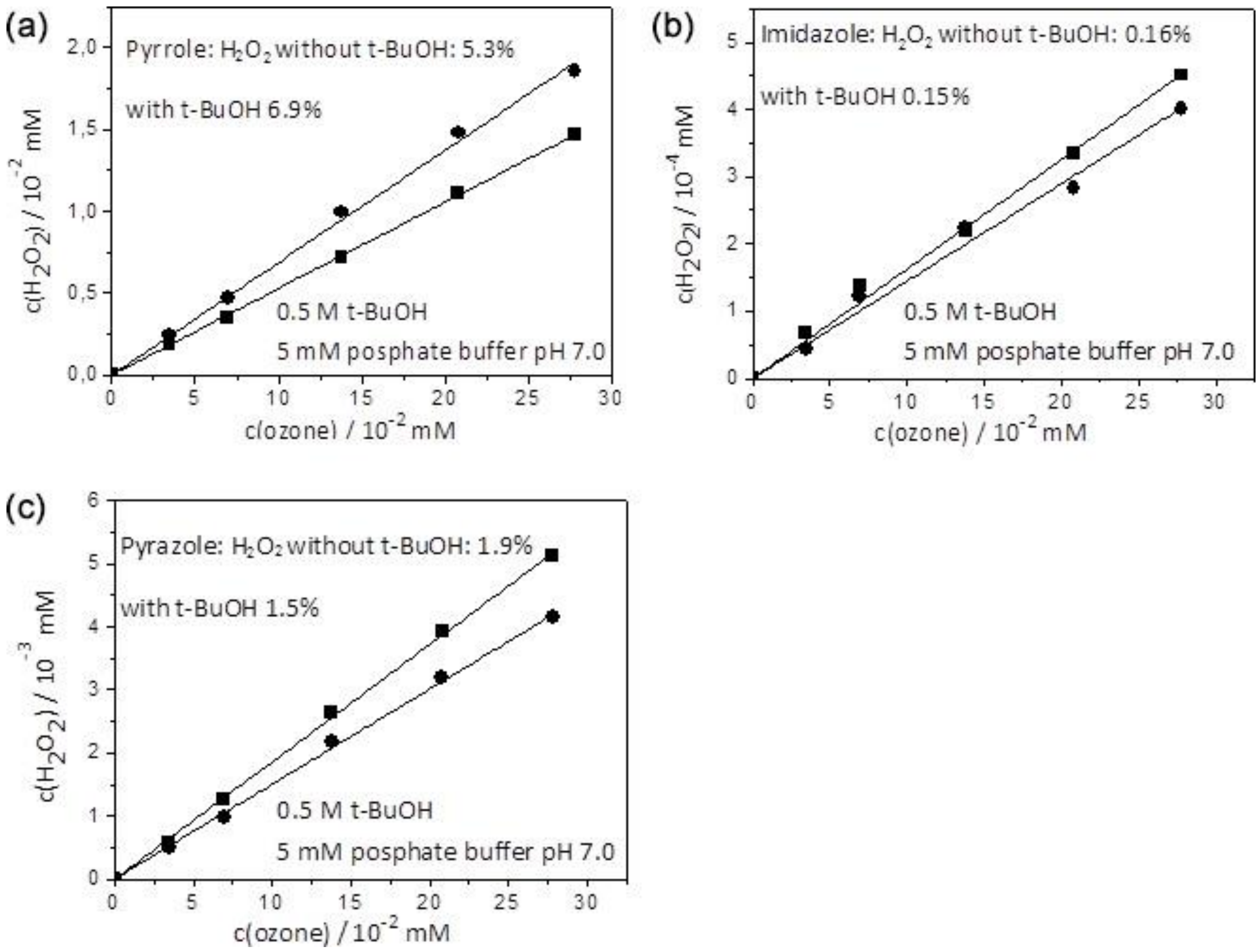

Figure S10. H_2O_2 formation during the reactions of (a) pyrrole, (b) imidazole, and (c) pyrazole with ozone (initial azole concentration = 1 mM). Symbols indicate the determined H_2O_2 concentrations with *t*-butanol (circle) and without *t*-butanol (square) and lines are the linear regression of the data for ozone doses ranging from 30 µM to 300 µM. Numbers in percentage are H_2O_2 yields obtained by the slopes of the linear regression.

Text S6. Detailed methods of quantum chemical computations

All computations were performed with Gaussian09 vD.01.[21] Geometry optimizations used the LC-ωPBE/6-31+G(d,p)[22] method together with the implicit SMD[23] model to account for aqueous solvation. The nature of all stationary structures was verified by normal mode analysis. Internal Reaction Coordinate[24] (IRC) calculations were performed to verify the connectivity of transition structures on the potential energy surface (PES). Energy differences are reported with respect to separate reactants ozone and pyrrole as follows: Electronic energy differences were evaluated with the LC-ωPBE/def2-tzvppd[22,25] model chemistry in combination with the SMD solvation model, using the structures described above. Additional electronic energy calculations were performed with the M06-2X/tzvppd model chemistry,[26] also using the LC-ωPBE-optimized geometries. All calculations used the restricted Kohn-Sham approach for singlet systems, unless mentioned otherwise. For doublet systems, unrestricted Kohn-Sham was used for geometry optimization and frequency calculations, and unrestricted open shell Kohn-Sham for single point energy calculations with the tzvppd basis set. For doublet species, the energetic difference between unrestricted and restricted open shell calculations was 4 kcal mol^{-1} in the most pronounced case, and did not affect the mechanistic interpretation.

Rotational, vibrational, and translational contribution to the Gibbs free energy were estimated with the harmonic oscillator/rigid rotor models at the LC-ωPBE/6-31+G(d,p) level at 1 atm and 298.15 K, and were modified with the GoodVibes software package using standard options. All vibrational frequencies were scaled by a factor of 0.9367,[27] and vibrational frequencies below 100 cm^{-1} were treated with the free rotor approach.

The accuracy of the free energy differences can be expected to be somewhere in a 5-10 kcal mol^{-1} range, owing to cumulative errors of the electronic structure methods and the solvation models. The absolute error in the free energy difference is expected to be larger, since describing ozone additions is challenging for density functional theory methods.[28,29] However, this is the result of an error in the description of ozone, and this systematic error will propagate through all results. Conversely, when comparing molecules with similar charge distribution and bonding pattern, or comparing reactions of the same type, the error should be < 5 kcal mol^{-1}. Three types of energies are reported: LC- ωPBE energies at 0 K that include zero-point vibrational energies, LC- ωPBE Gibbs free energies at 298 K, and M06-2X Gibbs free energies at 298 K. Throughout the reaction schemes presented from Figure S27 to Figure S32, and presented in Figure S36, these highlight that the results especially for charged species strongly depend on the choice of density functional and on the inclusion of temperature effects. For evaluating the feasibility of each step, it should be most instructive to compare all three types of energy to the preceding molecule. In the main text, the LC- ωPBE Gibbs free energies at 298 K were used for discussion.

The explored reaction pathways involve the addition of HO^-, deprotonation by HO^-, or protonation. To treat this in an energetically consistent fashion, the given energies refer to a reference energy corresponding to the addition of two H_2O molecules to the system. These have to undergo proton transfer to form H_3O^+ and HO^-, which are the species used in actual reactions. In the presented schemes, every time a reaction with HO- is involved, it is preceded by the reaction:

$2\ H_2O \rightarrow H_3O^+ + HO^-$

It should be noted that the SMD implicit solvation model underestimates the free energies of solvation of H_3O^+ and HO^- by 6 kcal mol^{-1} and 10 kcal mol^{-1}, respectively, owing to the strong specific interaction of these species with solvent molecules. This leads to a miss-estimation of the free energy differences associated with these reactions.

Figure S27, Figure S28, Figure S29, Figure S30, Figure S31, Figure S32, and Figure S36 depict mechanisms that are based on these quantum chemical computations. These are annotated with reaction energies, where the energetic references are always isolated molecules of ozone and pyrrole or imidazole. For each species, the three energies given are: LC- ωPBE/def2-tzvppd//LC- ωPBE/6-31+G(d,p), including (1) zero-point vibrational energy, (2) thermal corrections to Gibbs free energy, and (3) M06-2X/def2-tzvppd//LC- ωPBE/6-31+G(d,p) including thermal corrections to the Gibbs free energy. Transition structures (first order saddle points on the potential energy surface) are marked with square brackets and a double dagger. Usually, chemical species should be connected by a transition structure. If this is not drawn, then calculations were not carried out. If arrows connecting stable species and transition structures are dotted, then internal reaction coordinate (IRC) calculations did not succeed for technical reasons. The connectivity was then concluded from visualizing the imaginary vibrational mode of the transition structure, and from “relaxed scan” calculations that were used to locate the transition structure in the first place. Relaxed scans vary a selected bond distance between two atoms systematically and keep it fixed in each step, while the geometry of the remainder of the system is optimized with respect to the potential energy. Thus, if the chosen bond distances closely correspond to the reaction coordinate, these calculations give an indication of the connectivity on the PES and possible product structures.

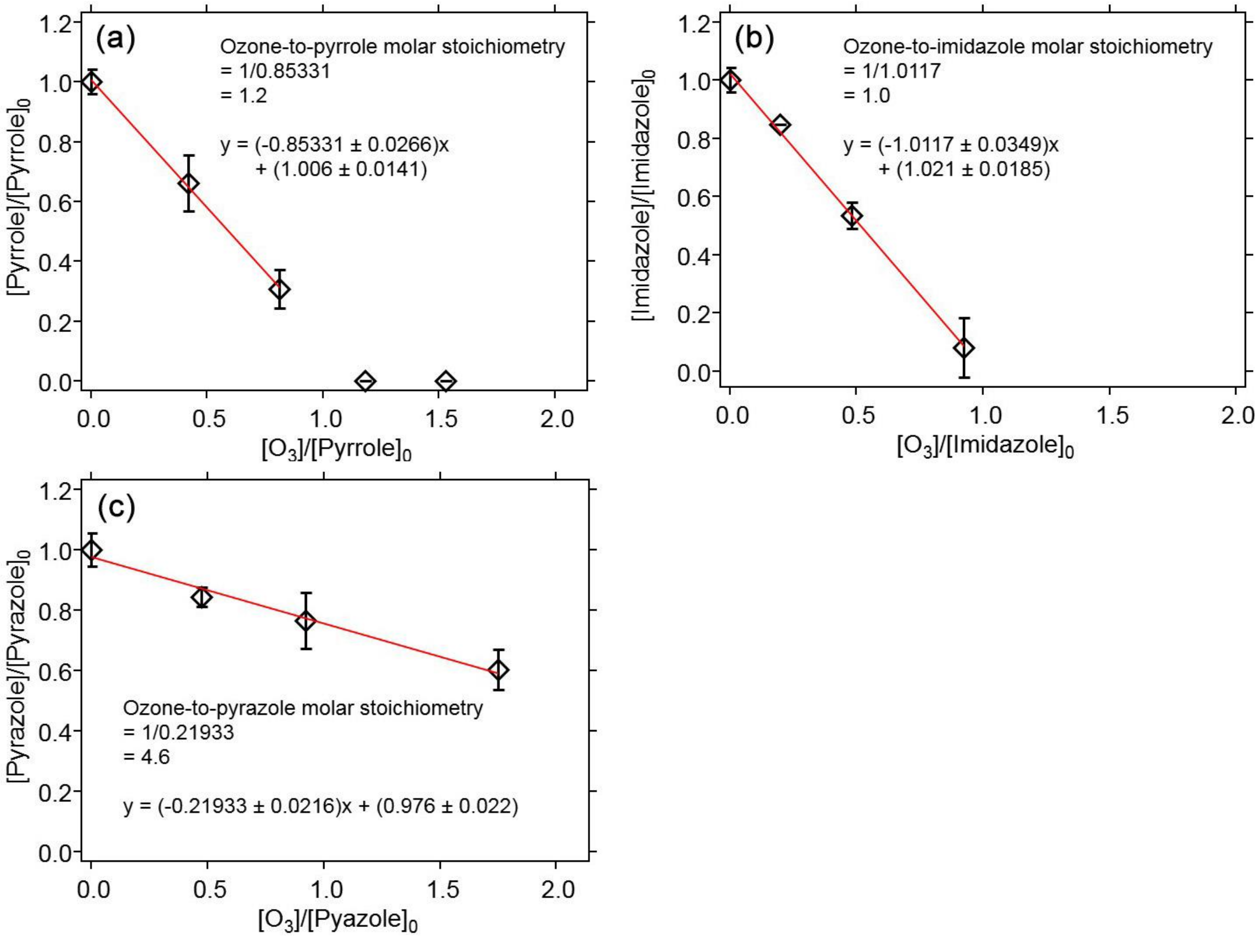

Figure S11. Ozone:azole molar stoichiometry calculated by inverting the slopes from linear regressions of the measured azole concentrations as a function of the molar ratio of [O$_3$]/[azole]$_0$: (a) Pyrrole, (b) imidazole, (c) pyrazole. All measurements were carried out in presence of 50 mM *t*-butanol at pH 7 (10 mM phosphate buffer). The initial azole concentrations were 100 – 110 µM.

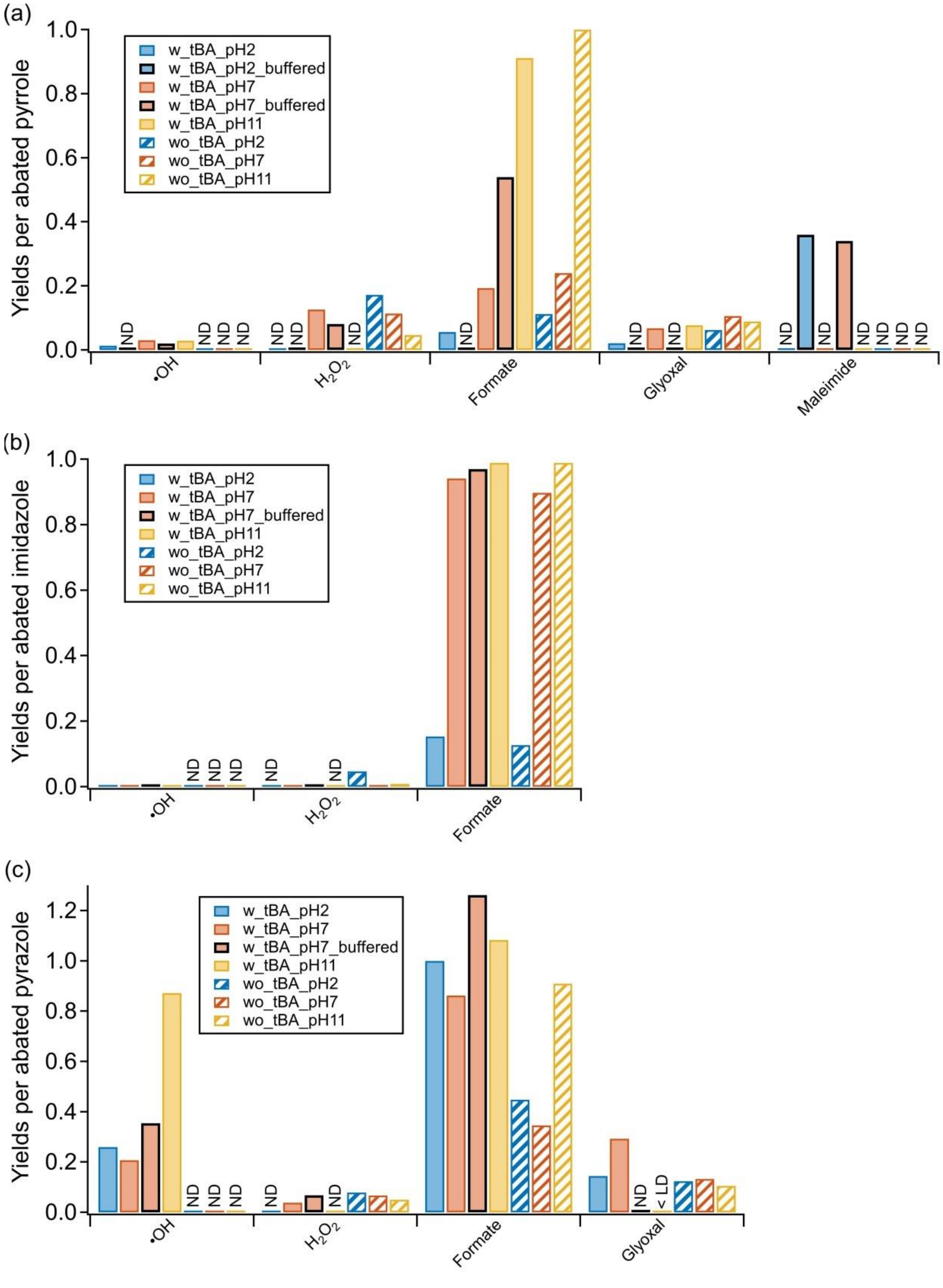

Figure S12. Product yields measured under various pH and $^{\bullet}$OH scavenging conditions for the reactions of (a) pyrrole, (b) imidazole, and (c) pyrazole with ozone. The yields are expressed with regard to the abatement of azole under the corresponding reaction condition as shown in Table S8. Blue, red, and yellow bars indicate pH 2, 7, and 11, respectively. Solid and hashed patterns indicate the presence and absence of $^{\bullet}$OH scavenger, respectively. Experiments were carried out with or without buffering agents and the results obtained under the buffered condition (10 mM phosphate buffer for pH 2 and 7) are shown as bars with black edges.

Table S8. Reaction stoichiometry and product yields for the reactions of pyrrole, imidazole, and pyrazole with ozone at pH 2, 7, and 11 in presence and absence of *t*-butanol. The yields are expressed as the specific ozone consumption ($\Delta[X]/\Delta[O_3]$) or relative to the abatement of azole ($\Delta[X]/\Delta[Azole]$).

azole	**product (X)**	**X type**	**pH**	**Buffer**	***t*-butanol**	**O_3:azole stoichiometry**	**$\Delta[X]/\Delta[O_3]$**	**$\Delta[X]/\Delta[azole]$**
pyrrole	$^\bullet$OH	ROS	2.0	none	presence	1.9	0.013	0.025
	$^\bullet$OH	ROS	7.3	none	presence	1.8	0.017	0.030
	$^\bullet$OH	ROS	11.0	none	presence	1.8	0.016	0.029
	$^\bullet$OH	ROS	7.0	PBS 5mM	presence	1.2	0.017	0.020
	H_2O_2	ROS	2.0	none	absence	1.7	0.10	0.172
	H_2O_2	ROS	7.3	none	absence	2.0	0.057	0.114
	H_2O_2	ROS	11.0	none	absence	1.9	0.025	0.047
	H_2O_2	ROS	7.3	none	presence	1.8	0.072	0.126
	H_2O_2	ROS	7.0	PBS 5mM	presence	1.2	0.069	0.081
	formate	TP_C	2.0	none	absence	1.7	0.065	0.112
	formate	TP_C	7.3	none	absence	2.0	0.12	0.240
	formate	TP_C	11.0	none	absence	1.9	0.53	1.000
	formate	TP_C	2.0	none	presence	1.9	0.056	0.108
	formate	TP_C	7.3	none	presence	1.8	0.11	0.193
	formate	TP_C	11.0	none	presence	1.8	0.51	0.911
	fomate	TP_C	7	PBS 10mM	presence	1.2	0.46	0.539
	glyoxal	TP_C	2.0	none	absence	1.7	0.036	0.062
	glyoxal	TP_C	7.3	none	absence	2.0	0.053	0.106
	glyoxal	TP_C	11.0	none	absence	1.9	0.047	0.089
	glyoxal	TP_C	2.0	none	presence	1.9	0.021	0.040
	glyoxal	TP_C	7.3	none	presence	1.8	0.039	0.068
	glyoxal	TP_C	11.0	none	presence	1.8	0.043	0.077
imidazole	$^\bullet$OH	ROS	2	none	presence	1.4	0.0007	0.001
	$^\bullet$OH	ROS	7.4	none	presence	1.2	0.0009	0.001
	$^\bullet$OH	ROS	11	none	presence	1.1	0.0009	0.001
	$^\bullet$OH	ROS	7	PBS 5mM	presence	1.0	0.006	0.006
	H_2O_2	ROS	2	none	absence	1.3	0.037	0.047
	H_2O_2	ROS	7.4	none	absence	1.1	0.0019	0.002
	H_2O_2	ROS	11	none	absence	1.1	0.0075	0.008
	H_2O_2	ROS	7.4	none	presence	1.2	0.0017	0.002
	H_2O_2	ROS	7	PBS 5mM	presence	1.0	0.0015	0.001
	formate	TP_C	2	none	absence	1.3	0.099	0.127
	formate	TP_C	7.4	none	absence	1.1	0.78	0.897
	formate	TP_C	11	none	absence	1.1	0.91	0.989
	formate	TP_C	2	none	presence	1.4	0.11	0.153
	formate	TP_C	7.4	none	presence	1.2	0.8	0.941
	formate	TP_C	11	none	presence	1.1	0.94	0.989
	formate	TP_C	7	PBS 10mM	presence	1.0	0.98	0.968
pyrazole	$^\bullet$OH	ROS	2	none	presence	3.7	0.070	0.259
	$^\bullet$OH	ROS	6.5	none	presence	3.4	0.061	0.207
	$^\bullet$OH	ROS	11.0	none	presence	8.3	0.105	0.872
	$^\bullet$OH	ROS	7.0	PBS 5mM	presence	4.6	0.077	0.354
	H_2O_2	ROS	2	none	absence	3.4	0.023	0.079
	H_2O_2	ROS	6.5	none	absence	4.2	0.016	0.067
	H_2O_2	ROS	11.0	none	absence	4.5	0.011	0.050
	H_2O_2	ROS	6.5	none	presence	3.4	0.011	0.038
	H_2O_2	ROS	7.0	PBS 5mM	presence	4.6	0.015	0.068
	formate	TP_C	2	none	absence	3.4	0.13	0.448
	formate	TP_C	6.5	none	absence	4.2	0.083	0.346
	formate	TP_C	11	none	absence	4.5	0.2	0.909
	formate	TP_C	2.0	none	presence	3.7	0.27	1.000
	formate	TP_C	6.5	none	presence	3.4	0.25	0.862
	formate	TP_C	11	none	presence	8.3	0.13	1.083
	formate	TP_C	7	PBS 10mM	presence	4.6	0.28	1.262
	glyoxal	TP_C	2	none	absence	3.4	0.04	0.124
	glyoxal	TP_C	6.5	none	absence	4.2	0.032	0.133
	glyoxal	TP_C	11	none	absence	4.5	0.023	0.105

	glyoxal	TP_C	2	none	presence	3.7	0.039	0.144
	glyoxal	TP_C	6.5	none	presence	3.4	0.085	0.293
	glyoxal	TP_C	11	none	presence	8.3	< LD	< LD

Text S7. NMR results – Identification of TP2, maleimide, and TP1 formed upon ozonation of pyrrole

This section presents assignments of ^{1}H and ^{13}C NMR data and NMR spectra overviews and expanded parts of the 1D ^{1}H, ^{1}H-NOESY, and ^{13}C, as well as the 2D, ^{1}H-^{13}C HSQC, ^{1}H-^{13}C HMBC, and ^{1}H-^{1}H DQF-COSY NMR spectra, analyzed to identify TP1, TP2, and maleimide, formed during the reaction of pyrrole with ozone.

The ^{1}H and ^{13}C NMR spectra of isolated products from ozonated pyrrole samples show many resonances from unknown products (indicated as "by-products" in Figure S14a, Figure S14b, Figure S15a, Figure S17a, and Figure S17b). Moreover, it seems that the broad resonances observed in the base of the ^{1}H NMR spectra originate from polymerized substances which had been formed during ozonation or during the sample work-up. Despite the large number of the unidentifiable signals in the NMR spectra, some characteristic ^{1}H and ^{13}C NMR chemical resonances were observed and successfully assigned to specific chemical structures (TP2, maleimide, and TP1, Figure S13). Two different sample work-up procedures were applied after ozonation: (1) only rotary evaporation until dryness, and (2) rotary evaporation followed by lyophilization (Text S4). Depending on the applied work-up (1) or (2), different product compositions were detected by the NMR analysis for the samples prepared under the same ozonation condition. Isolated solids by the work-up (1) contained TP2 and maleimide, whereas isolated solids by the work-up (2) mainly contained TP2 and TP1. TP2 could be identified as a main product regardless of the work-up procedures. The following sections discuss the assignments of ^{1}H and ^{13}C NMR chemical shifts to the identified products for NMR samples.

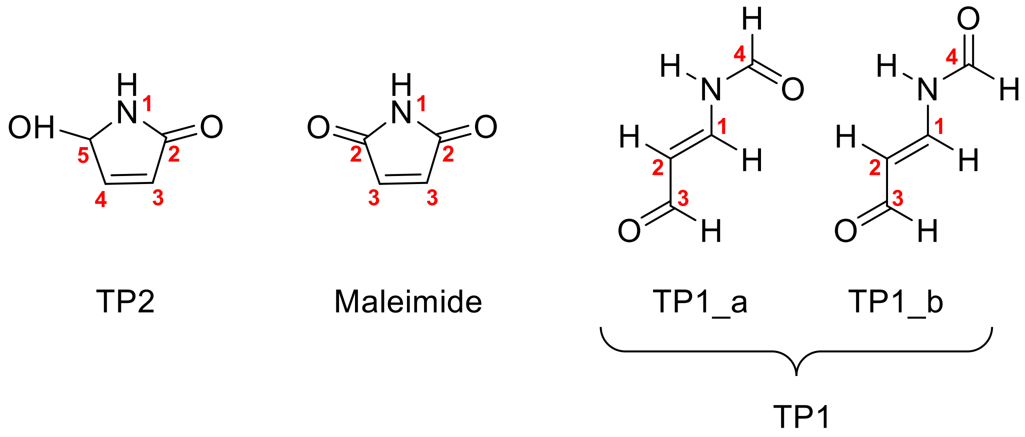

Figure S13. Chemical structures of TP2 (5-Hydroxy-1,5-dihydro-2H-pyrrol-2-one), maleimide, and TP1 (*N*-(3-oxo-1-propen-1-yl)formamide), isolated from the reaction of pyrrole with ozone. TP1_a and TP1_b are two stereoisomers of TP1 present in equilibrium. Positions used for NMR resonance assignments are indicated as red numbers.

1) *NMR identification of TP2 isolated by the work-up (1)*. The NMR data recorded in DMSO-d$_6$ for the NMR sample processed by the work-up (1) show one set of resonances that could be assigned to TP2. The full assignment of ^{1}H and ^{13}C NMR data to TP2 is shown in Table S9 and Figure S14. In the ^{1}H-^{1}H DQF-COSY NMR spectrum (Figure S14e), the cross signals observed between H-3, H-4, and H-5 prove that the three protons belong to the same spin system. Additionally, weak correlations of H-3, H-4, and H-5 to H-1 were detected (spectral region not shown in Figure S14e). From chemical shift reasons and from the ^{1}H-^{13}C HSQC correlation (Figure S14c), it is clear that position 5 of TP2 can be assigned to a R-**CH**(OH)-R group. From the NOESY NMR data (Figure S14f), it is clear that the NH group must be next to position 5 and subsequently H-4 (NOE to H-5) and H-3 (NOE to H-4 and coupling J_{34} = 5.7 Hz) could be assigned. All observed ^{1}H-^{13}C HMBC long-range correlations (Figure S14d and Table S9) support the proposed chemical structure. The NMR data of the same sample recorded in acetone-d$_6$ (Figure S15) shows considerably reduced amounts of resonances and is consistent with the assignments discussed above. The isolate was only partially soluble in acetone-d$_6$ and therefore the sample composition was different from the isolated dissolved in DMSO-d$_6$ (see Text S8).

Table S9. Assignments of ^{1}H and ^{13}C NMR data of extracted products from the reaction of pyrrole with ozone (TP2, maleimide, TP1_a, and TP1_b as shown in Figure S13) and the reference standard of maleimide.

			^{1}H NMR[c]				**^{13}C NMR[d]**		
Compound[a]	**Solvent[b]**	**Position[a]**	**δ^{1}H**	**Cp**	***J* [Hz]**	**No. H**	**δ^{13}C**	**mult.**	**Correlations observed: HMBC, DQF-COSY, NOESY (w = weak)[e]**
TP2	acetone-d_6	1	n.d.						**HMBC** (Figure S15c)**:** H-3 → C-(2, 4, 5); H-4 → C-(2, 3, 5); H-5 → C-(2, 3, 4)
		2					172.3	s	
		3	5.95	d(br)	5.8	1	128.4	d	
		4	6.99	d(br)	5.8	1	149.4	d	
		5	5.61	m		1	81	d	
TP2	DMSO-d_6	1	8.36	s(br)		1			**HMBC** (Figure S14d)**:** H-1 → C-(4w) (not shown); H-3 → C-(2, 4, 5); H-4 → C-(2, 3, 5); H-5 → C-(2, 3, 4)
		2					171.7	s	**DQF-COSY** (Figure S14e)**:** H-1 → H-(3w, 4w, 5w) (not shown in Figure S14e); H-3 → H-(1w, 4, 5); H-4 → H-(1w, 3, 5); H-5 → H-(1w, 3, 4)
		3	5.97	d(br)	5.7	1	127.3	d	**NOESY** (Figure S14f)**:** H-1 → H-(5); H-3 → H-(4); H-4 → H-(3, 5); H-5 → H-(1, 4)
		4	6.98	d(br)	5.7	1	149.4	d	
		5	5.44	m		1	79.9	d	
Maleimide	acetone-d_6	1	n.d.						**HMBC** (Figure S15c)**:** H-3 → C-(2, 3w)
		2					172.4	s	
		3	6.79	s		2	136.0	d	
Maleimide	DMSO-d_6	1	n.d.						**HMBC** (Figure S14d)**:** H-3 → C-(2, 3w)
		2					172.7	s	
		3	6.87	s		2	135.2	d	
Maleimide[f]	DMSO-d_6	1	10.9	s(br)		1			**HMBC** (Figure S16d)**:** H-3 → C-(2, 3w)
		2					172.7	s	
		3	6.87	s		2	135.2	d	

			^{1}H NMR[c]				^{13}C NMR[d]		
Compound[a]	**Solvent[b]**	**Position[a]**	**δ^{1}H**	**Cp**	***J* [Hz]**	**No. H**	**δ^{13}C**	**mult.**	**correlations observed: HMBC, DQF-COSY, NOESY (w = weak)[e]**
TP1_a	acetone-d$_6$	NH	10.3	s(br)		1			**HMBC (**Figure S17d-1**):** H-1 → C-(3, 4); H-3 → C-(2); H-4 → C-(1)
		1	7.89	dd	14.2/11.4	1	144.5	d	**DQF-COSY (**Figure S17e**):** H-1 → H-(2); H-2 → H-(1, 3); H-3 → H-(2)
		2	5.91	dd	14.2/8.1	1	115	d	
		3	9.48	dd	8.1	1	192.9	d	
		4	8.40	s		1	160.7	d	
TP1_b	acetone-d$_6$	NH	10.2	s(br)		1			**HMBC (**Figure S17d-1**):** H-1 → C-(3, 4); H-3 → C-(2)
		1	7.89	dd	n.d.	1	150.6	d	**DQF-COSY (**Figure S17e**):** H-1 → H-(2); H-2 → H-(1, 3); H-3 → H-(2)
		2	5.79	dd	13.7/8.0	1	113.2	d	
		3	9.38	dd	8.0	1	191.6	d	
		4	8.64	d(br)	8.7	1	164.9	d	

[a] Compound structures and numbering of positions are shown in Figure S13; [b] NMR solvent used, [c] “Cp” indicates coupling patterns described as s = singlet, d = doublet, dd = doublet of doublets, m = multiplet, br = broad; “No. H” indicates the number of hydrogens, [d] “mult.” Indicates multiplicities of carbons described as s = quaternary and d = doublet (= CH group). [e] numbers next to H- or C- indicate the positions as described in Figure S13. [f] a commercially available reference standard of maleimide

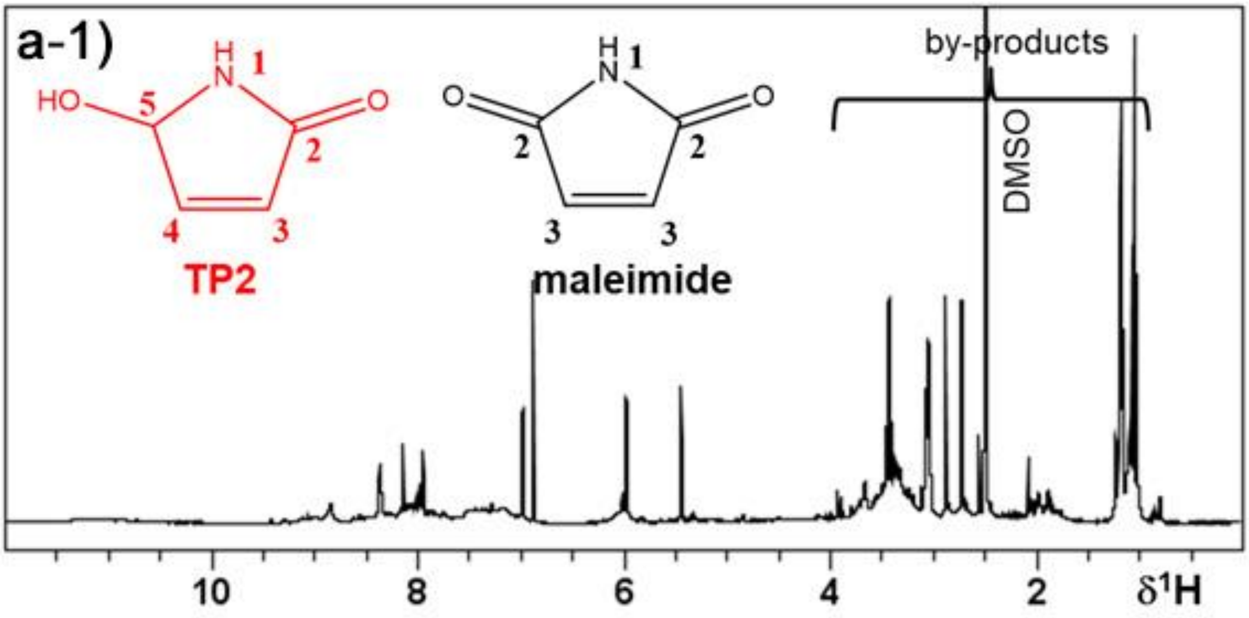
a-1)
H
N
1
HO
5
O
2
4
3
TP2
H
N
1
O
O
2
2
3
3
maleimide
by-products
DMSO
10
8
6
4
2
δ¹H

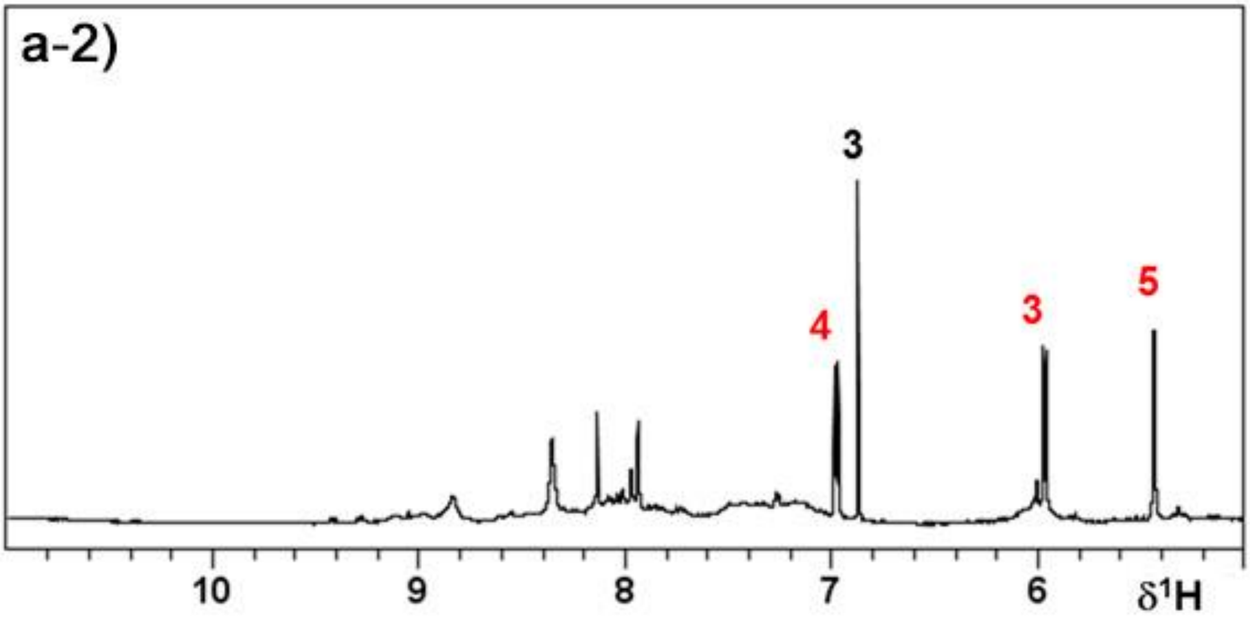
a-2)
3
4
3
5
10
9
8
7
6
δ¹H

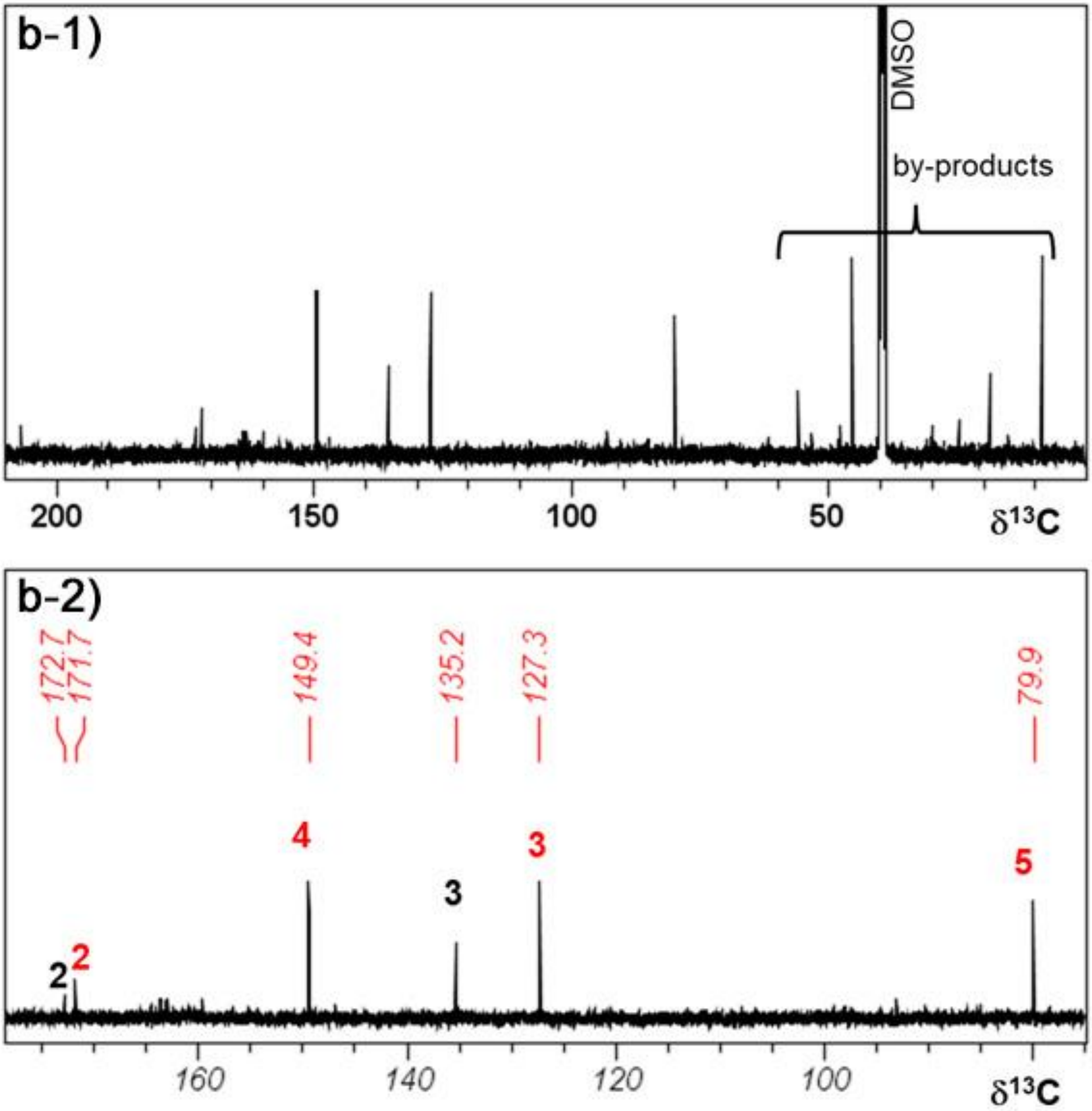
b-1)
DMSO
by-products
200
150
100
50
$\delta^{13}C$
b-2)
172.7
171.7
149.4
135.2
127.3
79.9
4
3
3
5
2
2
160
140
120
100
$\delta^{13}C$

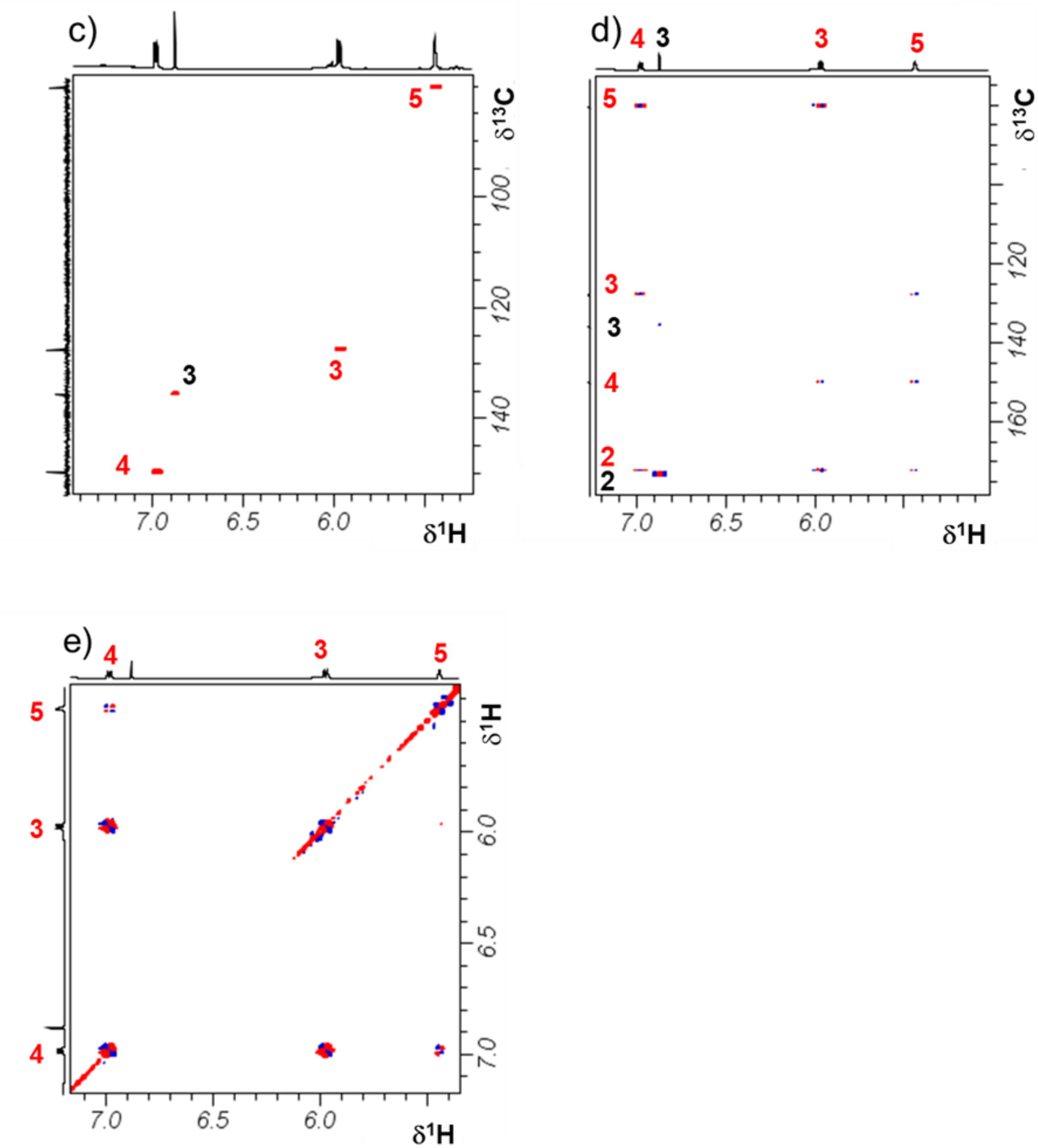
c)
5
3
3
4
δ13C
100
120
140
7.0
6.5
6.0
δ1H
d)
4
3
3
5
5
3
3
4
2
2
δ13C
120
140
160
7.0
6.5
6.0
δ1H
e)
4
3
5
5
3
4
δ1H
6.0
6.5
7.0
7.0
6.5
6.0
δ1H

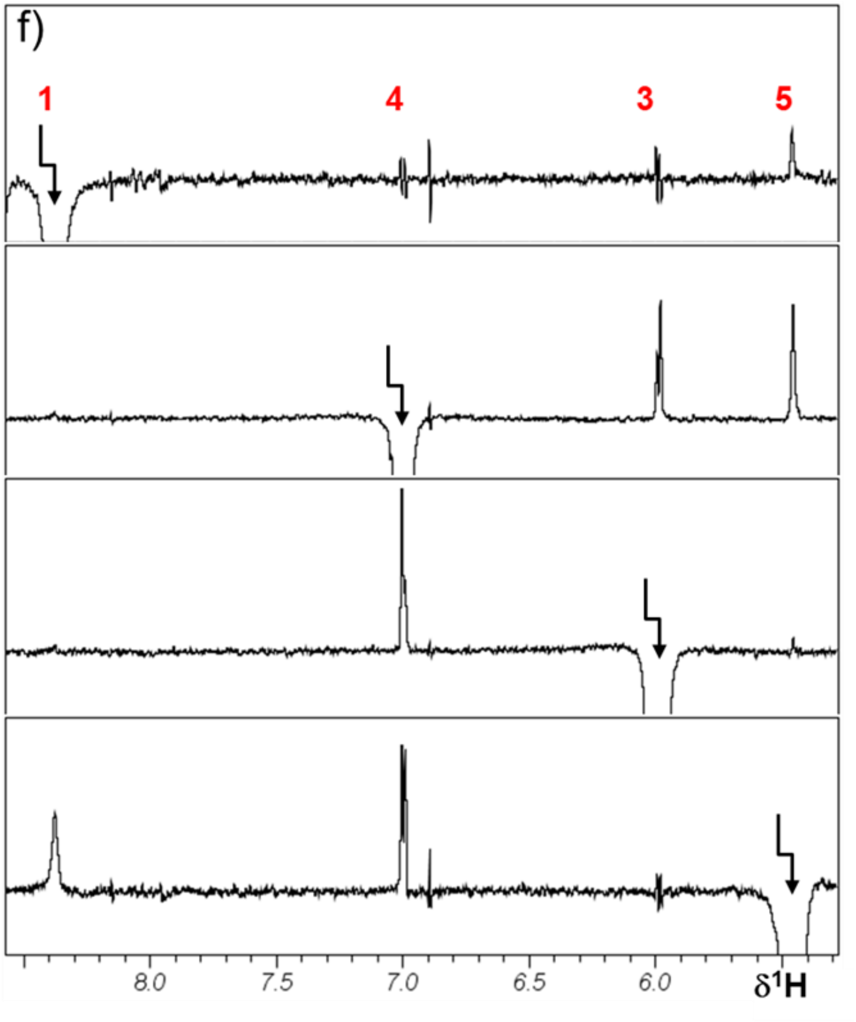

Figure S14. NMR data of ozonated pyrrole sample prepared by the work-up (1) (Text S7) recorded in DMSO-d_6: (a-1 and a-2) ^{1}H with chemical structures of TP2 and maleimide, (b-1 and b-2) ^{13}C, (c) ^{1}H-^{13}C HSQC, (d) ^{1}H-^{13}C HMBC, (e) ^{1}H-^{1}H DQF-COSY, and (f) 1D-NOESY with arrows indicating the selectively excited resonances. ^{1}H and ^{13}C NMR spectra of the full spectral regions (a-1 and b-1) and of the regions of interest (a-2 and b-2) are shown. The numbers assigned across the NMR spectra correspond to the positions of the structures of TP2 (in red) and maleimide (in black).

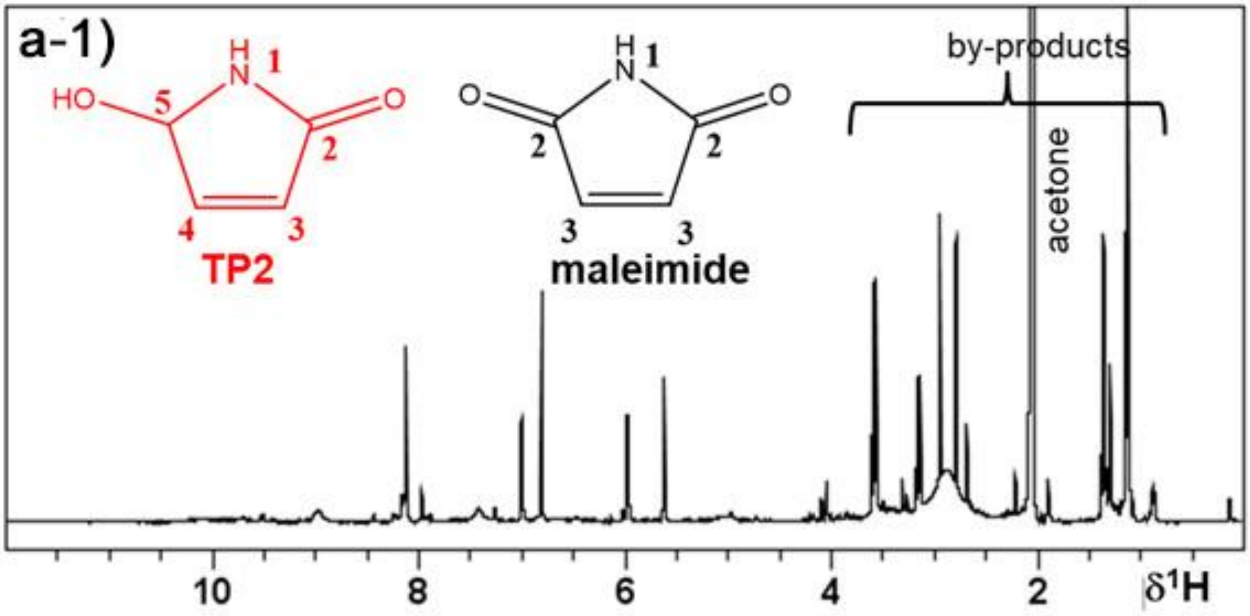
a-1)
HO
H
N
1
5
O
2
4
3
TP2
H
N
1
O
O
2
2
3
3
maleimide
by-products
acetone
10
8
6
4
2
δ¹H

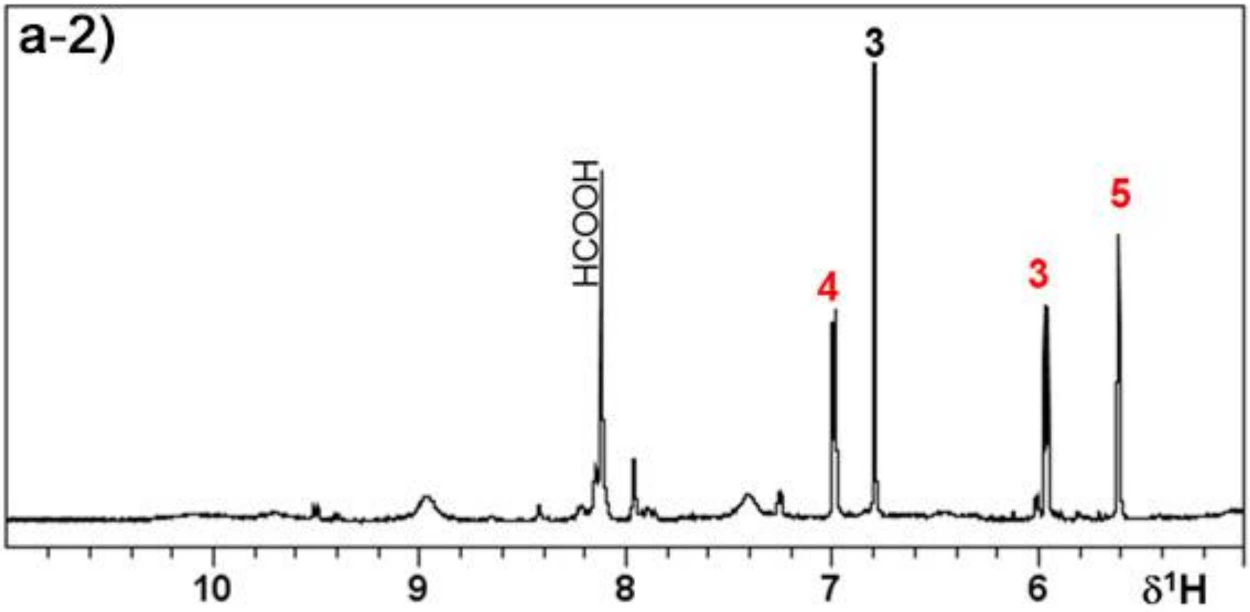
a-2)
HCOOH
3
4
3
5
10
9
8
7
6
δ¹H

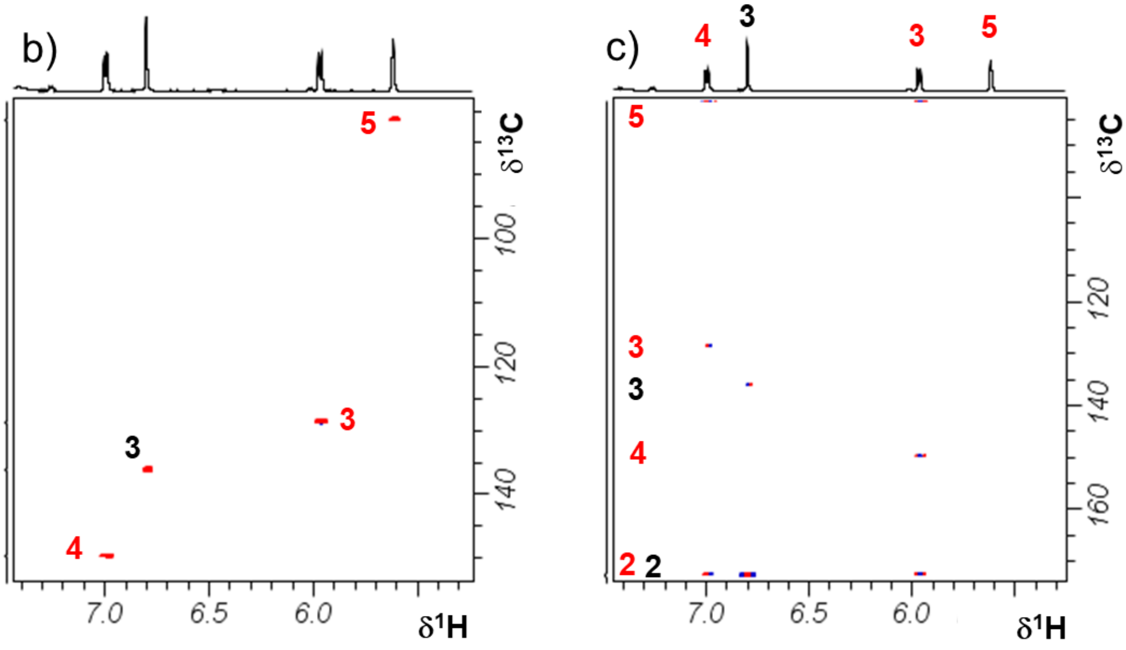

Figure S15. NMR data of ozonated pyrrole sample prepared by the work-up (1) (Text S7) recorded in acetone-d_6: (a-1 and a-2) ^{1}H with chemical structures of TP2 and maleimide, (b) ^{1}H-^{13}C HSQC, and (c) ^{1}H-^{13}C HMBC. ^{1}H NMR spectra of the full spectral region (a-1) and of the region of interest (a-2) are shown. The numbers assigned across the NMR spectra correspond to the positions of the structures of TP2 (in red) and maleimide (in black).

2) *NMR identification of maleimide isolated by the work-up (1)*. The singlet signal observed at 6.87 ppm in the ^{1}H NMR spectrum shows a direct attachment to carbon at 135.2 ppm, in the olefinic region of chemical shifts (Figure S14c). It also shows long-range correlations to carbons at 172.7 ppm (Figure S14d) as well as a weak correlation to 135.2 ppm (correlation to "itself") (Figure S14d). Therefore, we concluded that this chemical species must be symmetrical and maleimide was suggested as a potential candidate. The ^{1}H and ^{13}C NMR data of a commercially available reference standard of maleimide recorded in DMSO-d_6 solution (Figure S16 and Table S9) show resonances at exactly the same positions as obtained from the isolated species, unambiguously confirming the presence of maleimide in the NMR sample of the ozonated pyrrole solution.

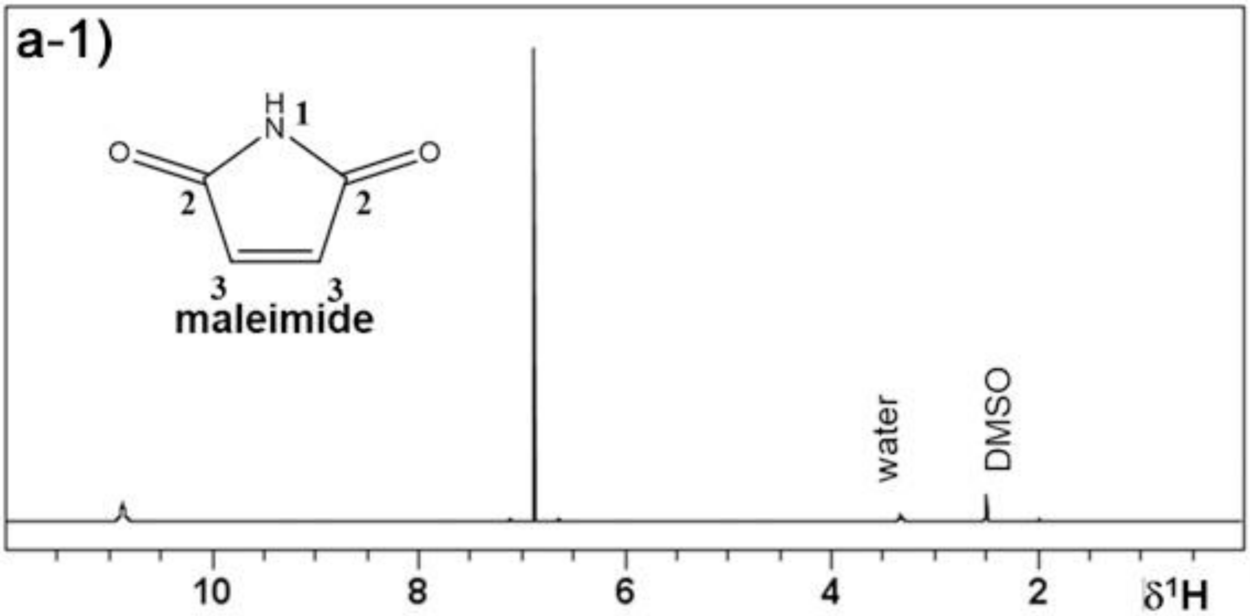
a-1)
H
N
1
O
O
2
2
3
3
maleimide
water
DMSO
10
8
6
4
2
δ1H

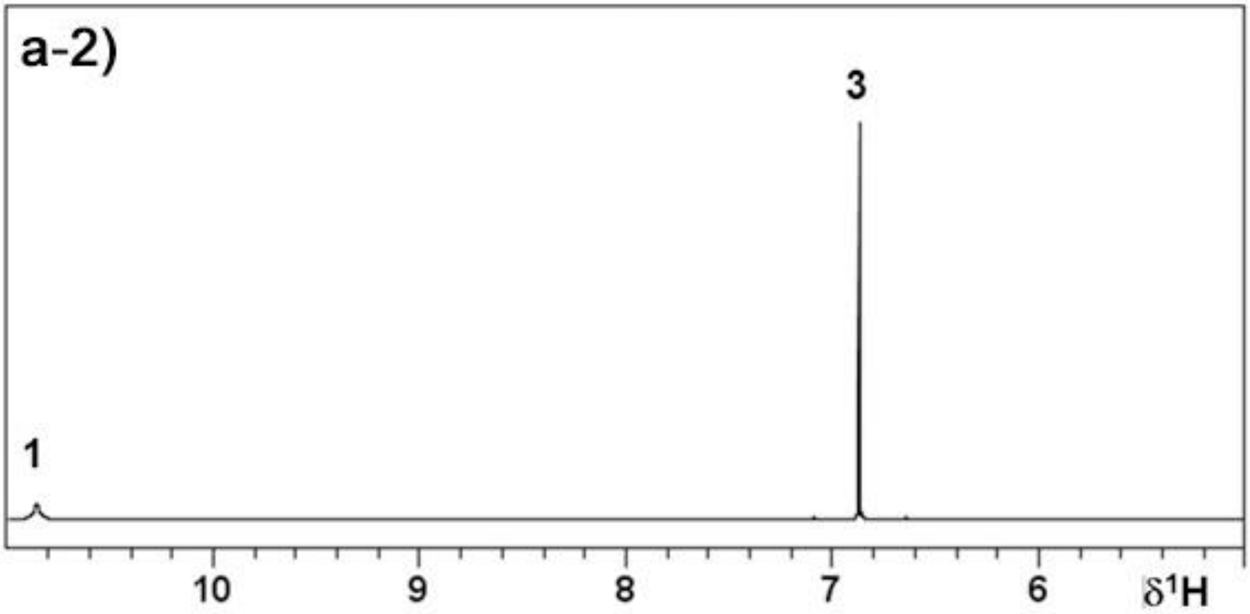
a-2)
3
1
10
9
8
7
6
δ1H

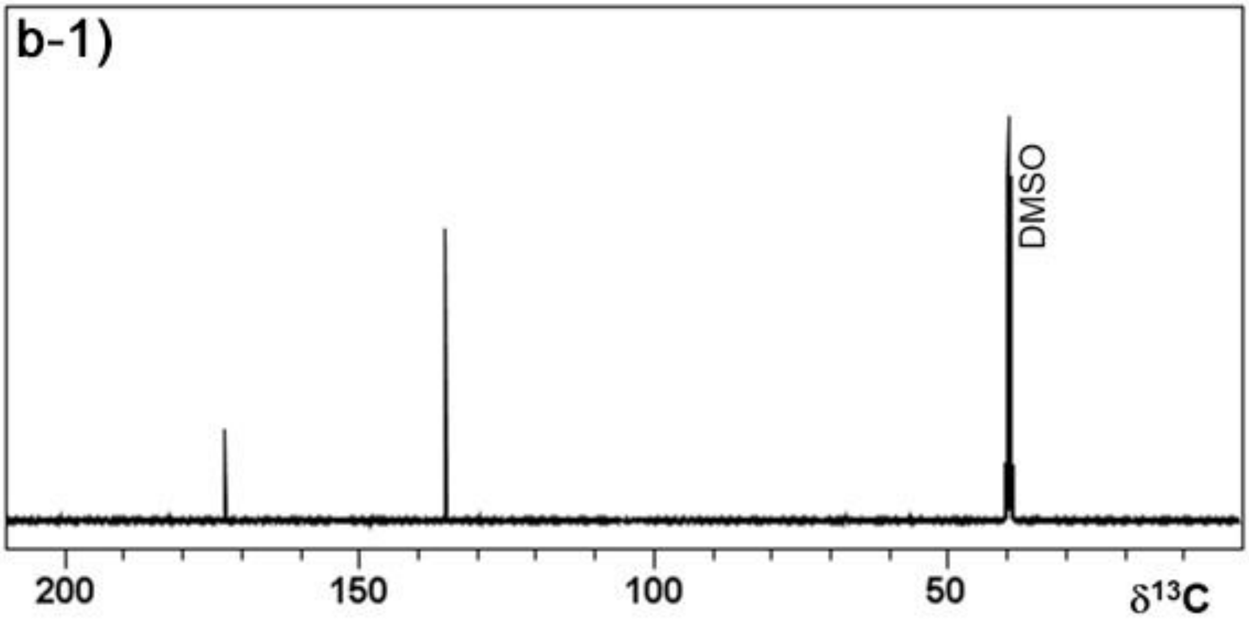
b-1)
DMSO
200
150
100
50
δ13C

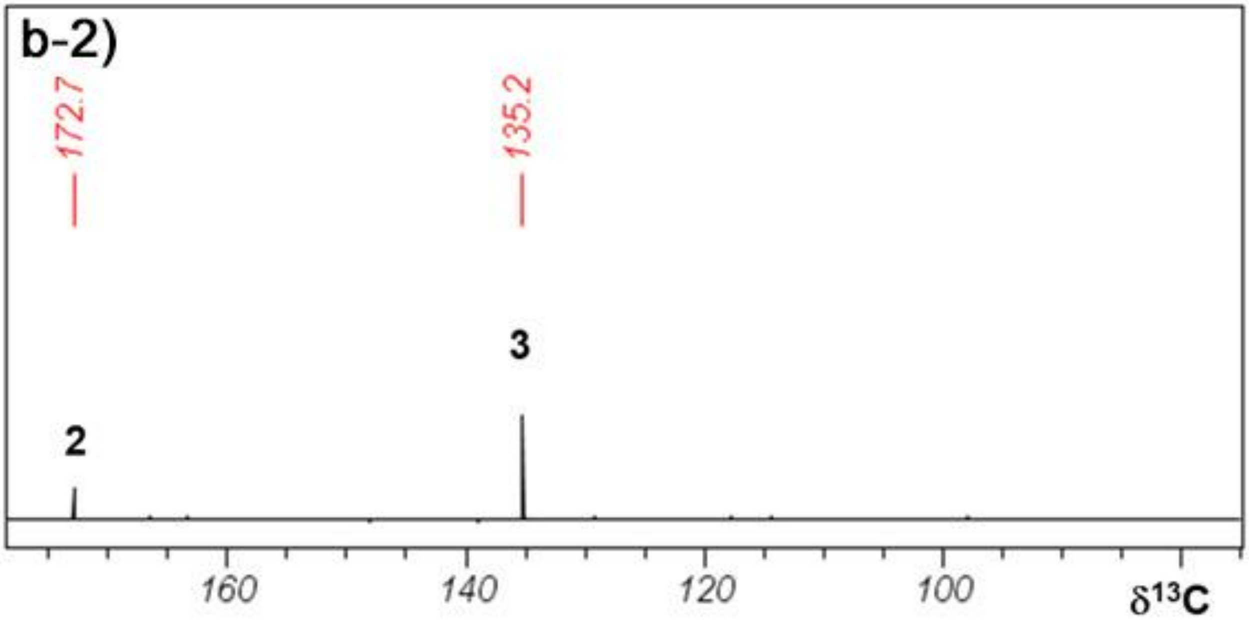
b-2)
172.7
135.2
3
2
160
140
120
100
δ13C

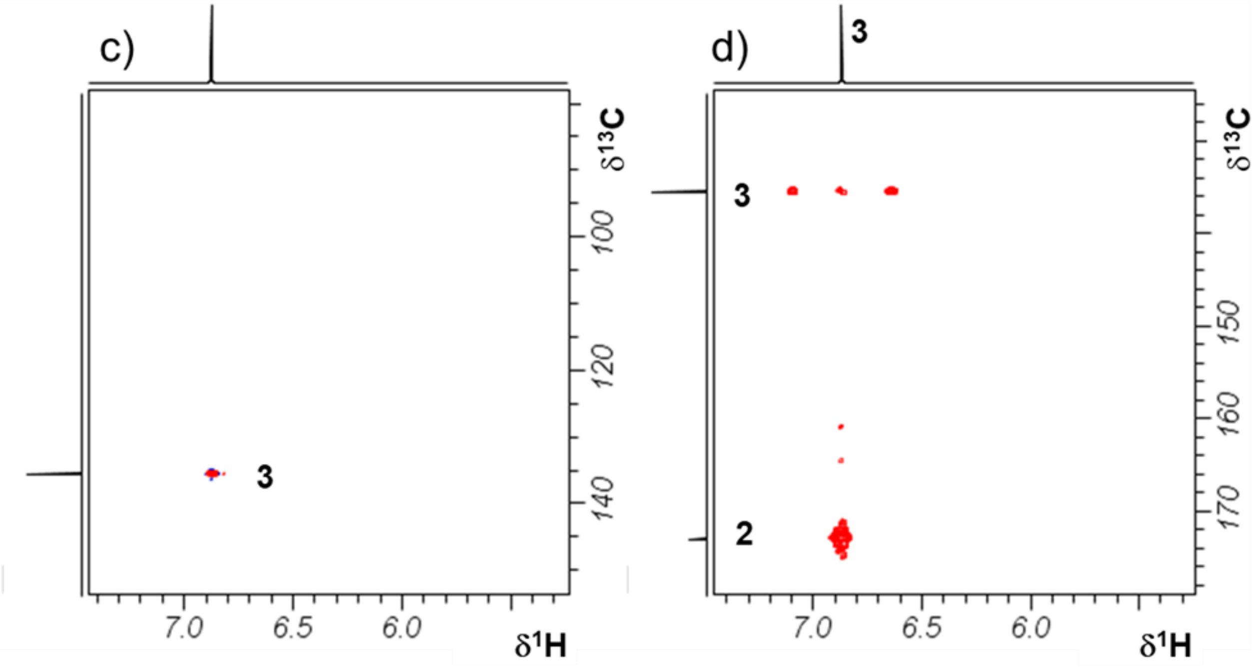

Figure S16. NMR data of a commercially available reference standard of maleimide recorded in DMSO-d_6: (a-1 and a-2) ^{1}H with chemical structure of maleimide, (b-1 and b-2) ^{13}C, (c) ^{1}H-^{13}C HSQC, and (d) ^{1}H-^{13}C HMBC. ^{1}H and ^{13}C NMR spectra of the full spectral regions (a-1 and b-1) and of the regions of interest (a-2 and b-2) are shown. The numbers assigned across the NMR spectra correspond to the positions of the structures of maleimide.

3) *NMR identification of TP2, TP1_a, and TP1_b isolated by the work-up (2)*. The presence of TP2 in the isolate prepared by the work-up (2) was confirmed by the ^{1}H and ^{13}C NMR chemical shifts and 2D NMR correlation signals (Figure S17) based on the assignments as discussed above in "*1) NMR identification of TP2 isolated by the work-up (1)*". Unlike the isolate prepared by work-up (1), the isolate prepared by the work-up (2) did not seem to contain much maleimide. The low intensity signal at 6.9 ppm (singlet) in the ^{1}H NMR spectrum can be attributed to traces of maleimide (resonance assignments not shown in Figure S17). In addition to TP2 and traces of maleimide, resonances of two additional chemical species were found. The ^{1}H-^{13}C HSQC experiment resulted in prominent correlations between 9.48 ppm and 192.9 ppm and between 9.38 ppm and 191.6 ppm, respectively (Figure S17c-1 and Table S9), indicating the presence of aldehyde groups. Furthermore, formamide-type correlations were found between protons and carbons at 8.40 ppm and 160.7 ppm and between 8.64 ppm and 164.9 ppm, respectively (Figure S17c-2 and Table S9). As a result of the ^{1}H-^{1}H DQF-COSY experiment (Figure S17e) and ^{1}H-^{13}C long-range correlations (Figure S17d), the chemical structure of TP1 (with no specific stereochemistry yet) was presumed with the skeleton structure of C(=O)H-NH-CH=CH-C(=O)H. For small molecules, typically the opposite sign is expected for 2D NOESY interactions with respect to the diagonal peaks: e.g., the cross signal of H-3 to H-4 of TP2 in Figure S17f. However, all other observable 2D NOESY NMR cross peaks have the same sign as the diagonal peaks (Figure S17f), wherefore, a chemical exchange process between two stereoisomers must be postulated. For the isomers TP1_a and TP1_b, *J*(H-1, H-2) of 14.2 Hz and 13.7 Hz were determined, respectively (Table S9). Therefore, H-1 and H-2 must be in *trans* configuration to each other at the double bond. For both isomers, *J*(H-2, H-3) of 8.0 Hz was found. This indicates a *trans* configuration of H-2 and H-3. Because of the presence of the aldehyde group, the coupling constants between H-2 and H-4 are considerably smaller than *J*(H-1, H-2). Finally, *J*(H-4, NH) = 8.7 Hz for TP1_b proved that H-4 and NH of the TP1_b must be *trans* to each other. In contrast, for TP1_a, *J*(H-4, NH) was small and not resolved, indicating *cis* configuration of H-4 and NH. Such isomer specific *J* values can be found in literature, e.g., for formamide as reference compound.[30]

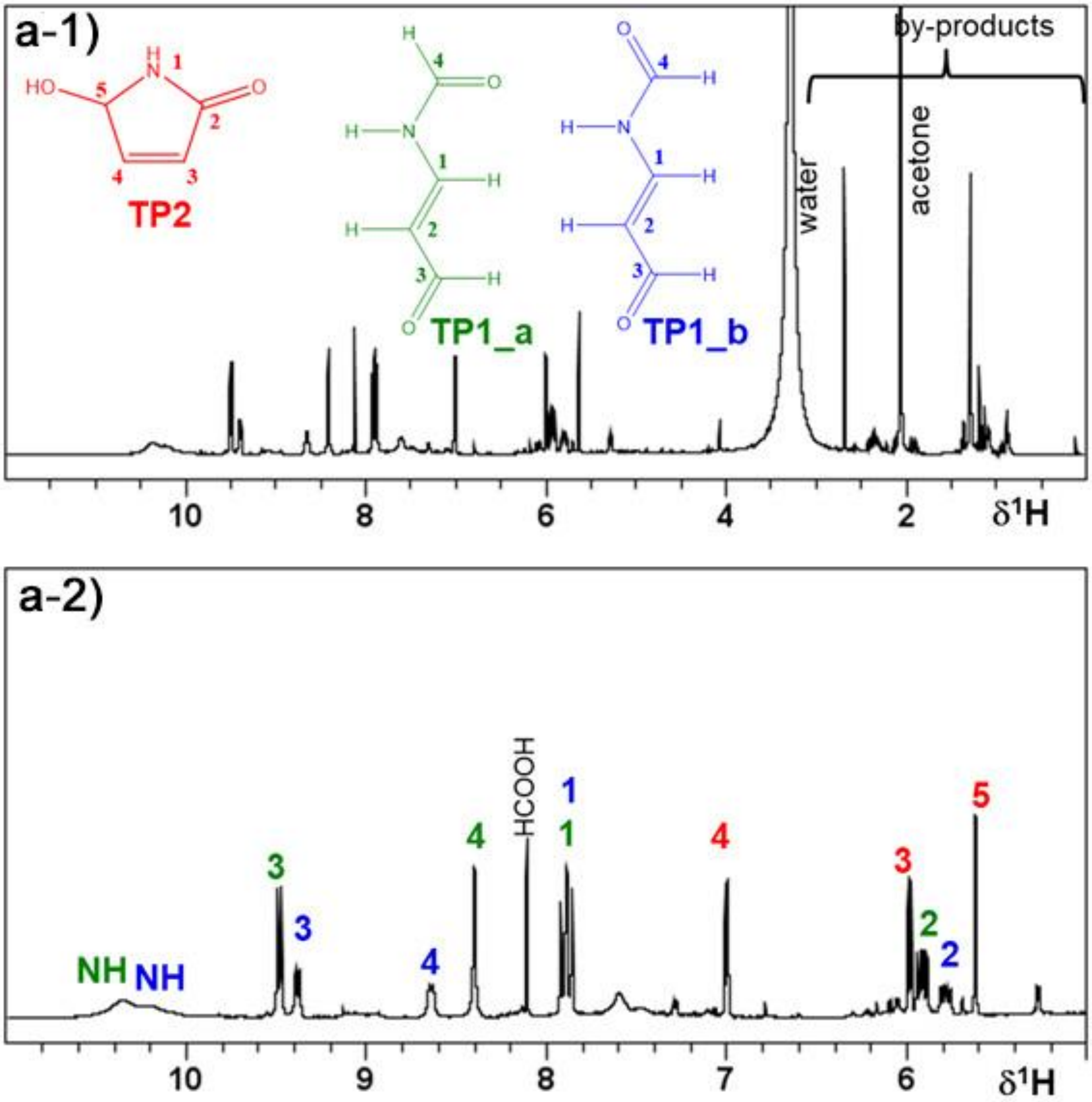
a-1)
TP2
TP1_a
TP1_b
HO
H
N
O
1
2
3
4
5
by-products
water
acetone
10
8
6
4
2
δ¹H
a-2)
NH
NH
3
3
4
4
HCOOH
1
1
4
3
2
2
5
10
9
8
7
6
δ¹H

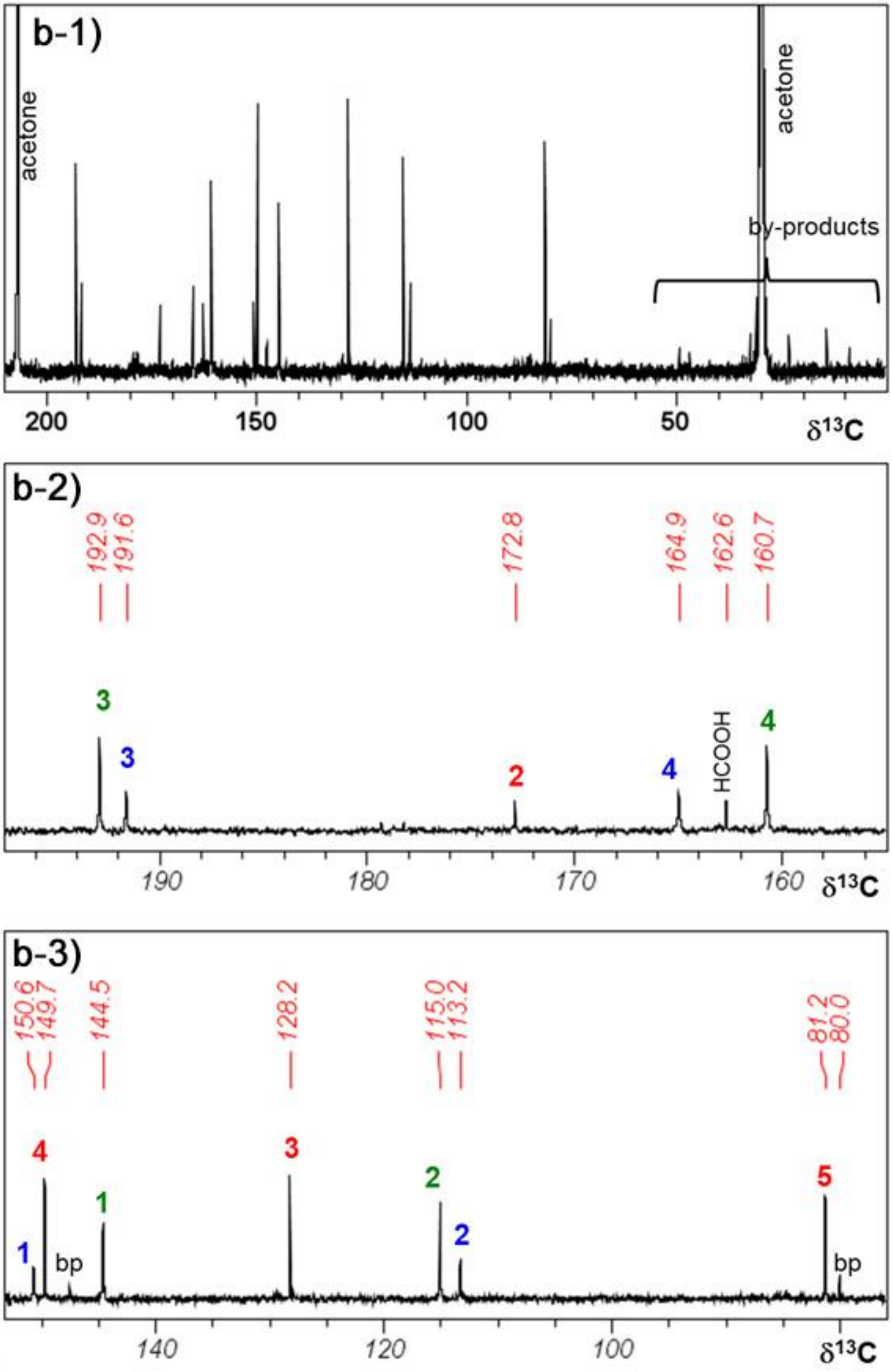

b-1)
acetone
acetone
by-products
200
150
100
50
δ13C
b-2)
192.9
191.6
172.8
164.9
162.6
160.7
3
3
2
4
HCOOH
4
190
180
170
160
δ13C
b-3)
150.6
149.7
144.5
128.2
115.0
113.2
81.2
80.0
1
4
bp
1
3
2
2
5
bp
140
120
100
δ13C

c-1)

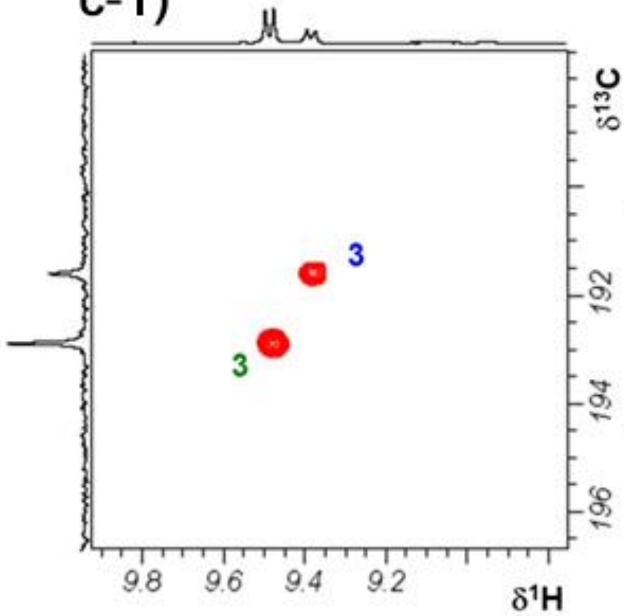
3
3
δ13C
192
194
196
9.8
9.6
9.4
9.2
δ1H

c-2)

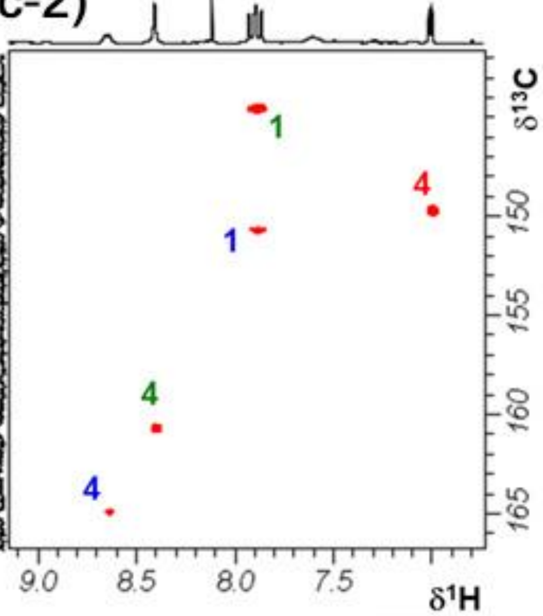
1
4
1
4
4
δ13C
150
155
160
165
9.0
8.5
8.0
7.5
δ1H

c-3)

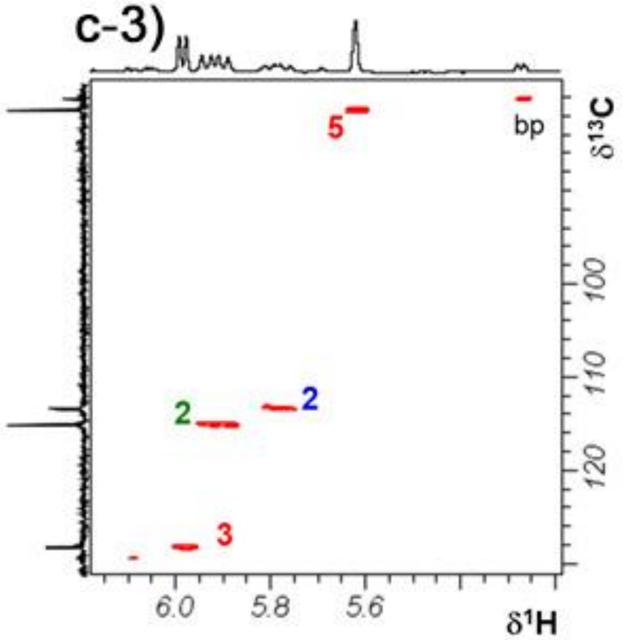
5
bp
δ13C
100
110
120
2
2
3
6.0
5.8
5.6
δ1H

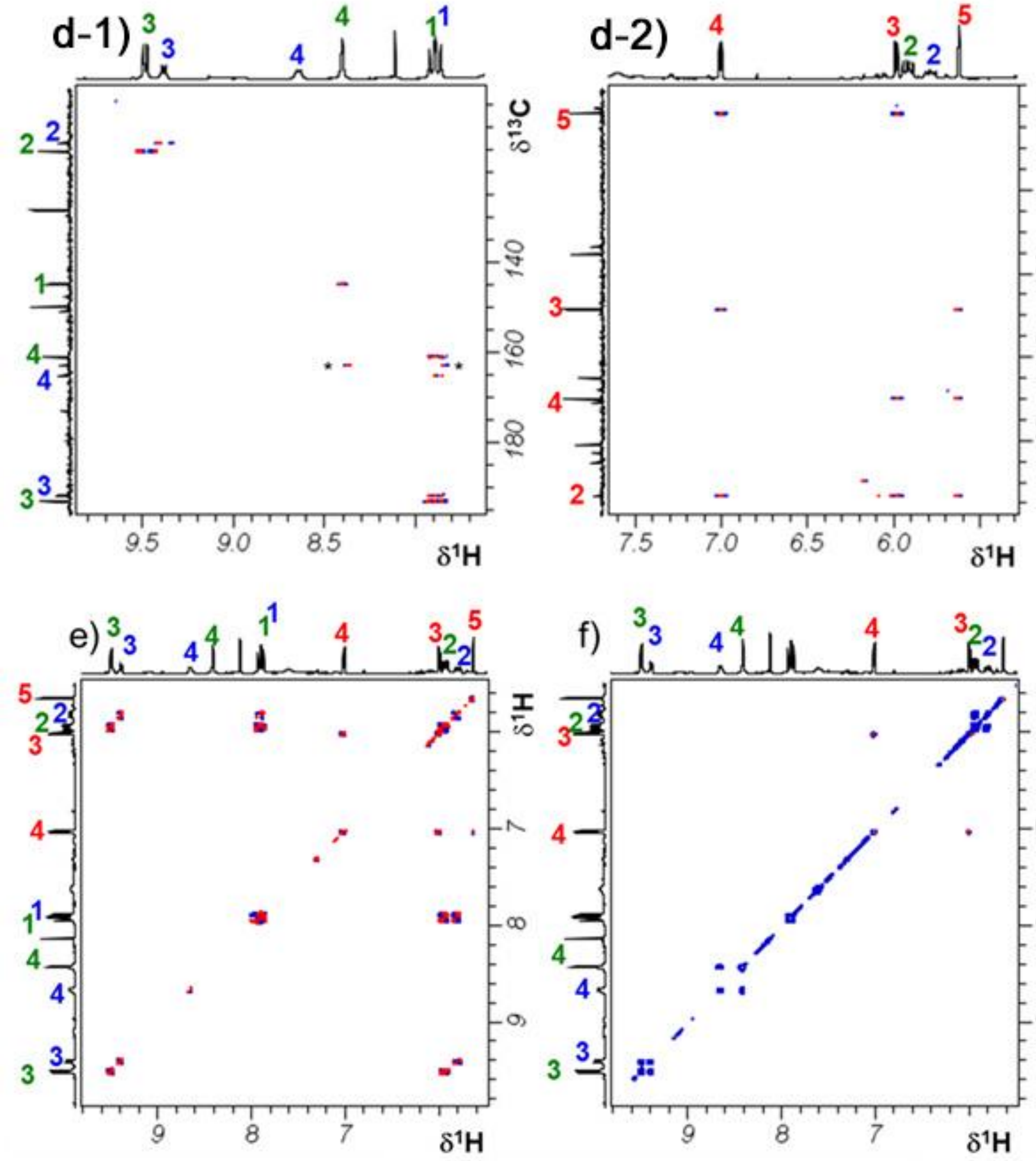

Figure S17. NMR data of an ozonated pyrrole sample prepared by the work-up (2) (Text S7) recorded in acetone-d_6: (a-1 and a-2) ^{1}H with chemical structures of TP2, TP1_a and TP1_b, (b-1, b-2, and b-3) ^{13}C, (c-1, c-2, and c-3) ^{1}H-^{13}C HSQC, (d-1 and d-2) ^{1}H-^{13}C HMBC, (e) ^{1}H-^{1}H DQF-COSY, and (f) ^{1}H-^{1}H NOESY. ^{1}H and ^{13}C NMR spectra of the full spectral regions (a-1 and b-1) and of the regions of interest (a-2, b-2, and b-3) are shown. The numbers assigned across the NMR spectra correspond to the positions of the structures of TP2 (in red), TP1_a (in green), and TP1_b (in blue).

Text S8. NMR results – ^{1}H signal integration for TP1, TP2, and maleimide

The relative amounts of TP1, TP2, and maleimide in the NMR samples can be determined by integrating substance-specific ^{1}H NMR resonances. However, the isolated solids from the ozonated pyrrole solution were only partially soluble in acetone-d$_6$, making a reproducible estimate of the isolated products impossible. Moreover, the ^{1}H NMR signal intensities varied significantly depending on the applied work-up procedures for removal of water after ozonation (Text S4). Specifically, the ratio of the integrated peak areas of TP2:TP1:maleimide was 1:0.1:0.5 for the sample isolated by work-up (1) treated by rotary evaporation with an elevated temperature (Table S10), whereas the ratio was 1:1.8:0.02 for the sample isolated by work-up (2) treated by rotary evaporation and lyophilization (Table S11). The isolated solids were almost completely soluble in DMSO-d$_6$ but with the disadvantage that broad background resonances of polymerized material made reliable integration of the signals of interest difficult. Therefore, a different sample composition of 1:0.08:0.3 for TP2:TP1:maleimide was obtained compared to those in acetone d$_6$ solutions (Table S10 and Table S12).

Table S10. Peak integration of ^{1}H NMR spectra recorded in acetone-d$_6$ for TP1, TP2, and maleimide detected in the ozonated pyrrole sample treated by the work-up (1) (only rotary evaporation to dryness).

Compound	**δ^{1}H**	**No. of H**	**Peak integration**	**Peak integration per H**
TP2	7.0/6.0/5.4	3	3.000	1.000
TP1_a	9.5	1	0.076	0.076
TP1_b	9.4	1	0.032	0.032
Maleimide	6.8	2	0.948	0.474

Table S11. Peak integration of ^{1}H NMR spectra recorded in acetone-d$_6$ for TP1, TP2, and maleimide detected in the ozonated pyrrole sample treated by work-up (2) (rotary evaporation followed by lyophilization).

Compound	**δ^{1}H**	**No. of H**	**Peak integration**	**Peak integration per H**
TP2	7.0/6.0/5.4	3	3.004	1.001
TP1_a	9.5/8.4/5.9	3	3.518	1.173
TP1_b	9.4/8.7/5.7	3	1.846	0.615
Maleimide	6.8	2	0.041	0.021

Table S12. Peak integration of ^{1}H NMR spectra recorded in DMSO-d$_6$ for TP1, TP2, and maleimide detected in the ozonated pyrrole sample treated by the work-up (1) (only rotary evaporation to dryness).

Compound	**δ^{1}H**	**No. of H**	**Peak integration**	**Peak integration per H**
TP2	7.0/6.0/5.4	3	2.976	0.992
TP1_a	9.4	1	0.045	0.045
TP1_b	9.3	1	0.038	0.038
Maleimide	6.9	2	0.506	0.253

Text S9. LC-HRMS/MS results – detection of $C_4H_5NO_2$ and C_4H_5NO upon ozonation of pyrrole.

This section presents LC-HRMS/MS chromatograms, MS2 spectra, and integrated LC-MS peak areas as a function of the molar ratio of $[O_3]/[\text{Pyrrole}]_0$ for $C_4H_5NO_2$ and C_4H_5NO formed during the reaction of pyrrole with ozone.

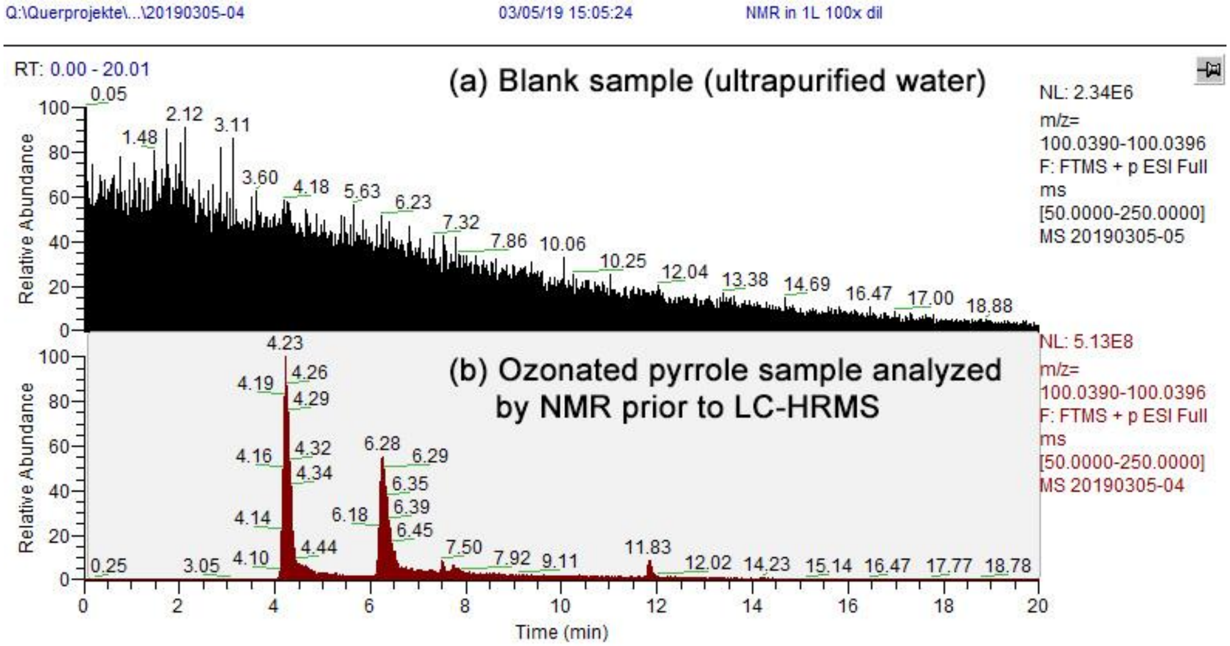

Figure S18. LC-HRMS/MS total ion chromatogram filtered by 100.0393, the exact mass of $C_4H_5NO_2$ as $[M+H]^+$ for (a) a blank sample with ultrapurified water and (b) a sample containing pyrrole ozonated and analyzed by NMR.

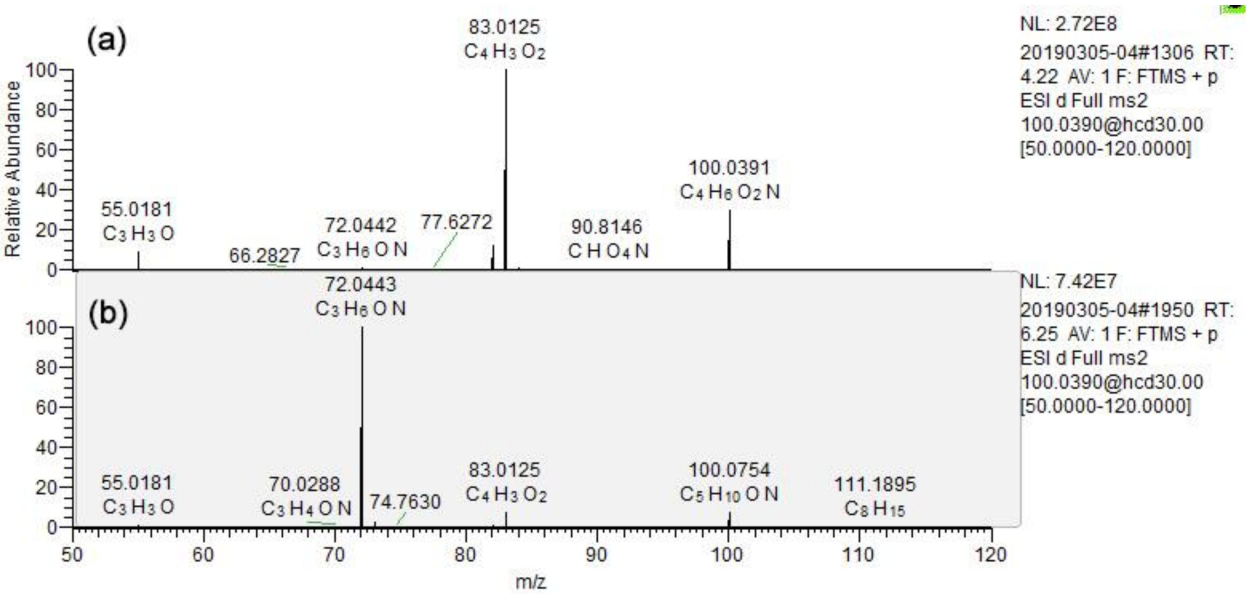

Figure S19. MS2 fragmentation patterns for the peaks at retention times of (a) 4.2 min and (b) 6.3 min for m/z = 100.0393 as shown in Figure S18.

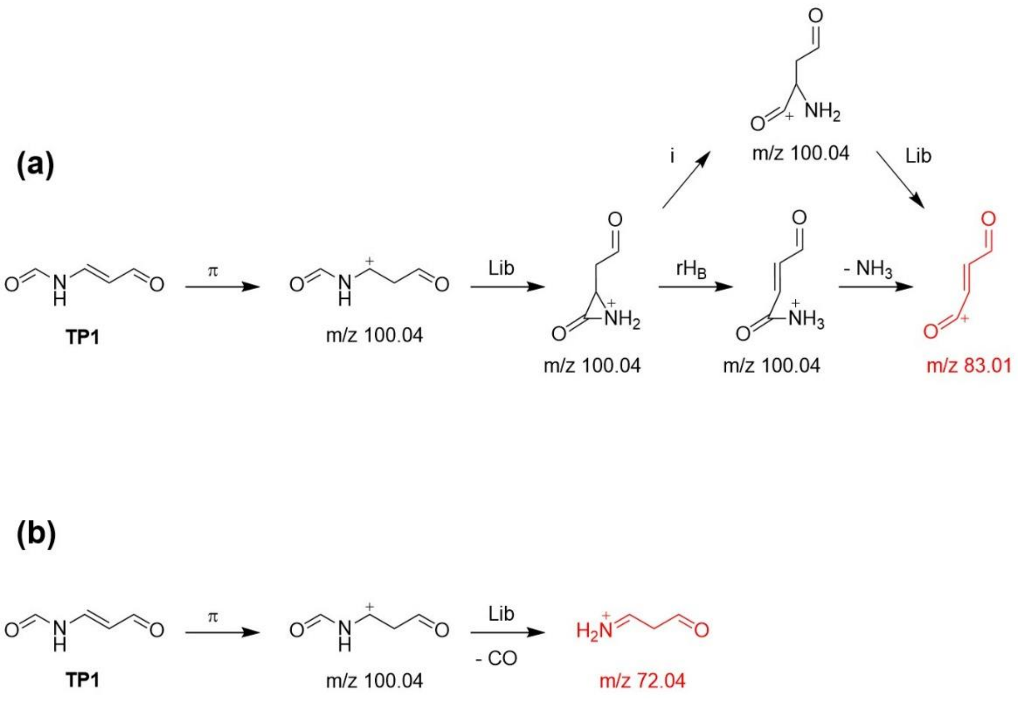

Figure S20. Fragmentation pathways predicted by a mass spectra interpretation software (Mass Frontier™, Thermo Scientific) from TP1 (a) to a fragment ion of m/z = 83.0125 and (b) to a fragment ion of m/z = 72.0443. Only selected patterns with the shortest pathway are shown. The codes used to describe the pathways are π: pi-electron ionization, Lib: fragmentation library mechanism, rH_B: charge site rearrangement (γ), i: inductive cleavage.

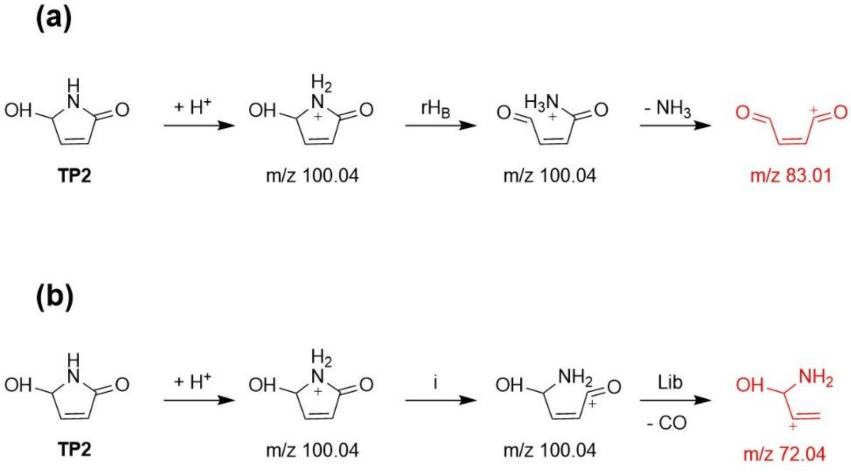

Figure S21. Fragmentation pathways predicted by a mass spectra interpretation software (Mass Frontier™, Thermo Scientific) from TP2 (a) to a fragment ion of m/z = 83.0125 and (b) to a fragment ion of m/z = 72.0443. Only selected patterns with the shortest pathway are shown. The codes used to describe the pathways are +H$^+$: protonation, i: inductive cleavage, Lib: fragmentation library mechanism, rH$_B$: charge site rearrangement (γ).

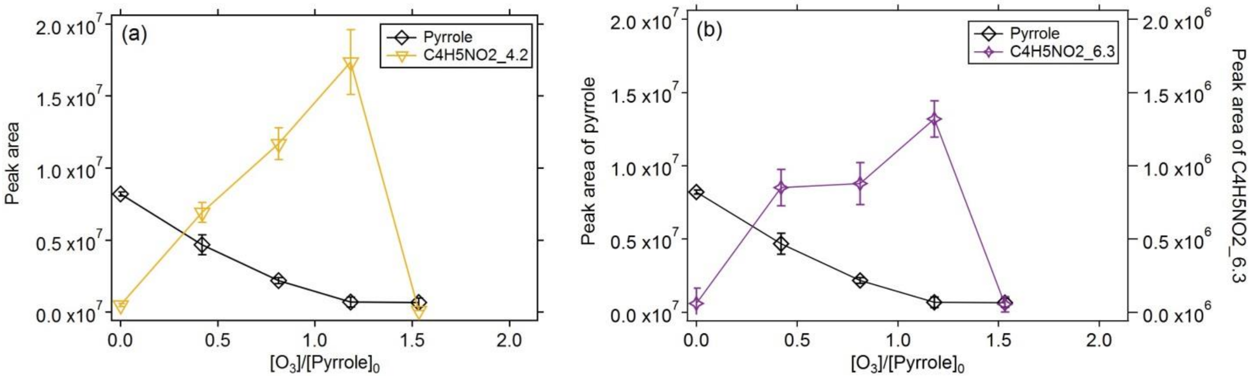

Figure S22. Integrated peak areas of (a and b) pyrrole, (a) $C_4H_5NO_2$_4.2, and (b) $C_4H_5NO_2$_6.3 as a function of the molar ratio of $[O_3]/[\mathrm{Pyrrole}]_0$. $C_4H_5NO_2$_4.2 and $C_4H_5NO_2$_6.3 are peaks with m/z = 100.0393 (as $[M+H]^+$) as shown in Figure S18. All measurements were carried out in presence of 50 mM *t*-butanol at pH 7 (10 mM phosphate buffer). The initial pyrrole concentration was around 110 µM.

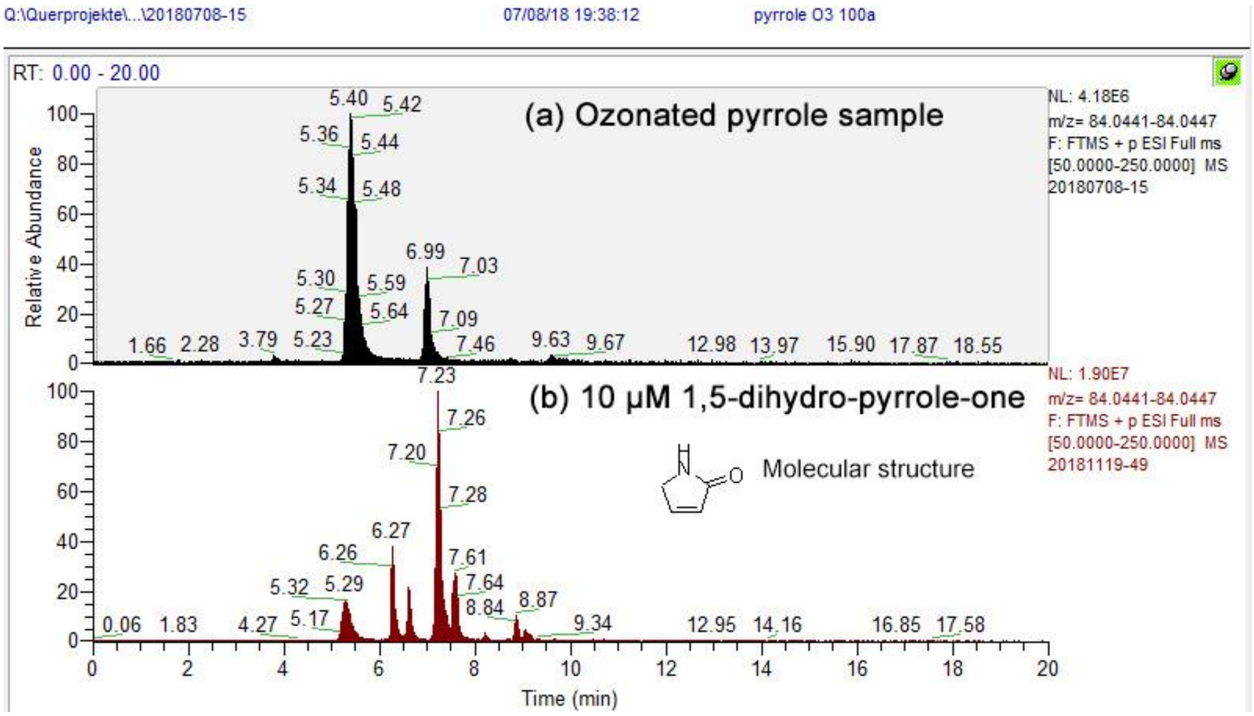

Figure S23. LC-HRMS/MS total ion chromatogram filtered by m/z = 84.0444, the exact mass of C_4H_5NO as $[M+H]^+$ (Δmass = 3 ppm) for an ozonated sample with (a) a molar $[O_3]/[Pyrrole]_0$ ratio of ~ 1 and (b) for 10 µM of 1,5-dihydro-pyrrole-one.

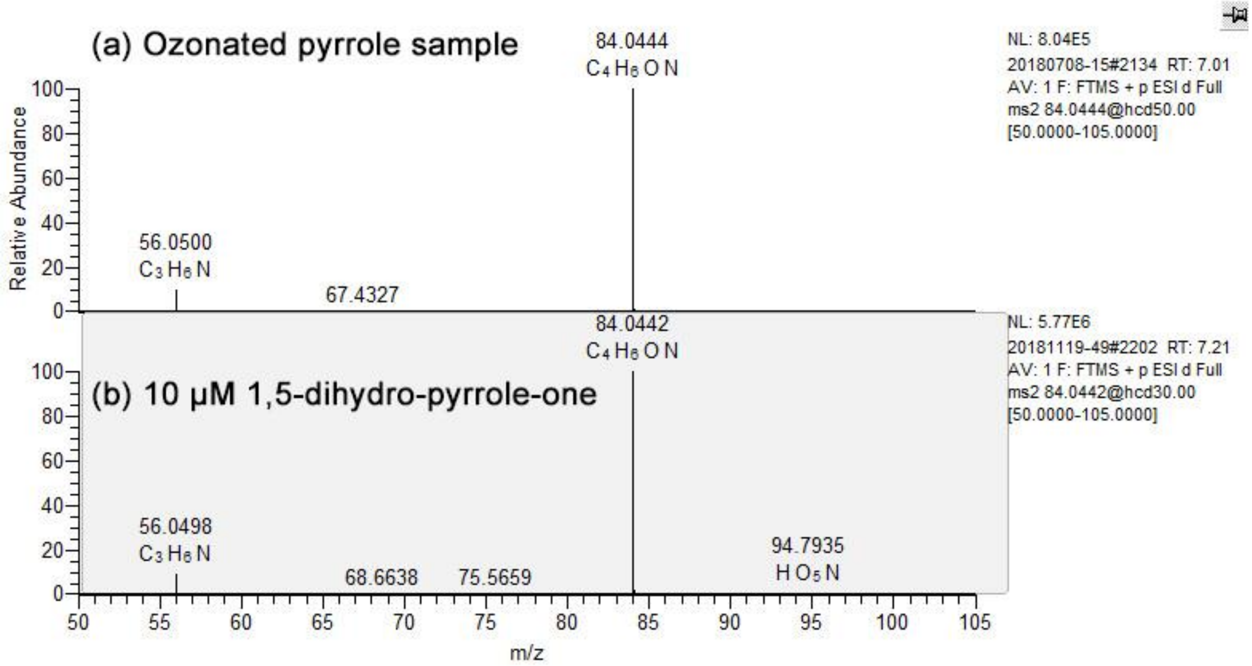

Figure S24. MS2 fragmentation patterns for the peaks (a) at a retention time of 7.0 min for an ozonated sample with a molar $[O_3]/[Pyrrole]_0$ ratio of ~ 1 and (b) at a retention time of 7.2 min for 10 µM 1,5-dihydro-pyrrole-one, as shown in Figure S23.

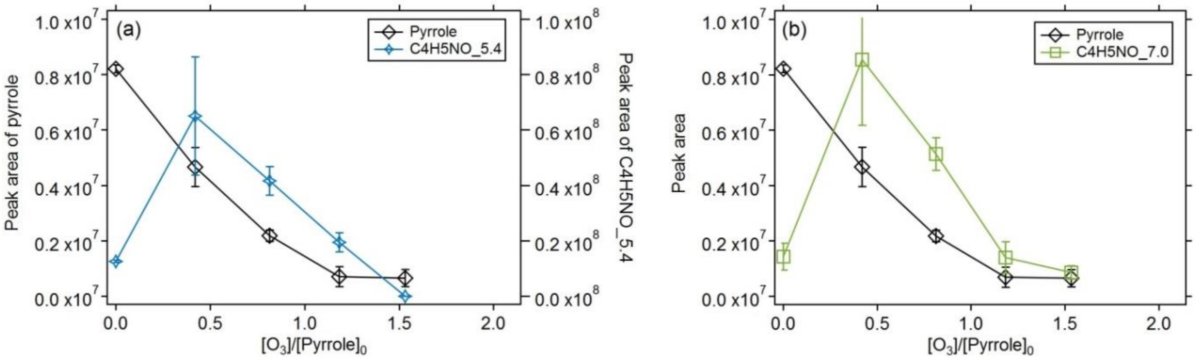

Figure S25. Integrated peak areas of (a and b) pyrrole, (a) C_4H_5NO_5.4, and (b) C_4H_5NO_7.0 as a function of the molar ratio of $[O_3]/[Pyrrole]_0$. C_4H_5NO_5.4 and C_4H_5NO_7.0 are unknown peaks with m/z = 84.0444 (as $[M+H]^+$) as shown in Figure S23. All measurements were carried out in presence of 50 mM *t*-butanol at pH 7 (10 mM phosphate buffer). The initial pyrrole concentration was around 110 µM.

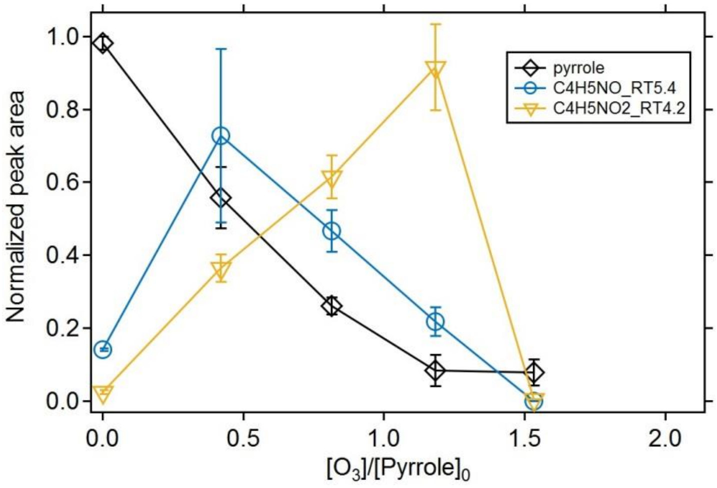

Figure S26. Integrated peak areas of pyrrole, C_4H_5NO_5.4, and $C_4H_5NO_2$_4.2 as a function of the molar ratio of $[O_3]/[Pyrrole]_0$. The areas were normalized by the largest area detected for each compound. C_4H_5NO_5.4, and $C_4H_5NO_2$_4.2 are the same as shown in Figure S25 and Figure S22, respectively. All measurements were carried out in presence of 50 mM *t*-butanol at pH 7 (10 mM phosphate buffer). The initial pyrrole concentration was around 110 µM.

Text S10. Quantum chemical computation results: initial pathways (A – C) of the pyrrole-ozone reaction

Based on the methods described in Text S6, the proposed reaction mechanisms of the pyrrole-ozone reaction were further investigated by quantum chemical computations. For the initial attack of ozone on pyrrole, different mechanisms are imaginable (Figure 3 in the main text and Figure S27). Following the formation of a pre-reactive complex, ozone could undergo concerted, bidentate cycloadditions at C2 and C3, or at C2 and C5. The other possibility is a monodentate addition at position C2. Transition structures for the monodentate attack were found using restricted as well as unrestricted calculations. We searched for transition structures for the bidentate attack by first optimizing the system keeping the C2-O and C3-O (or C2-O and C5-O) distances fixed at the same value (different values were tried), and optimizing the rest of the system. Starting from these partially optimized structures, a conventional transition structure optimization was performed. Neither for restricted nor for unrestricted (preceded by a wavefunction stability analysis) calculations were we able to obtain a transition structure for a concerted cycloaddition. Instead, the optimizations yielded transition structures for monodentate additions.

We note that the LC-ωPBE density functional was chosen as it performed best in reproducing gas phase barrier heights for ozone reactions with different substrates, including bidentate cycloaddition to ethane/ethyne, and monodentate attack on trimethylamine and bromide.[28] This suggests that if a bidentate cycloaddition to pyrrole in implicit water solvation is possible, LC-ωPBE should have been the most suitable density functional to find such transition structures. In contrast, a polar solvent can be expected to somewhat favor ionic reaction mechanisms, such as the monodentate attack that yields a zwitterion as an unstable intermediate. Lastly, as ozone is considered a multireference system, results obtained with single-reference methods have to be interpreted with caution, and the possibility of a bidentate attack cannot be entirely ruled out.

If a bidentate attack was possible, we would expect the barrier for formation of the C2,C5-cycloadduct to be higher than that for the formation of the C2,C3-cycloadduct. We reason that the strain in the C2,C5-cycloadduct that is responsible for its inferior stability compared to the C2,C3-cycloadduct is also partly present in the transition structure, and will destabilize the latter. We thus think that the formation of the C2,C5-cycloadduct is rather unlikely (see also Text S12).

The zwitterion that results from monodentate attack can exist in at least two stable conformations, which are separated by a low energetic barrier. Despite failing IRC calculations, the imaginary frequency of the transition structure is clearly associated with the torsion that would interconvert these conformers. From these, the C2,C3-cycloadduct can be reached also by a low barrier, whereas the C2,C5-cycloadduct can be reached only passing a higher barrier.

It is discussed in Text S11 to Text S15 that pathways (A) and (C) (including the subsequent pathways (D – G)) could be competitive, at least within the margin of error of the simulations, whereas pathway (B) is predicted to be rather unlikely.

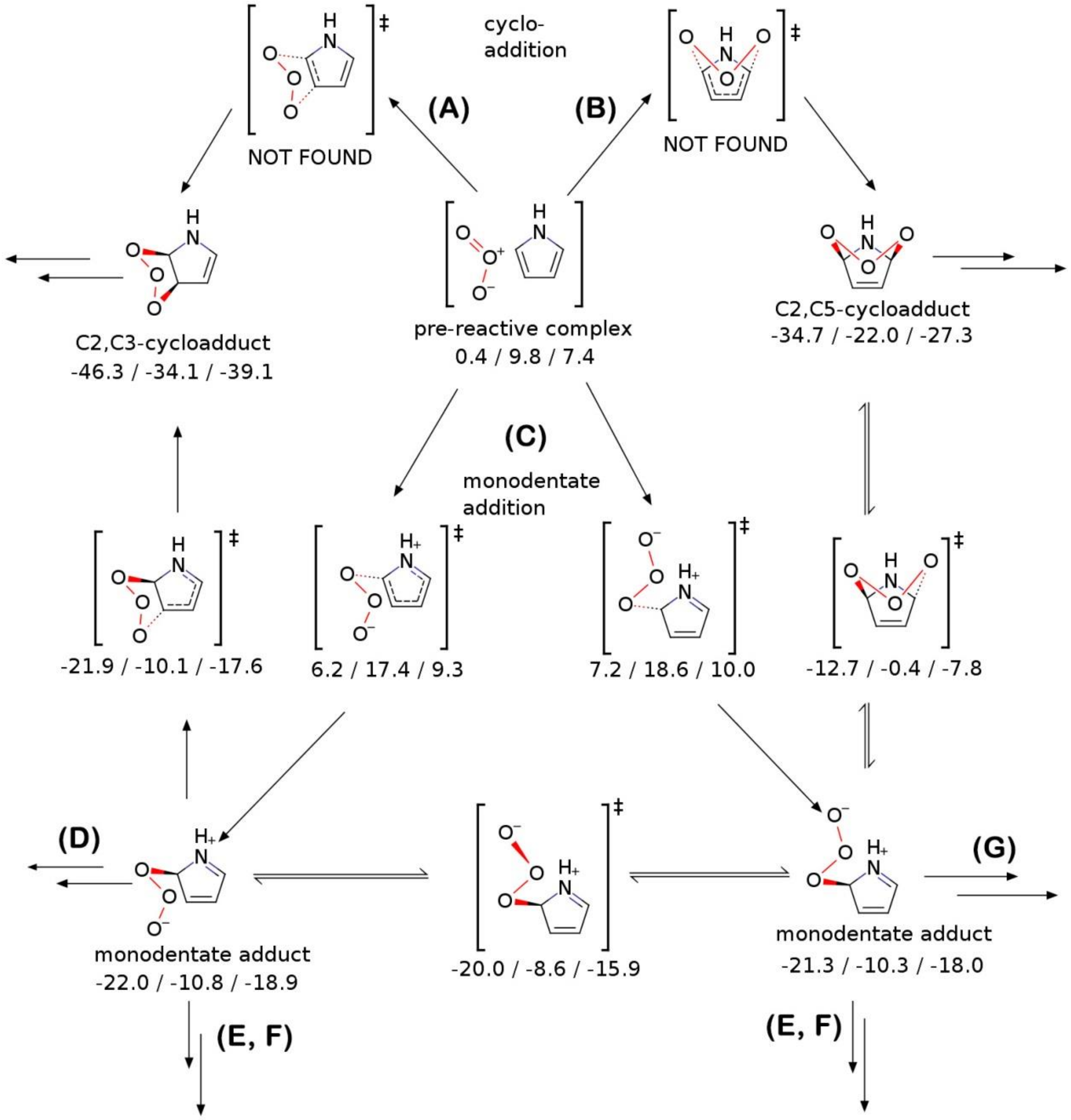

Figure S27. Computational depiction of the initial pathways (A – C) of the pyrrole-ozone reactions. The three numbers below each reaction species indicate LC-ωPBE energies at 0 K including zero-point vibrational energies, LC-ωPBE Gibbs free energies at 298 K, and M06-2X Gibbs free energies at 298 K (from left to right).

Text S11. Quantum chemical computation results: pathway (A) of the pyrrole-ozone reaction

Figure S28 shows how the double bond can be cleaved from the C2,C3-cycloadduct, leading eventually to the observed product TP1 and H_2O_2 in an exothermic/exergonic reaction. However, in the Gibbs free energy picture, the barrier for breaking the remaining C-C single bond is rather high, and the energy rises back to -10/-18 kcal mol^{-1}. This free energy of the transition structure is comparable to that of transition structures that connect the monodentate adduct to products, suggesting possible competition between different pathways.

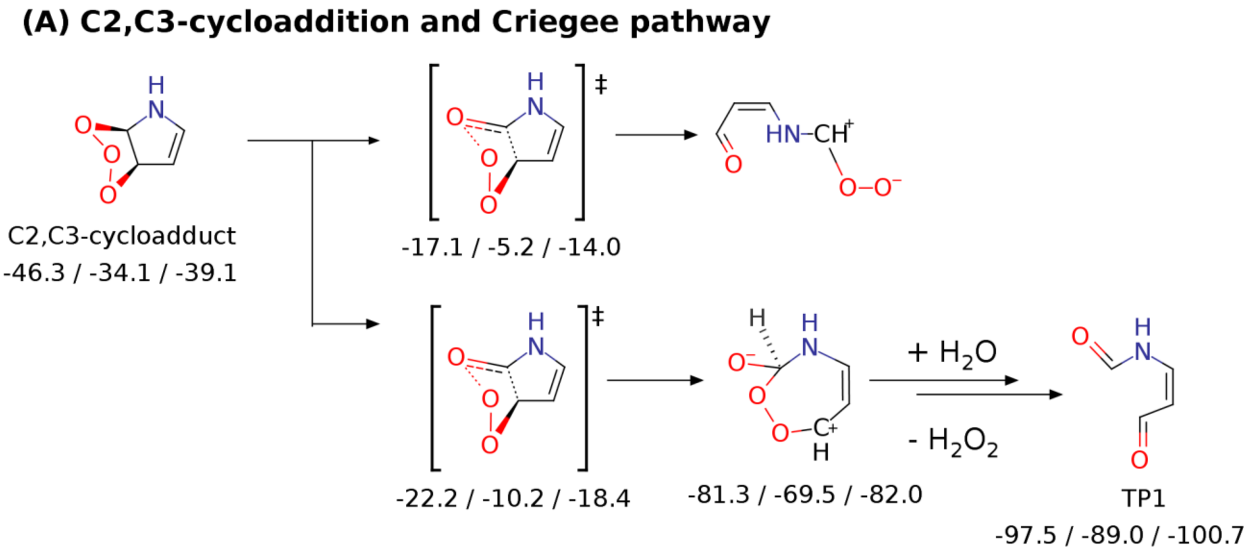
(A) C2,C3-cycloaddition and Criegee pathway

Figure S28. Computational depiction of the pathway (A), the cleavage of the double bond, following the formation of a cyclic adduct during the pyrrole-ozone reaction. The three numbers below each reaction species indicate LC-ωPBE energies at 0 K including zero-point vibrational energies, LC-ωPBE Gibbs free energies at 298 K, and M06-2X Gibbs free energies at 298 K (from left to right).

Text S12. Quantum chemical computation results: pathway (B) of the pyrrole-ozone reaction

The first step of the reaction refers to the autoprotolysis of two water molecules, which formally consumes ~51 kcal mol^{-1}. Hydroxide can abstract a proton from the cycloadduct with a relatively high barrier ($\Delta G^{\ddagger}$ = 27/23 kcal mol^{-1}, Figure S29). This leads immediately to the cleavage of an O-O bond, a planarization, and formation of a C=O double bond. The resulting peroxo-anion can be protonated to yield a stable intermediate. The intermediate can be reacted to the observed product maleimide, cleaving one water molecule. This reaction needs to be catalyzed by another HO^-, but seems kinetically feasible ($\Delta G^{\ddagger}$ = 17/14 kcal mol^{-1}), and leads to an unstable intermediate that cleaves HO^- to yield maleimide.

The overall feasibility of this route depends on (a) if the C2,C5-cycloadduct can be formed and (b) if the initial deprotonation of the cycloadduct is not outcompeted by the back-reaction from the cycloadduct. Since in the real system, hydroxide originates from the (fast) autoprotolysis of water, it will be present at a steady state concentration of 10^{-7} M at pH 7, which should be multiplied with the rate constant to yield an apparent first order rate constant. If an underestimation of the barrier by 5 kcal mol^{-1} is assumed, the Eyring equation will still predict a second order rate constant of 4×10^{-1} M^{-1} s^{-1}, and an apparent rate constant of 4×10^{-8} s^{-1}. The barrier for the reaction of the cycloadduct back to the monodentate adduct is predicted to be ~20 kcal mol^{-1}, corresponding to a rate constant of 1×10^{-2} s^{-1}. To proceed with pathway (B), the barrier of this back-reaction would need to be underestimated by ~5 kcal mol^{-1}. Conversely, it can be argued that the implicit solvation model should underestimate the solvation energy of hydroxide, and to a lesser extent also the solvation energy of the trioxoanion substituent. This should lead to the opposite effect: an underestimation of the barrier connected to the attack of hydroxide, and an overestimation of the barrier of the back-reaction. Thus, pathway (B) seems rather unlikely, even if the C2,C5-cycloadduct can be formed in some way.

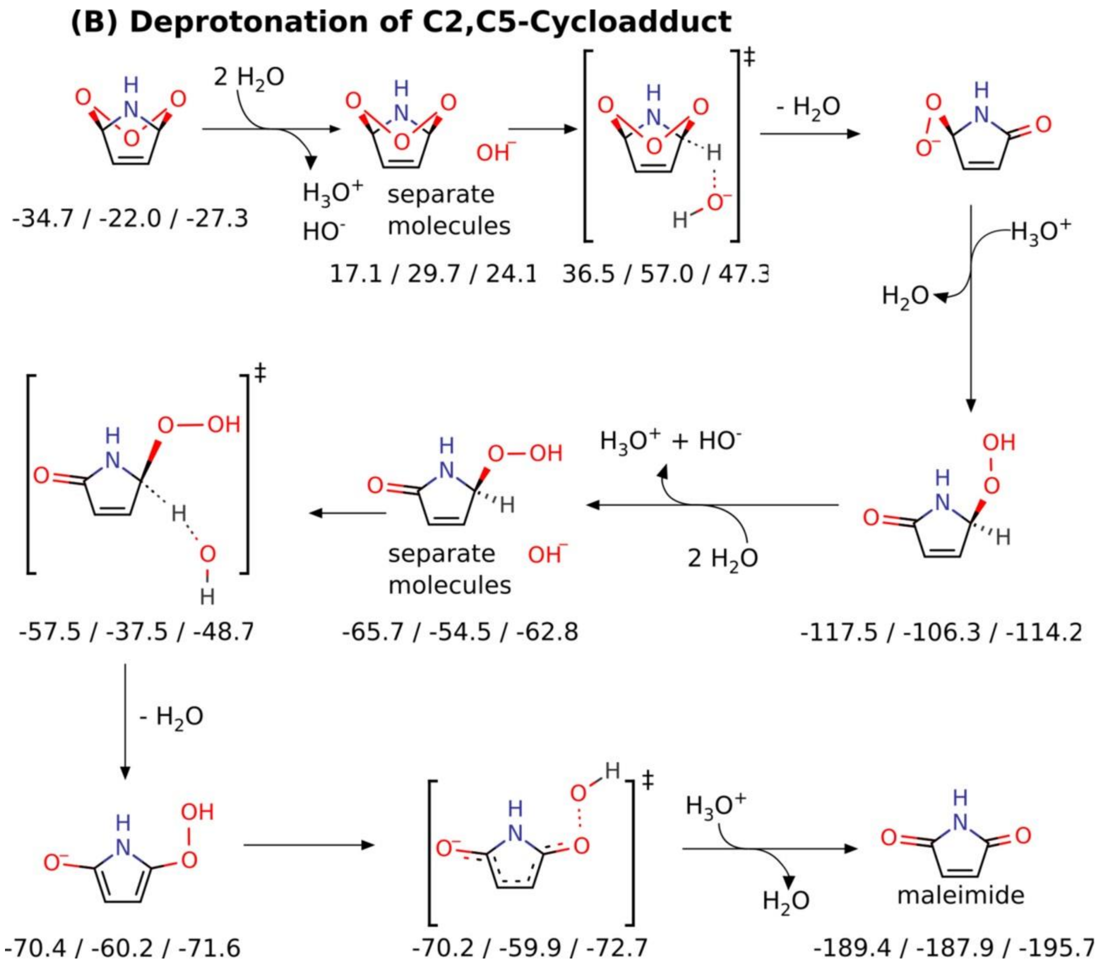

(B) Deprotonation of C2,C5-Cycloadduct

Figure S29. Computational depiction of the pathway (B), the deprotonation of the C2,C5-cycloadduct during the pyrrole-ozone reaction. The three numbers below each reaction species indicate LC-ωPBE energies at 0 K including zero-point vibrational energies, LC-ωPBE Gibbs free energies at 298 K, and M06-2X Gibbs free energies at 298 K (from left to right).

Text S13. Quantum chemical computation results: pathway (D) of the pyrrole-ozone reaction

All energies in Figure S30 depict a low barrier (2-3 kcal mol^{-1}) for cleaving singlet oxygen from the monodentate adduct. Although IRC calculations did not succeed, the imaginary frequency of the transition structure clearly corresponds to the relevant O-O stretch. This reaction is depicted as exergonic by free energy calculations, but as endothermic when neglecting temperature effects. Either way, the energy is drastically lowered when the resulting singlet oxygen converts to its triplet ground state in an irreversible reaction. Cleaving oxygen yields a zwitterion, from which different rearrangements are imaginable, of which we only report final energies. One of the products, 2-hydroxypyrrole, would be fast-reacting with ozone, and could form secondary products.

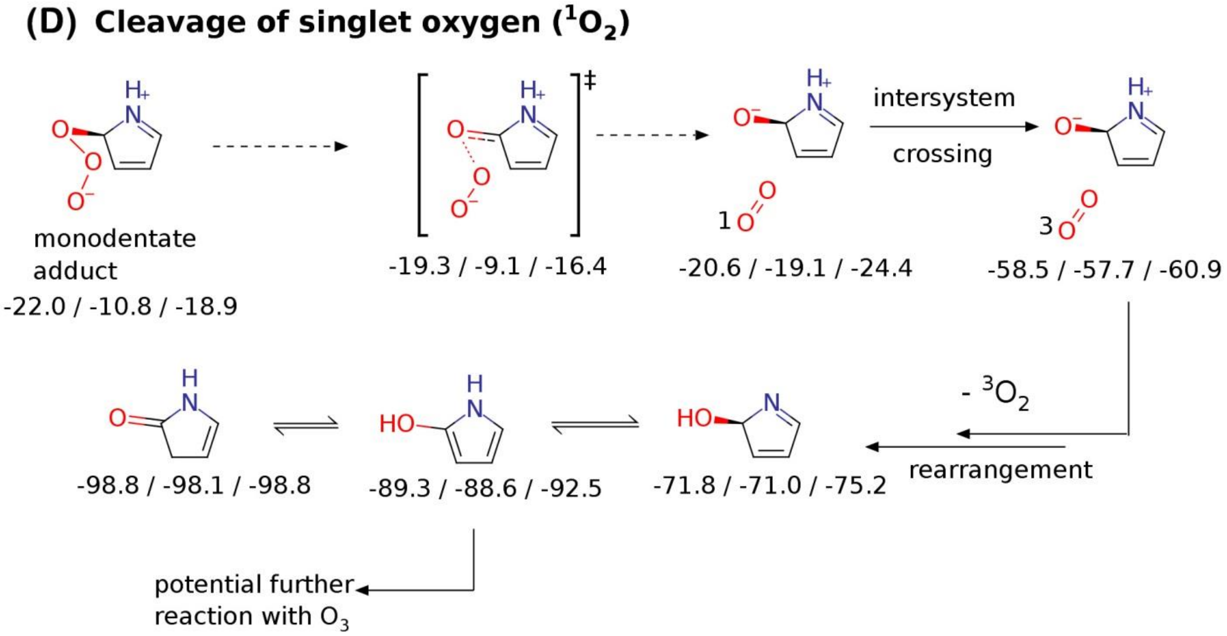

Figure S30. Computational depiction of the pathway (D), the deprotonation of singlet oxygen cleavage from a monodentate adduct. The three numbers below each reaction species indicate LC-ωPBE energies at 0 K including zero-point vibrational energies, LC-ωPBE Gibbs free energies at 298 K, and M06-2X Gibbs free energies at 298 K (from left to right).

Text S14. Quantum chemical computation results: pathways (E) and (F) of the pyrrole-ozone reaction

The zwitterionic adduct can undergo a rearrangement reaction, in which the negatively charged oxygen attacks the C-H position (Figure S31). Calculations could locate a closed-shell transition structure for this reaction, but IRC calculations failed, probably owing to a relatively flat PES around the transition structure. Relaxed scans along H-O distance would yield a zwitterionic, closed shell complex, which is highly unstable. Two possible cage reactions are N-H proton transfer to HOO- or addition of HOO- to the ring, both with negligible barriers. These could lead either to the observed product maleimide, or to pyrrole-2-one. Pyrrole-2-one can potentially hydrolyze, which would lead to the observed TP2. If this reaction is kinetically feasible is not easily answered, as the barrier for reactions with hydroxide could be severely underestimated.

In contrast, a radicalic mechanism should also be possible from the beginning. Owing to limitations of the used methods, complexed radical pairs cannot be simulated. However, the energy of isolated radicals is much lower than that of the zwitterionic complex. A transition structure for radical recombination could be found, though, and this pathway should be kinetically feasible.

(E / F) Rearrangement

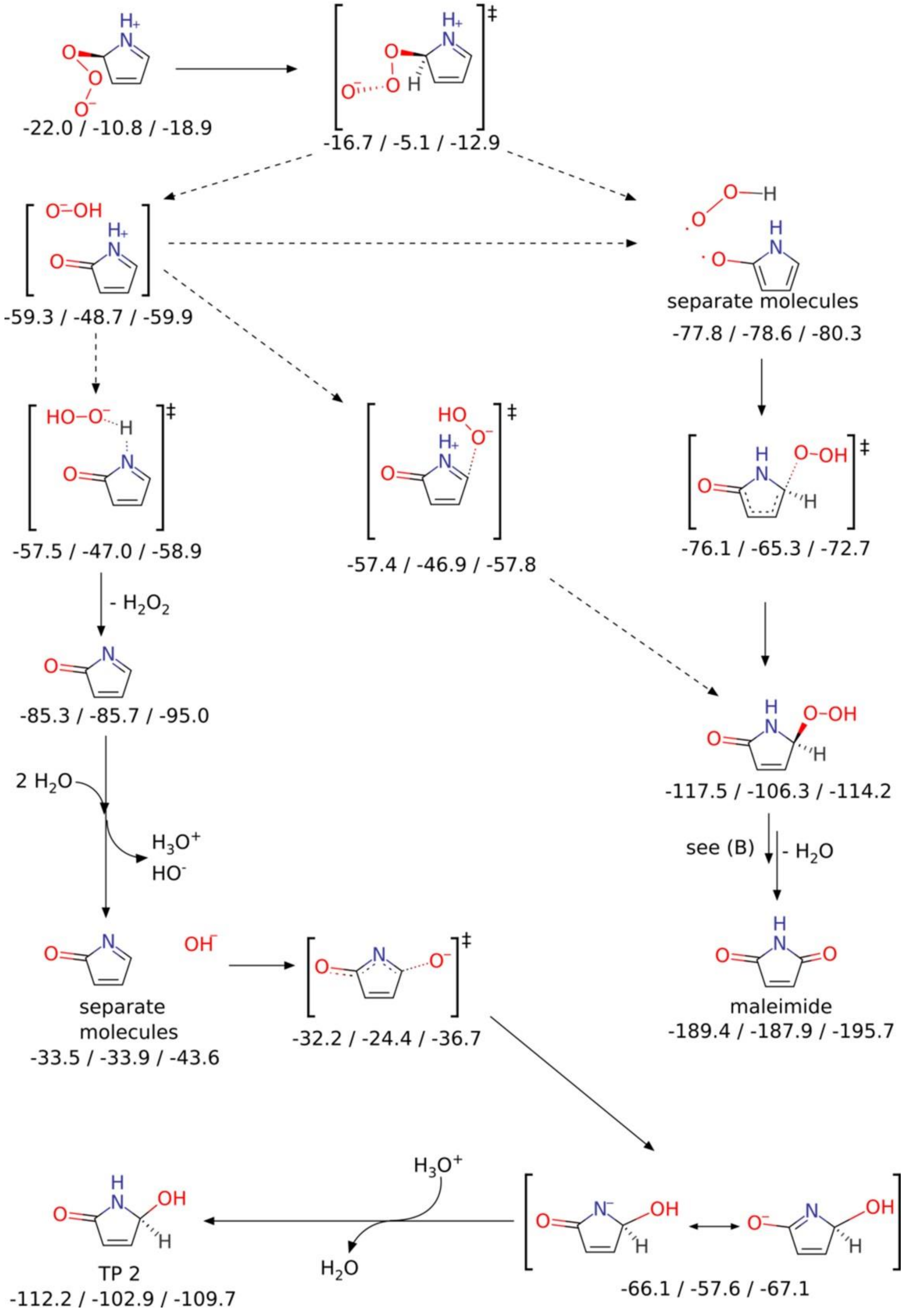

Figure S31. Computational depiction of the pathways (E) and (F), the rearrangement reactions of the zwitterionic adduct. The three numbers below each reaction species indicate LC-ωPBE energies at 0 K including zero-point vibrational energies, LC-ωPBE Gibbs free energies at 298 K, and M06-2X Gibbs free energies at 298 K (from left to right).

Text S15. Quantum chemical computation results: pathway (G) of the pyrrole-ozone reaction

Computations predict that the monodentate adduct can undergo another proton transfer reaction, in which the N-H proton is transferred to the trioxoanion moiety (Figure S32). This reaction is depicted as exergonic. A further exergonic rearrangement is catalyzed by water in the form of hydroxide and hydronium cation, and yields pyrrole with a –OOOH substituent. This molecule should dissociate rather easily into a hydroperoxyl radical and an organic radical, in which the unpaired electron can be stabilized by delocalization in the ring. This reaction is analogous to pathway (E/F) (see above), with the same limitation that the radical pair cannot be simulated.

The initial proton transfer is clearly kinetically feasible, but leads to an only slightly more stable product. From this product, the back-reaction (and subsequent reaction through other pathways) may be in competition with deprotonation by HO^-. The free energy barrier of the reaction with hydroxide is predicted at 6-10 kcal mol^{-1}, but may be underestimated because of shortcomings in the solvation model. In a “back of the envelope” estimation with the Eyring equation, a barrier of 6 kcal mol^{-1} would yield a rate constant of 2×10^8 M^{-1} s^{-1}, and an apparent first order rate constant of 2×10^1 s^{-1}. In comparison, the barrier for the back-reaction is predicted as 16-17 kcal mol^{-1}, formally corresponding to a rate constant of 1×10^1 s^{-1}. Thus, an equilibrium between the proton-transferred structure and the monodentate adduct cannot be excluded, and the forward reaction eventually leading to the observed product maleimide may compete with the back-reaction to the monodentate adduct.

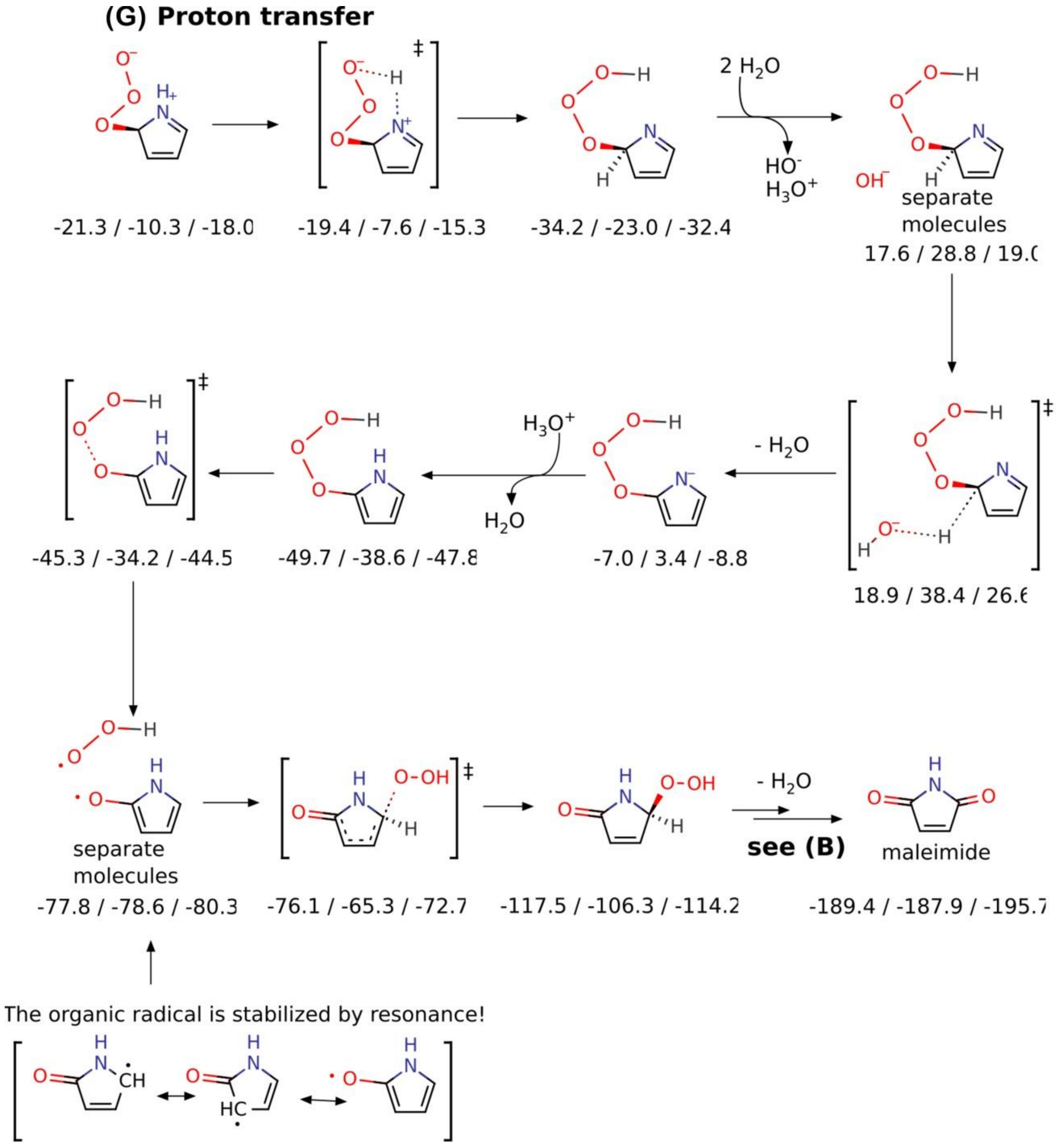

Figure S32. Computational depiction of the pathway (G), the proton transfer pathway starting from the zwitterionic adduct. The three numbers below each reaction species indicate LC-ωPBE energies at 0 K including zero-point vibrational energies, LC-ωPBE Gibbs free energies at 298 K, and M06-2X Gibbs free energies at 298 K (from left to right).

Text S16. Semi-quantification of urea during the imidazole-O_3 reaction.

A minor formation of urea during the reaction of imidazole with ozone was suggested by LC-HRMS/MS with the corresponding reference standard by matching the retention time. The formation of urea as a function of the molar ratio of $[O_3]/[\text{Pyrrole}]_0$ is shown in Figure S33. Accordingly the yield of urea per consumed imidazole was determined to be 8%. However, the urea concentrations should be considered as only semi-quantitative, since they were determined without any internal standards. Moreover, for this analysis, a high mass deviation of ~50 ppm was observed for both ozonated samples and standards (the detected exact mass = 61.0368 in comparison to the theoretical exact mass = 61.0396 for urea as $[M+H]^+$), probably caused by an inadequate mass calibration. This was much higher than the usual mass deviations within 2 ppm for all other analytes (Table S5). Therefore, additional tests with a more careful mass calibration and with an internal standard are required to confirm the formation of urea and its yield for certain.

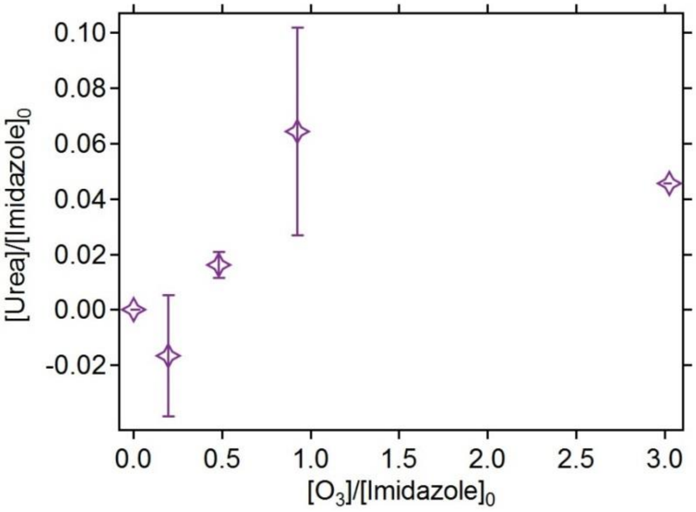

Figure S33. Formation of urea as a function of the molar ratio of $[O_3]/[\text{Imidazole}]_0$ determined by LC-HRMS/MS without internal standards. All measurements were carried out in presence of 50 mM *t*-butanol at pH 7 (20 mM bicarbonate buffer). The initial imidazole concentrations were around 100 µM.

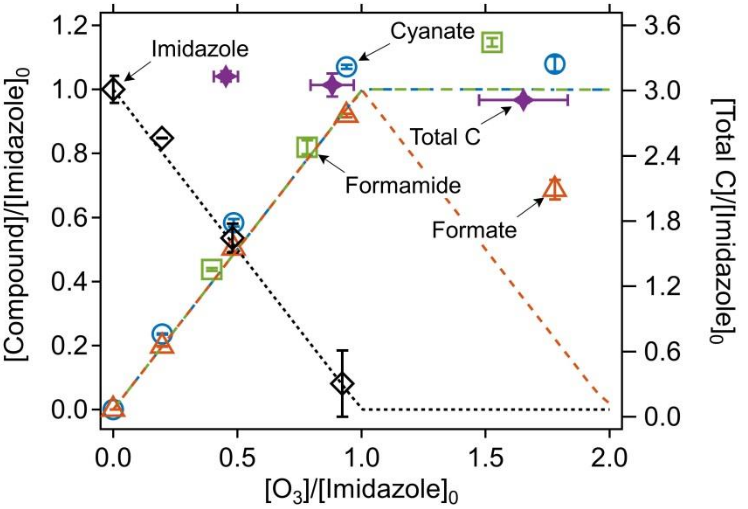

Figure S34. Relative abatement of imidazole and the formation of transformation products as a function of the molar ratio of [O$_3$]/[Imidazole]$_0$, as shown in Figure 5 in the main text. The symbols indicate the measured concentrations (duplicate or triplicate) and the lines indicate simulated concentrations based on the kinetic models described in Table S4. Total C indicates the sum of the concentrations of all carbons in the remaining imidazole and the carbon-containing transformation products.

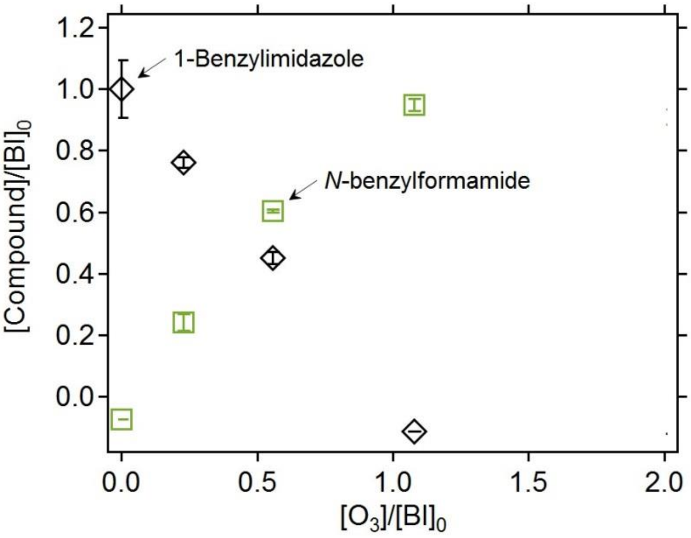

Figure S35. Relative abatement of 1-benzylimidazole (BI) and formation of *N*-benzylformamide as a function of the molar ratio of [O$_3$]/[BI]$_0$. All measurements were carried out in presence of 50 mM *t*-butanol at pH 7 (10 mM phosphate buffer). The initial BI concentrations were around 90 µM.

Text S17. Quantum chemical computation results: the imidazole-ozone reaction

The fate of the cyclic ozonide formed by addition to imidazole was investigated (Figure S36). This reaction can initially follow the Criegee pathway to cleave the double bond. In the resulting acyclic molecules with a zwitterion form, mesomeric effects delocalize the positive charge that is formally assigned to a carbon atom. A ring formation seems then possible with the anionic peroxo substituent of the zwitterion acting as a nucleophile. Two cyclic intermediates containing a dioxazole moiety can be formed in these exergonic reactions. From both structures, rearrangement reactions to formamide and formylisocyanate are imaginable, but were not investigated in more detail. However, this reaction would be strongly exergonic. Reactions of possible monodentate adducts that may be in competition with the shown Criegee mechanism were not investigated.

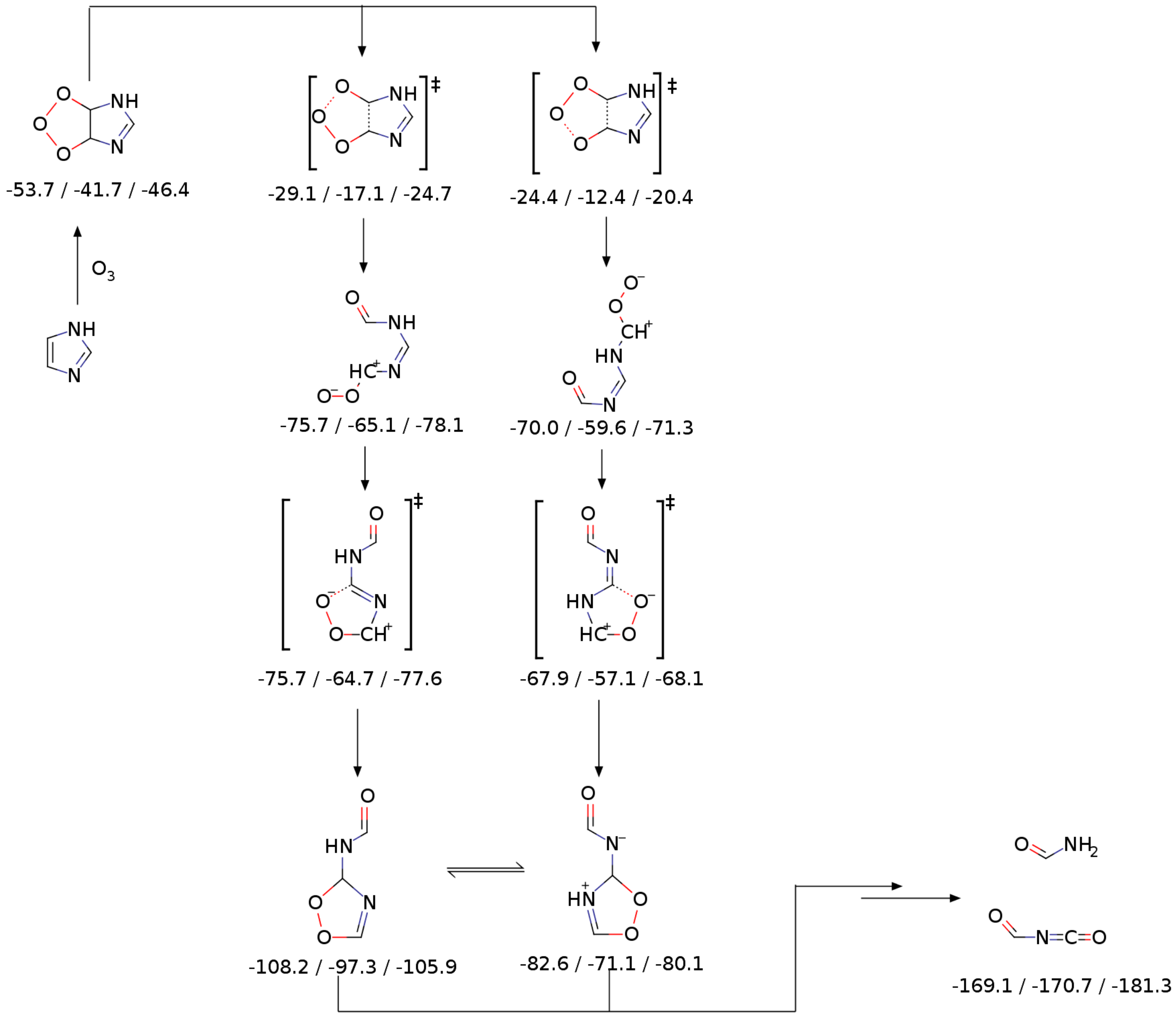

Figure S36. Computational depiction of the reaction of imidazole with ozone. The three numbers below each reaction species indicate LC-ωPBE energies at 0 K including zero-point vibrational energies, LC-ωPBE Gibbs free energies at 298 K, and M06-2X Gibbs free energies at 298 K (from left to right).

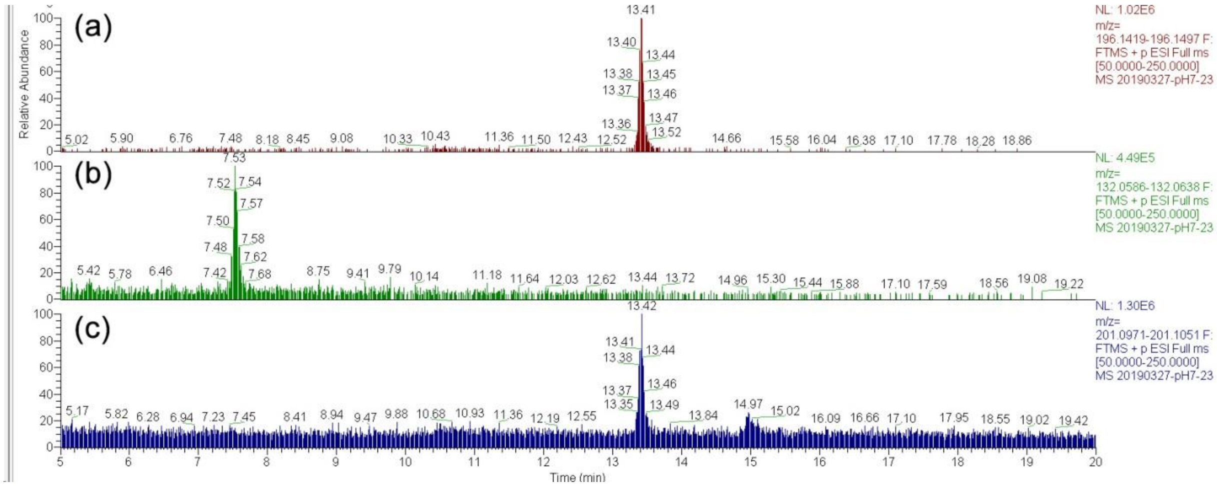

Figure S37. LC-HRMS/MS chromatogram filtered by m/z = (a) 196.1458, (b) 132.0612, and (c) 201.1009 for an ozonated pyrazole sample with a molar $[O_3]/[\text{Pyrazole}]_0$ ratio of ~ 3. All measurements were carried out in presence of 50 mM *t*-butanol at pH 7 (10 mM phosphate buffer). The initial pyrazole concentration was around 100 µM.

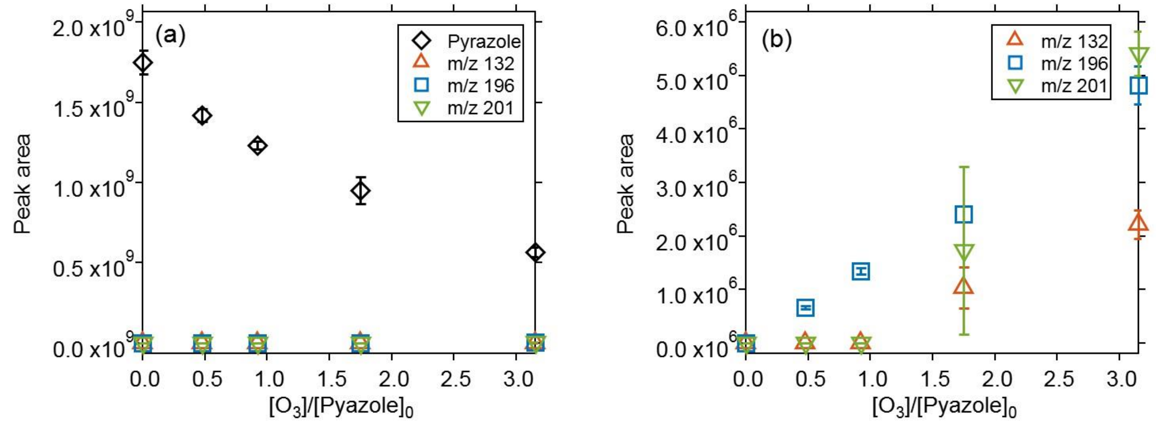

Figure S38. Integrated peak areas of (a) pyrazole and (b) m/z = 132.0612, 196.1458, and 201.1009 as a function of the molar ratio of $[O_3]/[\text{Pyrazole}]_0$. All measurements were carried out in presence of 50 mM *t*-butanol at pH 7 (10 mM phosphate buffer). The initial pyrazole concentration was around 100 µM.

Table S13. Possible molecular formulas for the exact masses of m/z = 132.0612, 196.1458, and 201.1009 by assuming the maximum numbers of occurrences of the isotopes ^{12}C, ^{14}N, ^{16}O, ^{1}H, and ^{23}Na to be 10, 10, 10, 20, and 1, respectively. Only the formulas with mass deviations of less than 20 ppm are shown.

Exact mass	**Possible molecular formula**	**Mass deviation, ppm**
132.0612	$CH_9O_2N_4Na$	-4.3
	CH_6ON_7	-12.4
196.1458	$C_{10}H_{18}ON_3$	6.9
	$C_8H_{16}N_6$	13.8
	$C_8H_{19}ON_3Na$	19.2
201.1009	$C_{10}H_{11}N_5$	0.03
	$C_{10}H_{14}ON_2Na$	5.3
	$C_9H_{15}O_4N$	6.7
	$C_8H_{12}N_5Na$	12.0
	$C_7H_{13}O_3N_4$	13.3
	$C_7H_{16}O_4NNa$	18.6

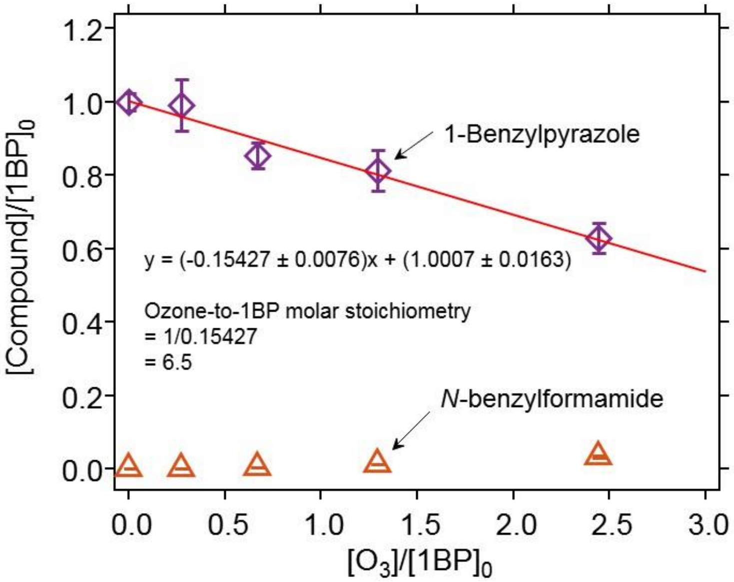

Figure S39. Relative abatement of 1-benzylpyrazole (1BP) and the formation of *N*-benzylformamide as a function of the molar ratio of $[O_3]/[1BP]_0$. The ozone:1BP molar stoichiometry was calculated by inverting the slopes from a linear regression of the measured 1BP concentrations. All measurements were carried out in presence of 50 mM *t*-butanol at pH 7 (10 mM phosphate buffer). The initial 1BP concentration was around 70 µM.

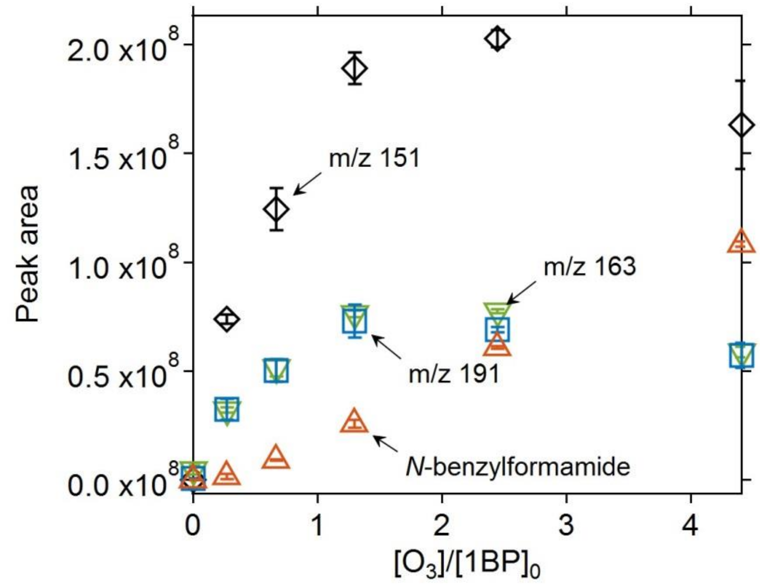

Figure S40. Integrated peak areas of *N*-benzylformamide (triangle), m/z = 151.0864 (diamond), 163.0864 (inversed triangle), and 191.0813 (square) as a function of the molar ratio of $[O_3]/[1BP]_0$ for ozonated 1-benzylpyrazole samples. All measurements were carried out in presence of 50 mM *t*-butanol at pH 7 (10 mM phosphate buffer). The initial 1BP concentration was around 70 µM.

A. Chromatogram

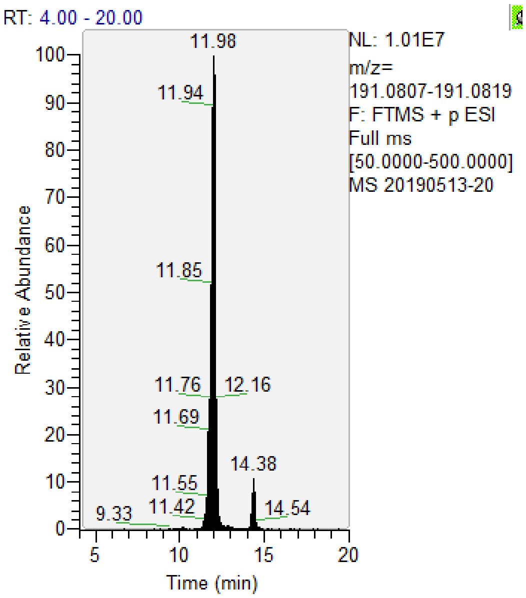

- Peak retention time: 12.0 min
- Peak intensity: 1.0 x 10^7

C. Proposed molecular formula

$C10H10N2O2$

D. Candidate structures

191a

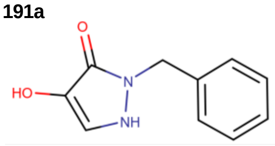

191b

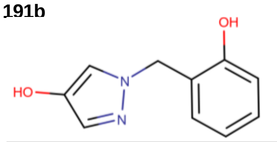

191c

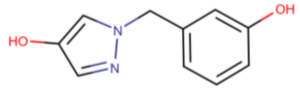

191d

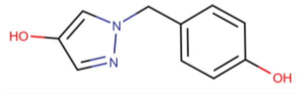

B. MS2 spectra

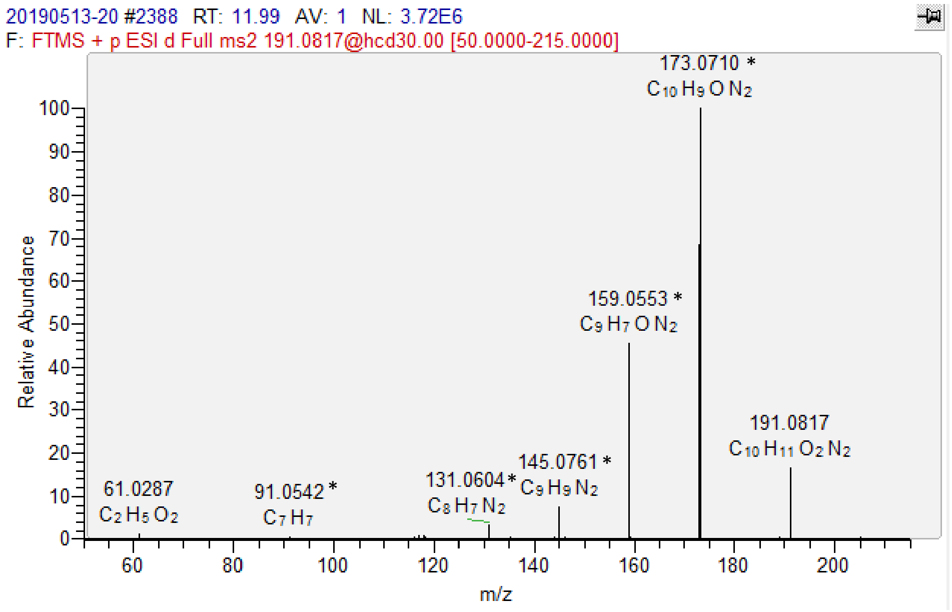

Figure S41. (A) LC-HRMS/MS total ion chromatogram filtered by m/z = 191.0813, (B) the corresponding MS2 spectrum, (C) a proposed molecular formula, and (D) candidate structures of m/z = 191.0813 found by MetFrag analyses for an ozonated 1-benzylpyrazole sample with a molar ratio of $[O_3]/[1BP]_0$ ~ 1. The fragment ions denoted with asterisks (*) match those simulated by MetFrag as shown in Figure S44 and Figure S45. The candidate structure highlighted by a red square indicates the most plausible structure (Text S18).

A. Chromatogram

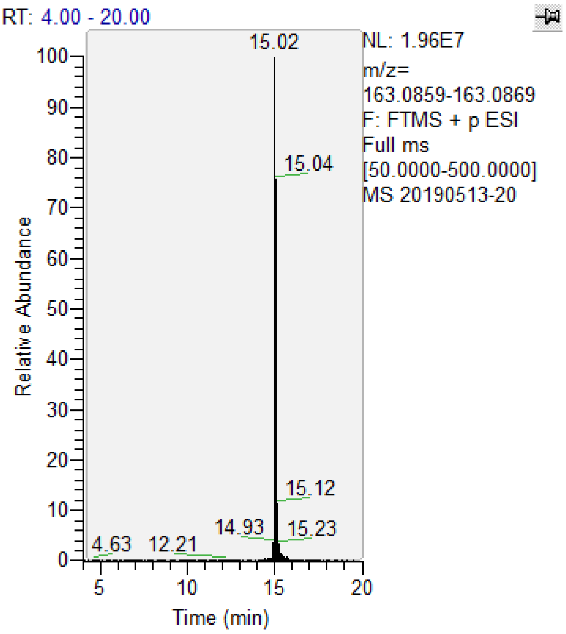

- Peak retention time: 15.0 min
- Peak intensity: 2.0 x 10^7

C. Proposed molecular formula

C9H10N2O

D. Candidate structures

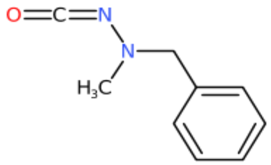

B. MS2 spectra

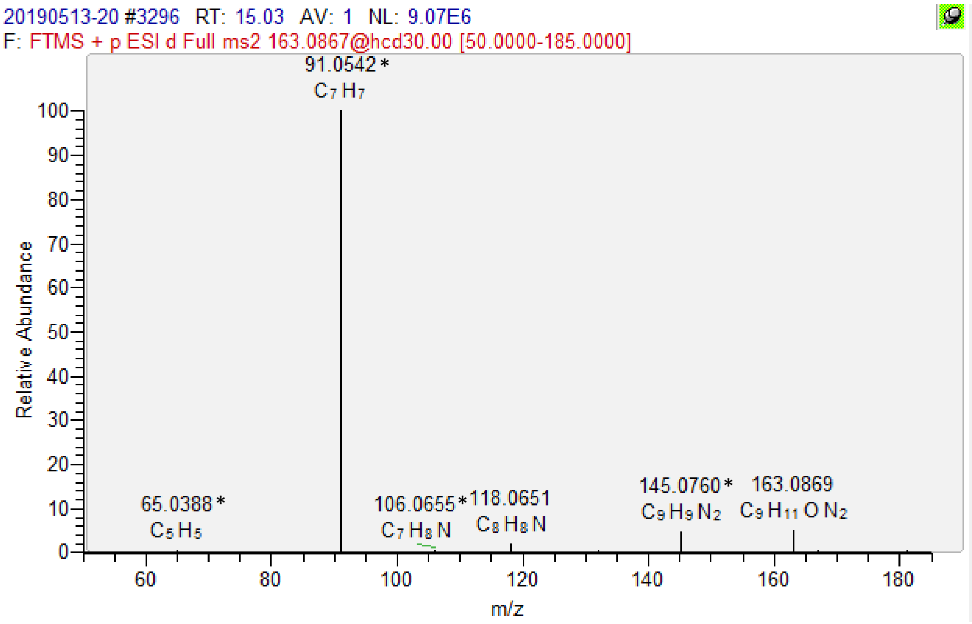

Figure S42. (A) LC-HRMS/MS total ion chromatogram filtered by m/z = 163.0864, (B) the corresponding MS2 spectrum, (C) a proposed molecular formula, and (D) a candidate structure of m/z = 163.0864 found by MetFrag analyses for an ozonated 1-benzylpyrazole sample with a molar ratio of $[O_3]/[1BP]_0$ ~ 1. The fragment ions denoted with asterisks (*) match those simulated by MetFrag as shown in Figure S46.

A. Chromatogram

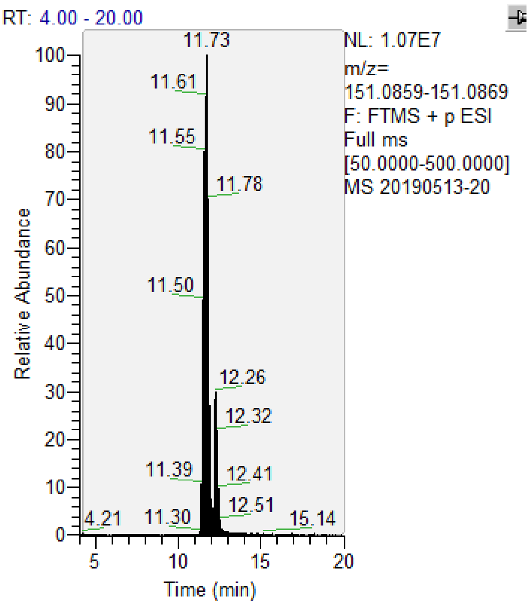

- Peak retention time: 11.7 min
- Peak intensity: 1.1 x 10^7

C. Proposed molecular formula

C8H10N2O

D. Candidate structures

151a

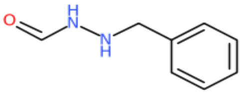

151b

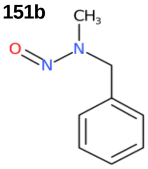

151c

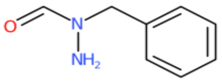

151d

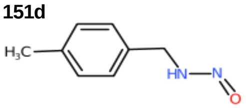

B. MS2 spectra

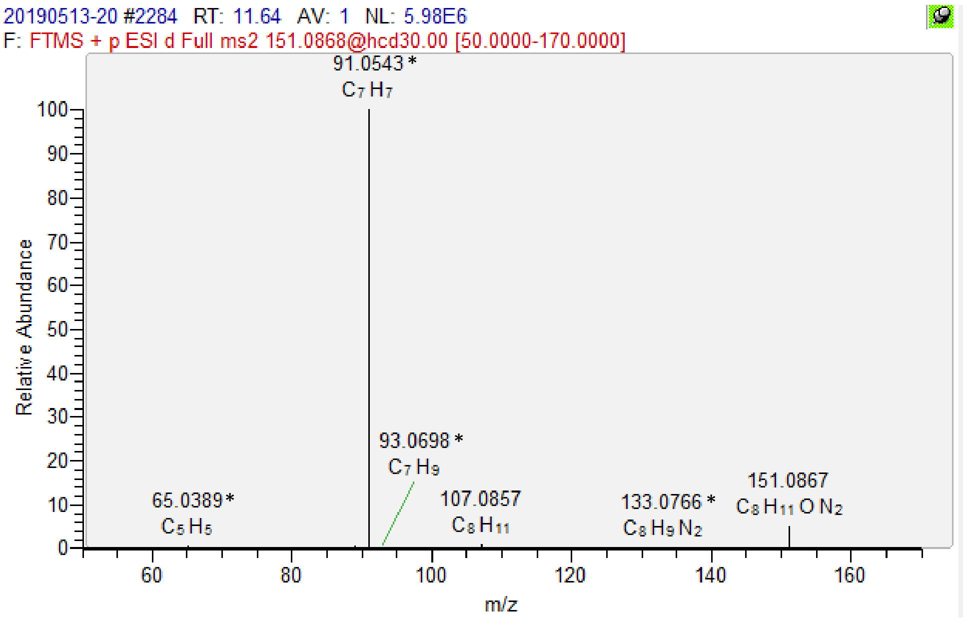

Figure S43. (A) LC-HRMS/MS total ion chromatogram filtered by m/z = 151.0864, (B) the corresponding MS2 spectrum, (C) a proposed molecular formula, and (D) candidate structures of m/z = 151.0864 found by MetFrag analyses for an ozonated 1-benzylpyrazole sample with a molar ratio of $[O_3]/[1BP]_0$ ~ 1. The fragment ions denoted with asterisks (*) match those simulated by MetFrag as shown in Figure S47, Figure S48, Figure S49, and Figure S50. The candidate structure highlighted by a red square indicates the most plausible structure (Text S18).

Text S18. MetFrag procedure and results for m/z 151.0864, 163.0864, and 191.0813 found in the reaction of 1-benzylpyrazole with ozone

To elucidate structures of unknown LC-MS peaks with the exact masses of m/z = 151.0864, 163.0864, and 191.0813 (as $[M+H]^+$) detected in ozonated 1-benzylpyrazole samples, their MS2 spectra were recorded (Figure S41, Figure S42, and Figure S43) and compared with simulated fragment ions of candidate structures obtained by a compound database, PubChem[31] and an *in silico* fragmenter, MetFrag.[32] The database search is incorporated into the web-based MetFrag workflow, available at https://msbi.ipb-halle.de/MetFragBeta/. It should be noted that this approach has the limitation that it only covers the candidate structures available in the applied database, PubChem.[31] Moreover, in some cases, the recorded MS2 spectra contained only a few distinguishing fragment ions, providing only limited structural information (see the cases of m/z = 151.0864 and 163.0864 as examples).

Preliminary candidate structures were obtained by searching PubChem for the exact mass (e.g., 151.0864 as $[M+H]^+$) with mass deviation of 5 ppm. The resulting candidates (total 2993 entries for 151.0864) were further narrowed down (to 4 entries) by filtering their structures with a specific substructure, selecting only the candidates containing a *N*-benzylhydrazine moiety (or “c1ccc(cc1)[CH2]NN” as an input for the structural identifier, SMILES arbitrary target specification), based on the assumption that the moiety should be less reactive towards ozone and thus still be seen as a transformation product. The final candidate structures were then fragmented by MetFrag, using a bond dissociation approach. The resulting fragments were compared with the measured fragment ions by submitting a list of m/z (of fragments) and the corresponding intensities recorded by LC-HRMS/MS measurements. The results are presented below for m/z = 191.0813, 163.0864, and 151.0864, respectively.

a) **m/z = 191.0813 corresponding to $C_{10}H_{10}N_2O_2$ with a mass deviation of -1.1 ppm.** A total of four candidate structures (candidates 191a – 191d as shown in Figure S41D) resulted from the PubChem search. Candidate 191a forms benzylpyrazole with two oxygens added to the pyrazole ring. The other three candidates, candidates 191b – 191d, form benzylpyrazole with two oxygens added to the pyrazole and the benzene rings, respectively. The only difference among candidates 191b – 191d is the location of the hydroxyl group on the benzene ring and thus only candidate 191b is discussed as a representative case hereafter. The candidate structures processed by MetFrag are shown in Figure S44 and Figure S45. The MS2 fragments simulated by MetFrag and matched to the detected fragments are also compiled. The substructure of the candidate structure, forming an individual fragment is highlighted in green. Candidates 191a and 191b share all fragments in common. Thus, it is difficult to conclude which is more plausible than the other based on this analysis. Based on the ozone reactivity, 4-hydroxypyrazole (a possible precursor of both candidates 191a and 191b) is more reactive towards ozone than benzene (Table 1 in the main text). Accordingly, the 4-hydroxypyrazole moiety is more susceptible to the ozone attack than the benzene ring, and therefore, candidate 191a is more plausible than candidate 191b.

Candidate 191a

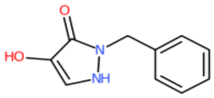

Name: 2-benzyl-4-hydroxy-1H-pyrazol-3-one
Molecular formula: C10H10N2O2
Monoisotopic mass: 190.074
$\mathbf{[M+H]^+}$ = 191.081

Fragments

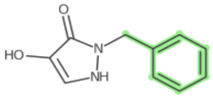

Fragment 1

Formula [C7H7]+
Mass 91.0543
Peak m/z 91.0542

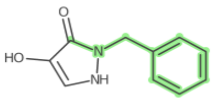

Fragment 2

Formula [C8H7N-H]+
Mass 116.0495
Peak m/z 116.0492

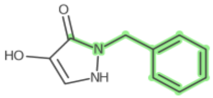

Fragment 3

Formula [C8H7N]+
Mass 117.0573
Peak m/z 117.0573

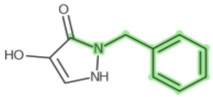

Fragment 4

Formula [C8H7N]+H+
Mass 118.0652
Peak m/z 118.0650

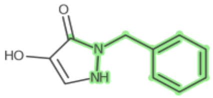

Fragment 5

Formula [C8H8N2-H]+
Mass 131.0604
Peak m/z 131.0604

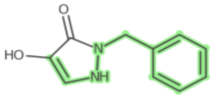

Fragment 6

Formula [C9H9N2-H]+
Mass 144.0682
Peak m/z 144.0683

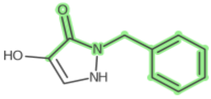

Fragment 7

Formula [C9H7NO]+
Mass 145.0522
Peak m/z 145.0520

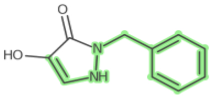

Fragment 8

Formula [C9H9N2]+
Mass 145.0761
Peak m/z 145.0761

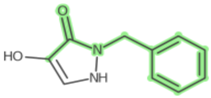

Fragment 9

Formula [C9H7NO]+H+
Mass 146.0601
Peak m/z 146.0601

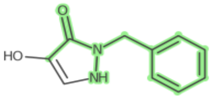

Fragment 10

Formula [C9H8N2O-H]+
Mass 159.0553
Peak m/z 159.0553

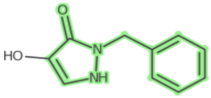

Fragment 11

Formula [C10H9N2O]+
Mass 173.0710
Peak m/z 173.0710

Figure S44. MetFrag results of the candidate 191a. Eleven fragments of 191a obtained by *in silico* fragmentation of MetFrag are shown under “Fragments”. The substructure of 191a forming an individual fragment is highlighted in green. “Mass” indicates the theoretical exact mass of the fragment and “Peak m/z” indicates the exact mass detected by LC-HRMS/MS measurement as shown in Figure S41B.

Candidate 191b

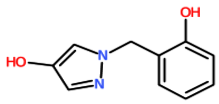

Name: 1-[(2-hydroxyphenyl)methyl]pyrazol-4-ol
Molecular formula: C10H10N2O2
Monoisotopic mass: 190.074
$[M+H]^+$ = 191.081

Fragments

Fragment 1

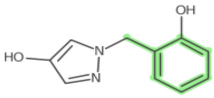

Formula	[C7H6]+H+
Mass	91.05426
Peak m/z	91.0542

Fragment 2

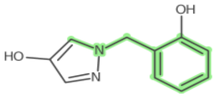

Formula	[C8H7N-H]+
Mass	116.0495
Peak m/z	116.0492

Fragment 3

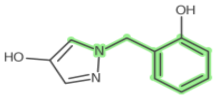

Formula	[C8H7N]+
Mass	117.0573
Peak m/z	117.0573

Fragment 4

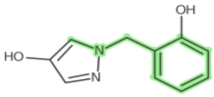

Formula	[C8H7N]+H+
Mass	118.0652
Peak m/z	118.065

Fragment 5

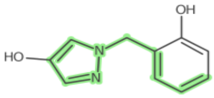

Formula	[C8H7N2]+
Mass	131.0604
Peak m/z	131.0604

Fragment 6

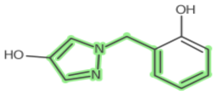

Formula	[C9H8N2]+
Mass	144.0682
Peak m/z	144.0683

Fragment 7

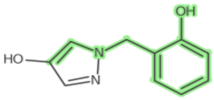

Formula	[C9H8NO-H]+
Mass	145.0522
Peak m/z	145.052

Fragment 8

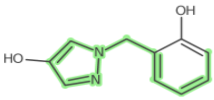

Formula	[C9H8N2]+H+
Mass	145.0761
Peak m/z	145.0761

Fragment 9

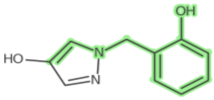

Formula	[C9H8NO]+
Mass	146.0601
Peak m/z	146.0601

Fragment 10

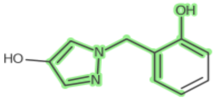

Formula	[C9H8N2O-H]+
Mass	159.0553
Peak m/z	159.0553

Fragment 11

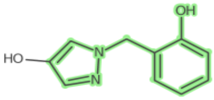

Formula	[C10H9N2O]+
Mass	173.071
Peak m/z	173.071

Figure S45. MetFrag results of the candidate 191b. Eleven fragments of 191b obtained by *in silico* fragmentation of MetFrag are shown under "Fragments". The substructure of 191b forming an individual fragment is highlighted in green. "Mass" indicates the theoretical exact mass of the fragment and "Peak m/z" indicates the exact mass detected by LC-HRMS/MS measurement as shown in Figure S41B.

b) m/z = 163.0864 corresponding to $C_9H_{10}N_2O$ with a mass deviation of -1.2 ppm. The MetFrag analysis resulted in only one candidate structure characterized by an aminoisocyanate moiety (Figure S46). It can form by the prior ozone attack on the pyrazole ring, followed by ring cleavage via a Criegee mechanism. However, it is unlikely that the ring cleavage reaction leaves the methyl substituent on the nitrogen. Instead, carbonyl compounds are often produced as a result of the Criegee mechanism. Therefore, another compound, probably not included in the PubChem database, seems responsible for m/z = 163.0864.

Candidate 163

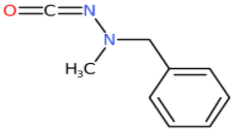

Name: N-isocyanato-N-methyl-1-phenyl-methanamine
Molecular formula: C9H10N2O
Monoisotopic mass: 162.079
$[M+H]^+$ = 163.086

Fragments

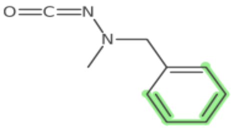

Fragment 1

Formula [C5H5]+
Mass 65.0386
Peak m/z 65.0388

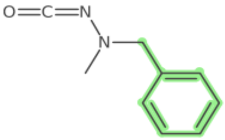

Fragment 2

Formula [C7H7]+
Mass 91.0543
Peak m/z 91.0542

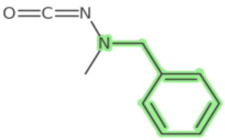

Fragment 3

Formula [C7H7N-H]+
Mass 104.05
Peak m/z 104.05

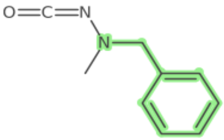

Fragment 4

Formula [C7H7N]+H+
Mass 106.065
Peak m/z 106.066

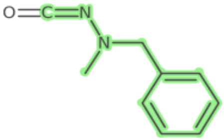

Fragment 5

Formula [C9H10N2-H]+
Mass 145.0761
Peak m/z 145.076

Figure S46. MetFrag results of the candidate 163. Five fragments of 163 obtained by *in silico* fragmentation of MetFrag are shown under “Fragments”. The substructure of 163 forming an individual fragment is highlighted in green. “Mass” indicates the theoretical exact mass of the fragment and “Peak m/z” indicates the exact mass detected by LC-HRMS/MS analysis as shown in Figure S42B.

c) **m/z = 151.0864 corresponding to $C_8H_{10}N_2O$ with a mass deviation of -1.3 ppm.** The MetFrag analysis resulted in four candidate structures, candidates 151a – 151d (Figure S47, Figure S48, Figure S49, and Figure S50). Candidates 151b and 151d contain an *N*-nitroso moiety of which presence was rejected by the total *N*-nitrosamine analysis that detected no nitrosamines. The remaining candidates 151a and 151c contain a hydrazide moiety and candidate 151c is more likely to form via a Criegee mechanism as shown in Figure 8 in the main text.

Candidate 151a

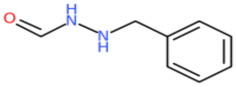

Name: N-(benzylamino)formamide
Molecular formula: C8H10N2O
Monoisotopic mass: 150.079
[M+H]$^+$ = 151.086

Fragments

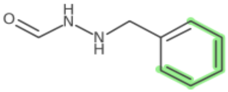

Fragment 1

Formula [C5H5]+
Mass 65.0386
Peak m/z 65.0389

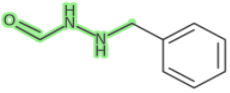

Fragment 2

Formula [C2H5N2O]+
Mass 73.0397
Peak m/z 73.0397

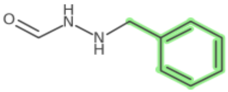

Fragment 3

Formula [C7H7]+
Mass 91.0543
Peak m/z 91.0543

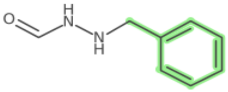

Fragment 4

Formula [C7H7+H]+H+
Mass 93.0699
Peak m/z 93.0698

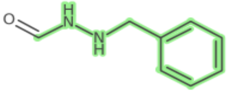

Fragment 5

Formula [C8H10N2-H]+
Mass 133.076
Peak m/z 133.077

Figure S47. MetFrag results of the candidate 151a. Five fragments of 151a obtained by *in silico* fragmentation of MetFrag are shown under “Fragments”. The substructure of 151a forming an individual fragment is highlighted in green. “Mass” indicates the theoretical exact mass of the fragment and “Peak m/z” indicates the exact mass detected by LC-HRMS/MS analysis as shown in Figure S43B.

Candidate 151b

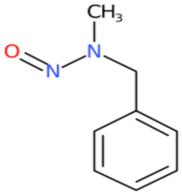

Name: N-benzyl-N-methyl-nitrous amide
Molecular formula: C8H10N2O
Monoisotopic mass: 150.079
$[M+H]^+$ = 151.086

Fragments

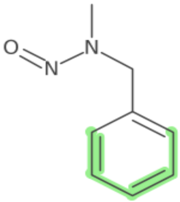

Fragment 1

Formula	[C5H5]+
Mass	65.0386
Peak m/z	65.0389

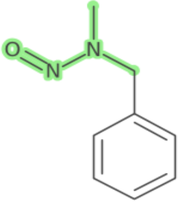

Fragment 2

Formula	[C2H5N2O]+
Mass	73.0397
Peak m/z	73.0397

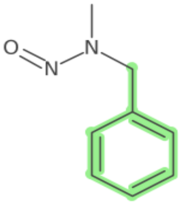

Fragment 3

Formula	[C7H7]+
Mass	91.0543
Peak m/z	91.0543

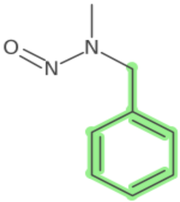

Fragment 4

Formula	[C7H7+H]+H+
Mass	93.0699
Peak m/z	93.0698

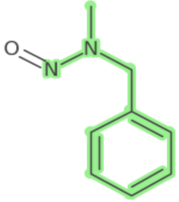

Fragment 5

Formula	[C8H10N2-H]+
Mass	133.076
Peak m/z	133.077

Figure S48. MetFrag results of the candidate 151b. Five fragments of 151b obtained by *in silico* fragmentation of MetFrag are shown under “Fragments”. The substructure of 151b forming an individual fragment is highlighted in green. “Mass” indicates the theoretical exact mass of the fragment and “Peak m/z” indicates the exact mass detected by LC-HRMS/MS analysis as shown in Figure S43B.

Candidate 151c

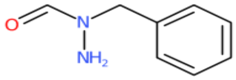

Name: N-amino-N-benzyl-formamide
Molecular formula: C8H10N2O
Monoisotopic mass: 150.079
$[M+H]^+$ = 151.086

Fragments

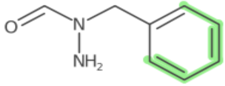

Fragment 1

Formula [C5H5]+
Mass 65.0386
Peak m/z 65.0389

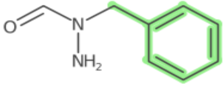

Fragment 4

Formula [C7H7+H]+H+
Mass 93.0699
Peak m/z 93.0698

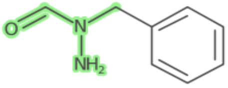

Fragment 2

Formula [C2H5N2O]+
Mass 73.0397
Peak m/z 73.0397

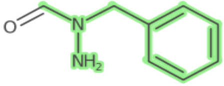

Fragment 5

Formula [C8H10N2-H]+
Mass 133.076
Peak m/z 133.077

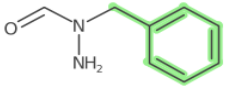

Fragment 3

Formula [C7H7]+
Mass 91.0543
Peak m/z 91.0543

Figure S49. MetFrag results of the candidate 151c. Five fragments of 151c obtained by *in silico* fragmentation of MetFrag are shown under “Fragments”. The substructure of 151c forming an individual fragment is highlighted in green. “Mass” indicates the theoretical exact mass of the fragment and “Peak m/z” indicates the exact mass detected by LC-HRMS/MS analysis as shown in Figure S43B.

Candidate 151d

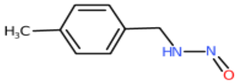

Name: N-(p-tolylmethyl)nitrous amide
Molecular formula: C8H10N2O
Monoisotopic mass: 150.079
[M+H]$^+$ = 151.086

Fragments

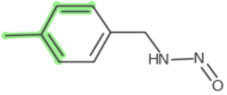

Fragment 1

Formula [C5H6-H]+
Mass 65.0386
Peak m/z 65.0389

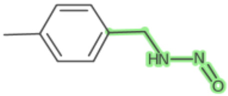

Fragment 2

Formula [C2H3N2O+H]+H+
Mass 73.0397
Peak m/z 73.0397

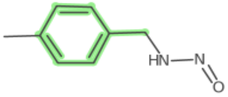

Fragment 3

Formula [C7H6-H]+
Mass 89.0386
Peak m/z 89.0386

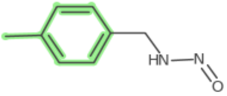

Fragment 4

Formula [C7H7]+
Mass 91.0543
Peak m/z 91.0543

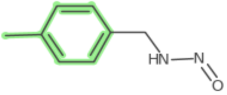

Fragment 5

Formula [C7H7+H]+H+
Mass 93.0699
Peak m/z 93.0698

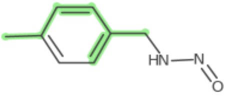

Fragment 6

Formula [C7H8+2H]+H+
Mass 95.0856
Peak m/z 95.0854

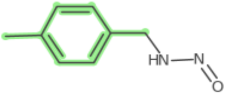

Fragment 7

Formula [C8H9+H]+H+
Mass 107.086
Peak m/z 107.086

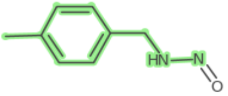

Fragment 8

Formula [C8H10N2-H]+
Mass 133.076
Peak m/z 133.077

Figure S50. MetFrag results of the candidate 151d. Eight fragments of 151d obtained by *in silico* fragmentation of MetFrag are shown under “Fragments”. The substructure of 151d forming an individual fragment is highlighted in green. “Mass” indicates the theoretical exact mass of the fragment and “Peak m/z” indicates the exact mass detected by LC-HRMS/MS analysis as shown in Figure S43B.

Table S14. Average abatement of the micropollutants containing a pyrrole, imidazole, or pyrazole moiety during ozonation at a full-scale wastewater treatment plant, based on the Table S7 in Bourgin et al. (2018).[33] The abatements were calculated by comparing the average concentrations after biological treatment with after ozonation. For the substrates of which concentrations were below LOQ after ozonation, their abatements were calculated by using the LOQs and presented as the minimum abatements with ">" signs.[33]

Substance	**Substructure**	**Use**	**LOQ, ng L^{-1}**	**Average concentration after biological treatment, ng L^{-1}**	**Average concentration after ozonation, ng L^{-1}**	**Average abatement during ozonation, %**
Fluvastatin	Pyrrole	Pharmaceuticals	1.3	4	< LOQ	> 67
Fludioxonil	Pyrrole	Pesticides	1	3	< LOQ	> 64
Atorvastatin	Pyrrole	Pharmaceuticals	35	60	< LOQ	> 41
Etodolac	Pyrrole	Pharmaceuticals	0.8	110	< LOQ	> 99
Indomethacin	Pyrrole	Pharmaceuticals	2	91	< LOQ	> 98
Thiabendazol	Imidazole	Pesticides	1.6	6	1	> 65
Candesartan	Imidazole	Pharmaceuticals	5	330	91	72
Eprosartan	Imidazole	Pharmaceuticals	3	45	< LOQ	> 93
2-Aminobenzimidazol	Imidazole	Biocides	5	10	< LOQ	> 50
Metronidazol	Imidazole	Pharmaceuticals	8	112	47	58
Carbendazim	Imidazole	Biocides	3	28	< LOQ	> 89
Climbazol	Imidazole	Personal Care Products	1	66	2	98
Losartan	Imidazole	Pharmaceuticals	4	260	3	> 98
Ketoconazol	Imidazole	Pharmaceuticals	10	65	< LOQ	> 84
Telmisartan	Imidazole	Pharmaceuticals	1	93	22	76
Fipronil	Pyrazole	Pesticides	0.9	5	2	58
Fipronil-sulfon	Pyrazole	Pesticides	0.5	2	1	58

References

1 W. A. Pryor, D. H. Giamalva and D. F. Church, *Journal of the American Chemical Society*, 1984, **106**, 7094–7100.

2 G. V. Buxton, C. L. Greenstock, W. P. Helman and A. B. Ross, *Journal of Physical and Chemical Reference Data*, 1988, **17**, 513–886.

3 T. Nash, *Biochemical Journal*, 1953, **55**, 416.

4 P. Dowideit and C. von Sonntag, *Environmental Science & Technology*, 1998, **32**, 1112–1119.

5 H. Bader and J. Hoigné, *Ozone: Science & Engineering*, 1982, **4**, 169–176.

6 J. R. Rumble, Ed., in *CRC Handbook of Chemistry and Physics, 100th Edition (Internet Version 2019)*, CRC Press/Taylor & Francis, Boca Raton, FL, 2019.

7 J. C. Ianni, Kintecus, 2017, Windows Version 6.01, www.kintecus.com.

8 J. Hoigné, H. Bader, W. R. Haag and J. Staehelin, *Water Research*, 1985, **19**, 993–1004.

9 E. Reisz, A. Fischbacher, S. Naumov, C. von Sonntag and T. C. Schmidt, *Ozone: Science & Engineering*, 2014, **36**, 532–539.

10 F. Breider and U. von Gunten, *Analytical Chemistry*, 2017, **89**, 1574–1582.

11 A. Shrivastava and V. Gupta B., *Chronicles of Young Scientists*, 2011, **2**, 21.

12 C. S. McArdell, A. C. Alder, A. Göbel, D. Löffler, M. J.-F. Suter and T. A. Ternes, in *Human pharmaceuticals, hormones and fragrances. The challenge of micropollutants in urban water management*, 2006, pp. 55–105.

13 S. Ohmori, M. Mori, M. Kawase and S. Tsuboi, *Journal of Chromatography B: Biomedical Sciences and Applications*, 1987, **414**, 149–155.

14 S. Lim, C. S. McArdell and U. von Gunten, *Water Research*, 2019, **157**, 514–528.

15 F. Muñoz, E. Mvula, S. E. Braslavsky and C. von Sonntag, *Journal of the Chemical Society, Perkin Transactions 2*, 2001, 1109–1116.

16 A. M. Held, D. J. Halko and J. K. Hurst, *Journal of the American Chemical Society*, 1978, **100**, 5732–5740.

17 R. Flyunt, A. Leitzke, G. Mark, E. Mvula, E. Reisz, R. Schick and C. von Sonntag, *The Journal of Physical Chemistry B*, 2003, **107**, 7242–7253.

18 A. O. Allen, C. J. Hochanadel, J. A. Ghormley and T. W. Davis, 1952, **56**, 575–586.

19 K. Kitsuka, A. M. Mohammad, M. I. Awad, K. Kaneda, M. Ikematsu, M. Iseki, K. Mushiake and T. Ohsaka, *Chem. Lett.*, 2007, **36**, 1396–1397.

20 H. Bader, V. Sturzenegger and J. Hoigne, *Water Research*, 1988, **22**, 1109–1115.

21 M. J. Frisch, G. W. Trucks, H. B. Schlegel, G. E. Scuseria, M. A. Robb, J. R. Cheeseman, G. Scalmani, V. Barone, G. A. Petersson, H. Nakatsuji, X. Li, M. Caricato, A. Marenich, J. Bloino, B. G. Janesko, R. Gomperts, B. Mennucci, H. P. Hratchian, J. V. Ortiz, A. F. Izmaylov, J. L. Sonnenberg, D. Williams-Young, F. Ding, F. Lipparini, F. Egidi, J. Goings, B. Peng, A. Petrone, T. Henderson, D. Ranasinghe, V. G. Zakrzewski, J. Gao, N. Rega, G. Zheng, W. Liang, M. Hada, M. Ehara, K. Toyota, R. Fukuda, J. Hasegawa, M. Ishida, T. Nakajima, Y. Honda, O. Kitao, H. Nakai, T. Vreven, K. Throssell, J. A. Montgomery, Jr., J. E. Peralta, F. Ogliaro, M. Bearpark, J. J. Heyd, E. Brothers, K. N. Kudin, V. N. Staroverov, T. Keith, R. Kobayashi, J. Normand, K. Raghavachari, A. Rendell, J. C. Burant, S. S. Iyengar, J. Tomasi, M. Cossi, J. M. Millam, M. Klene, C. Adamo, R. Cammi, J. W. Ochterski, R. L. Martin, K. Morokuma, O. Farkas, J. B. Foresman and D. J. Fox, *Gaussian 09, Revision D.01*, Gaussian, Inc., Wallingford CT, 2016.

22 O. A. Vydrov and G. E. Scuseria, *J. Chem. Phys.*, 2006, **125**, 234109.

23 A. V. Marenich, C. J. Cramer and D. G. Truhlar, *The Journal of Physical Chemistry B*, 2009, **113**, 6378–6396.

24 K. Fukui, *Acc. Chem. Res.*, 1981, **14**, 363–368.

25 D. Rappoport and F. Furche, *J. Chem. Phys.*, 2010, **133**, 134105.

26 Y. Zhao and D. G. Truhlar, *Theoretical Chemistry Accounts*, 2008, **120**, 215–241.

27 C. A. Jiménez-Hoyos, B. G. Janesko and G. E. Scuseria, *Physical Chemistry Chemical Physics*, 2008, **10**, 6621–6629.

28 D. Trogolo, J. S. Arey and P. R. Tentscher, *The Journal of Physical Chemistry A*, , DOI:10.1021/acs.jpca.8b10323.

29 Y. Zhao, O. Tishchenko, J. R. Gour, W. Li, J. J. Lutz, P. Piecuch and D. G. Truhlar, *The Journal of Physical Chemistry A*, 2009, **113**, 5786–5799.

30 R. Quintanilla-Licea, J. Colunga-Valladares, A. Caballero-Quintero, C. Rodríguez-Padilla, R. Tamez-Guerra, R. Gómez-Flores and N. Waksman, *Molecules*, 2002, **7**, 662–673.

31 S. Kim, J. Chen, T. Cheng, A. Gindulyte, J. He, S. He, Q. Li, B. A. Shoemaker, P. A. Thiessen, B. Yu, L. Zaslavsky, J. Zhang and E. E. Bolton, *Nucleic Acids Res*, 2019, **47**, D1102–D1109.

32 C. Ruttkies, E. L. Schymanski, S. Wolf, J. Hollender and S. Neumann, *J Cheminform*, 2016, **8**, 3.

33 M. Bourgin, B. Beck, M. Boehler, E. Borowska, J. Fleiner, E. Salhi, R. Teichler, U. von Gunten, H. Siegrist and C. S. McArdell, *Water Research*, 2018, **129**, 486–498.